Institut für Physik und Astronomie
Astrophysik

Hydrogen-deficient Central Stars of Planetray Nebulae

Dissertation
zur Erlangung des akademischen Grades
"doctor rerum naturalium"
(Dr. rer. nat.)
in der Wissenschaftsdisziplin Astrophysik

eingereicht an der
Mathematisch-Naturwissenschaftlichen
Fakultät
der Universität Potsdam

von
Helge Todt

Potsdam, den 3. September 2009

This work is licensed under a Creative Commons License:
Attribution - Noncommercial - No Derivative Works 3.0 Germany
To view a copy of this license visit
http://creativecommons.org/licenses/by-nc-nd/3.0/de/deed.en

Published online at the
Institutional Repository of the University of Potsdam:
URL http://opus.kobv.de/ubp/volltexte/2010/4104/
URN urn:nbn:de:kobv:517-opus-41047
http://nbn-resolving.org/urn:nbn:de:kobv:517-opus-41047

Contents

1 Introduction **4**

1.1 Wolf-Rayet-type central stars of planetary nebulæ 4
1.2 Task 4
1.3 Previous work 6
1.3.1 Analyses of [WCL] stars 7
1.3.2 Analyses of [WCE] stars 10
1.3.3 PG-1159 stars and white dwarfs 10
1.3.4 Theory of the formation of hydrogen-deficient CSPN 11
1.3.5 Overview of previous analyses 14

2 Methods **19**

3 Analyses of [WC] stars **20**

3.1 Parameters of [WCE]-type central stars 20
3.1.1 Determination of T_* and R_t 21
3.2 Clumping in the winds of [WC]-type central stars 24
3.3 Chemical abundances 28
3.3.1 Carbon and Helium 28
3.3.2 Oxygen 32
3.3.3 Hydrogen 33
3.3.4 Nitrogen 33
3.3.5 Neon 33
3.4 New line-blanketed analyses of individual [WCE] stars 36
3.4.1 NGC 2867 37
3.4.2 PB 6 37
3.4.3 NGC 5189 39
3.4.4 NGC 6905 41
3.4.5 NGC 7026 44
3.4.6 Hen 2-55 44
3.4.7 [S71d]3 – Sanduleak 3 47
3.4.8 IC 1747 51
3.4.9 NGC 1501 53
3.4.10 NGC 6369 55
3.4.11 NGC 5315 55
3.4.12 Summary of the [WCE] spectral analyses 58
3.5 Mass-loss rates from radio observation 59

3.6 Distances of planetary nebulæ 60

4 Discussion **65**
4.1 Chemical abundances of [WC] central stars 65
4.1.1 Helium and carbon abundances 65
4.1.2 Hydrogen 68
4.1.3 Oxygen 68
4.1.4 Nitrogen 69
4.1.5 Neon 69
4.1.6 Iron 70
4.2 Conclusion 70

5 Analyses of hydrogen-deficient non-[WC] stars **72**
5.1 PN PB 8 72
5.1.1 Introduction 72
5.1.2 Observations 72
5.1.3 Analysis 73
5.1.4 Discussion 85
5.2 PMR 5 - A [WN] central star candidate 91
5.2.1 Observations 91
5.2.2 Analysis 92
5.2.3 Discussion 94

1 Introduction

1.1 Wolf-Rayet-type central stars of planetary nebulæ

Stars are the engines of chemical evolution in the universe. Starting with nothing more than hydrogen, helium, and traces of lithium the universe has been enriched by other chemical elements as the result of stellar evolution.

The most frequent stars in the present universe have an initial mass of below $8\,M_{\odot}$. Many of them will undergo a phase of simultaneous helium and hydrogen shell burning as an asymptotic giant branch star (AGB) when approaching the end of their evolution. Shell burning, unlike core burning of our sun, is not stable against thermal runaways, called thermal pulses (see e.g. Kippenhahn & Weigert 1990). The theory of stellar evolution predicts a periodic occurrence of thermal pulses with the possibility of mixing of layers of different chemical compositions. In the AGB phase, various processes of nucleosynthesis occur, including the formation of elements heavier than iron by capture of slow neutrons (s-process) as a result of thermal pulses.

Although spectral analysis of AGB stars has already been performed, e.g. seeking for s-process elements, studying post-AGB stars provides deeper insight into the stellar evolution during the AGB phase. When a star leaves the AGB phase, it has lost its envelope, thus it displays former subsurface layers.

Post-AGB stars in a certain, very narrow range of mass evolve fast enough to become hotter than 25 000 K before their circumstellar matter is dispersed; the ejected envelope becomes excited by the ionizing radiation of their central star and a so called planetary nebula (PN) becomes visible.

Planetary nebulæ, being a frequent phenomenon that can be easily discovered by their Hα and/or [O III] emission, are widely used as astronomical tools, e.g. to trace stellar populations or as a distance measure. A good understanding of PNe, their formation and evolution is therefore necessary.

1.2 Task

A considerable fraction of the central stars of planetary nebulæ (CSPNe) are hydrogen deficient. As a rule, the atmospheres of such CSPNe exhibit a chemical composition of helium, carbon and oxygen resulting from partial helium burning. Most of them show a dense stellar wind like the massive Pop I Wolf-Rayet (WR) stars and are, in analogy, classified as [WC].

Similar to the Pop I WC classification scheme, there is a sequence from the "early" subtypes [WC 2-5] showing lines of C IV, He II and O V-VII to the "late" subtypes [WC 6-11] with spectra dominated by lower ions. This scheme was later refined by Acker &

Neiner (2003) such that the earliest types of [WC] stars which show very strong emission of O VI are designated as [WO 1-4] stars.

The determination of element abundances by spectral analyses provides the empirical base for understanding the origin and evolution of H-deficient [WC] stars.

It was suggested that this classification scheme corresponds to an evolutionary sequence from the cooler [WC]-late types to the hotter [WC]-early types.

However, previous spectral analyses of Wolf-Rayet type central stars resulted in different abundance patterns for late- and early [WC] subtypes (cf. Sect. 1.3.5), which could not be explained in the framework of post-AGB evolutionary scenarios with any form of a late thermal pulse.

The concerns about this sequence are corroborated by the distribution of the subtypes. [WC]-CSPNe seem to prefer extreme subtypes. Intermediate subtypes, e.g. [WC5-6] are relatively rare, thus presenting a rather bimodal distribution.

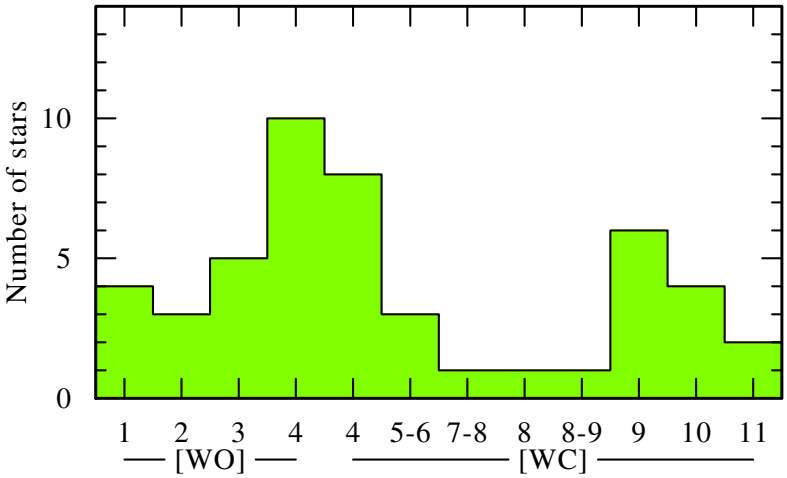

Figure 1.1: Distribution of the Wolf-Rayet type CSPNe over the subtypes according to Acker & Neiner (2003). The distribution appears to be bimodal. More "early" than "late" subtypes are detected. This may be the result of an observational bias: Spectra of [WO] and [WCE] stars show broader stellar lines than [WCL] stars. Therefore the stellar emission lines of [WCE] and [WO] stars can be distinguished more easily from the narrow nebular emission lines, which is necessary to detect an emission-line central star.

In the present work, we have re-analyzed systematically these [WC]-type central stars, using the most recent version of our non-LTE models for expanding atmospheres which now accounts for line blanketing by iron-group elements. So far we have revisited the early subtypes and a [WC5-6] intermediate subtype. We do not only focus on the determination of the most abundant elements, helium, carbon, oxygen, but also on tracer elements like neon and nitrogen predicted by the very late thermal pulse scenario. Moreover, the

stellar parameters are revisited. Accurate mass-loss rates are important for two issues: the stellar evolution and the nebula formation. If the mass loss is high the amount of fuel for helium shell burning diminishes and the star enters the WD cooling track earlier. Furthermore, in the interacting wind picture the formation of PN structures like the hot bubble depends on the wind momentum which is proportional to the mass loss rate.

1.3 Previous work

Since the work of Paczyński (1970), it has been widely accepted that a central star of a planetary nebula (CSPN) is a low mass star in an intermediate stage of its evolution. The central star has left the so-called asymptotic giant branch (AGB) and will soon end as a white dwarf (WD).

While AGB-stars are hydrogen-rich at their surface, there are detections of low mass stars, like CSPNe or WDs, which are considered to be descendants of AGB stars, displaying a hydrogen deficient surface composition.

In the following, we give a brief historical overview on the observation and theory of H deficient CSPNe and their descendants.

It has been long known that some of the CSPNe exhibit spectra very similar to those of the massive Wolf-Rayet stars, showing broad emission lines, and thus making it easy to identify them.

Already six examples were given by Smith & Aller (1969): NGC 40, Hen 2-99, NGC 5315, NGC 6751, M 1-67, BD+30°3639. Additionally, seven stars of the so called O VI sequence were mentioned, showing very strong emission lines of O VI $\lambda\lambda$ 3811, 3834. Nowadays, these O VI stars are classified as early [WC] stars ([WCE]), or more recently as [WO] stars (see introduction Sect. 1.1). This classification is purely phenomenological and refers to the strength of this specific O VI line. A [WO] star does not necessarily need to have a higher oxygen abundance on its surface than a [WC] star.

The earliest detections of emission-line central stars were confused with those of massive Wolf-Rayet stars. E.g. Keeler (1898) reported the discovery of a hydrogen envelope around the Wolf-Rayet star D.M.+30°3639 (BD+30°3639). Actually, this star is a WR-type central star and the "hydrogen envelope" is its planetary nebula.

Another example is Sanduleak 3 (alternative identifier: [Sd71d]3), discovered by Sanduleak (1971), which has been mistaken for a massive WC star (van der Hucht et al. 1981), as no PN was found around this object.

Applying a spectral classification scheme to a sample of 115 central stars of planetary nebulæ, Méndez (1991) found 38 of the CSPN to be hydrogen deficient.

With help of model codes which solve the radiative transfer equation in the comoving frame, i.e. appropriate for expanding atmospheres, it was then possible to perform quantitative analyses of [WC] stars, whose spectra are formed in strong stellar winds.

In the last years, a large number of [WC]-type central stars have been analyzed by means of non-LTE codes, most important to mention, the code CMFGEN, developed by Hillier (1990), and the Potsdam Wolf-Rayet model atmospheres (PoWR).

Although both codes were developed independently, the same assumption of spherical symmetry is made. While in earlier analyses also homogeneity of the wind was assumed, the recent versions of both codes account now for inhomogeneities in a first order approximation, the so called microclumping, and additionally for iron line blanketing.

1.3.1 Analyses of [WCL] stars

The spectral analyses of [WC] stars started with the analysis of the late-type [WC] star V 348 Sgr (Leuenhagen & Hamann 1994). They accounted for helium, carbon, and hydrogen, but not for oxygen, and derived chemical abundances of $X_{\rm He} = 41\,\%$ and $X_{\rm C} = 56\,\%$ (by mass fraction). The model calculations were performed for a homogeneous wind and did not account for iron line blanketing.

Due to the low temperature of 20 000 K that was restricted to an upper limit of 25 000 K from the weakness of C III absorption lines, the dominant ionization stage in the wind is He II. Hence, He II lines are predicted to appear only in absorption, and hydrogen lines are therefore not blended with He II emission lines from the Pickering series. From the Hα emission line, Leuenhagen & Hamann (1994) derived a hydrogen abundance of 4 %. Therefore, V 348 Sgr is hydrogen deficient, but not hydrogen free.

Analyses of a larger sample of [WCL] stars and accounting also for oxygen (Leuenhagen et al. 1996) resulted in an abundance pattern of roughly He:C:O=40:50:10 (cf. Table 1.1), similar to the results for V 348 Sgr. All stars of the sample are hotter than 30 000 K, thus, stellar emission lines of He II are expected in the spectrum. Hence, spectral lines from hydrogen may be blended with He II lines from the Pickering series with even principle quantum number.

Furthermore, the detection of stellar hydrogen lines is hampered by the presence of strong nebular hydrogen emission lines. Only in the case of Hen 2-113 the authors find a weak indication for the presence of stellar hydrogen, and give an upper limit of $X_{\rm H} \leq 7\,\%$. For the other sample stars, the given upper limits for the hydrogen content, ranging from 0.5 % up to 10 %, are much more uncertain.

Five more [WCL] stars were analyzed by Leuenhagen & Hamann (1998), and as the models included additionally neon, nitrogen, and silicon, most of the already analyzed [WCL] stars were revisited, with focus on the abundances of these elements.

Concerning the abundances of helium, carbon, and oxygen, the overall [WCL] star sample appears relatively homogenous, meaning to confirm the abundance pattern found by Leuenhagen et al. (1996).

At the same time, stellar evolutionary models which account for hydrodynamically-based overshooting during the 3$^{\rm rd}$ dredge-up, were published by Herwig et al. (1997). The given abundances for the intershell region of He:C:O=23:50:23 are relatively similar to the surface abundances found for the [WCL] stars.

For IRAS 21282+50 a mass fraction of 10 % hydrogen has been derived from the observed line profile of Hα (see Fig. 1.2), while for the other stars of the sample only upper limits for the hydrogen abundance were given.

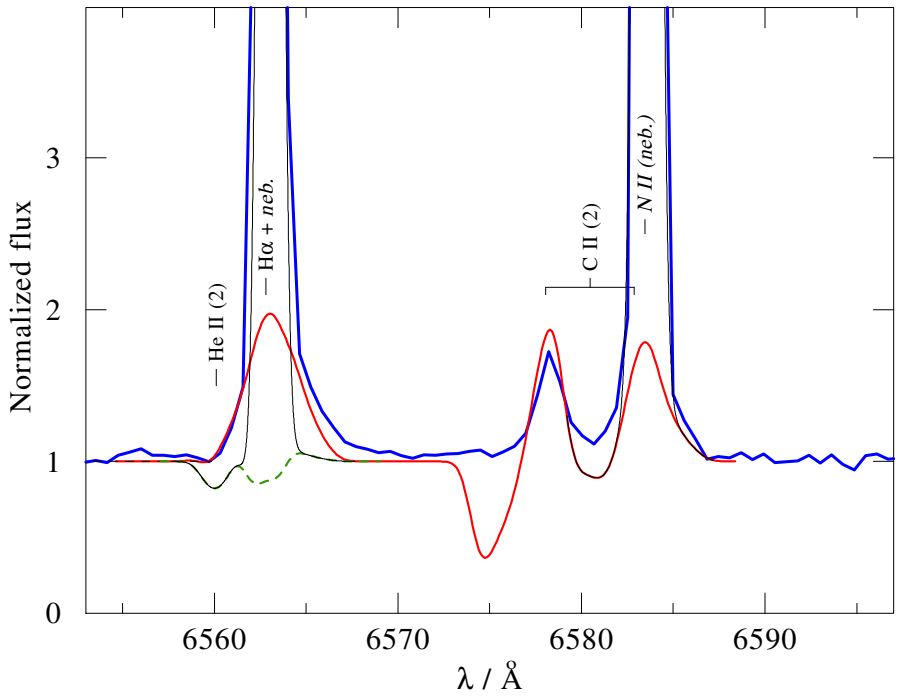

Figure 1.2: IRAS 21282+5050: observation (blue line) and model with 1.5 % H (green dashed) and with 10 % H (red solid), respectively. Also shown are the Gaussian fits to the nebula lines (black thin). The wings, in particular the red wing, of the Hα emission line appear stronger in the observation than expected from the Gaussian fit of the nebular line. Therefore the residual emission might originate from stellar hydrogen. Plot is adopted from Leuenhagen & Hamann (1998).

From N II and N III lines, nitrogen abundances between 0.1% and 1 % were derived, which is interesting, as evolutionary models for the formation of H deficient central stars predict a nitrogen enrichment in the case of a very late thermal pulse (Iben et al. 1983).

Additionally, silicon abundances in the range from less than 0.1 % (V 348 Sgr, IRAS 21282) up to $2-3$ % (PM 1-188) were found, although silicon overabundance is not predicted by the evolutionary calculations of Herwig et al. (1997).

Using CMFGEN, de Marco and co-workers reanalyzed the [WC 10] stars CPD -56°8032 and Hen 2-113 (De Marco et al. 1997; De Marco & Crowther 1998; De Marco et al. 1998). Their analyses resulted in C, He, and O abundances, and stellar temperatures very similar to those found by Leuenhagen et al. (1996) (cf. Table 1.1). Regarding hydrogen abundances and the fitting technique applied by Leuenhagen et al. (1996), De Marco & Crowther (1998) attributed the broad pedestal in the Balmer line profiles of Hen 2-113 to a nebular origin, thus refuting the detection of stellar hydrogen by Leuenhagen et al. (1996).

Actually, as already mentioned by Koesterke (2001), the determination of hydrogen

abundances is difficult in [WC] stars, as stellar H lines are blended with stellar He II lines and nebular H lines. Disentangling the various contributions requires observations with good spectral resolution and with good S/N ratio. The spectral resolution must be sufficient to tell stellar hydrogen lines, which are broadened by a wind with velocities down to $160\,\mathrm{km\,s^{-1}}$, from nebular lines which are broadened by expansion velocities of the PN in the range of $8 - 44\,\mathrm{km\,s^{-1}}$ (Medina et al. 2006). A high spectral resolution also helps to distinguish between the He II lines and the H lines. Moreover, the point spread function of the spectrograph might also induce line wings, which cannot be fitted by a simple Gaussian.

However, for M 4-18 De Marco & Crowther (1999) found Hβ emission wings, but attributed them, as well as for Hen 2-113, to high-velocity components of the nebular spectrum. Such high-velocity components were found e.g. for CPD-56°8032 by Sahai et al. (1993). There, the authors took maps and spectra of molecular lines for some PNe. From the full width at zero intensity of the CO $J = 2 - 1$ line, they derived a corresponding Δv of $186\,\mathrm{km\,s^{-1}}$. The width which is found for Hen 2-113 is twice this value ($\Delta v = 320\,\mathrm{km\,s^{-1}}$), but would be rather consistent with a wind broadened hydrogen emission line (cf. Fig. 1.3).

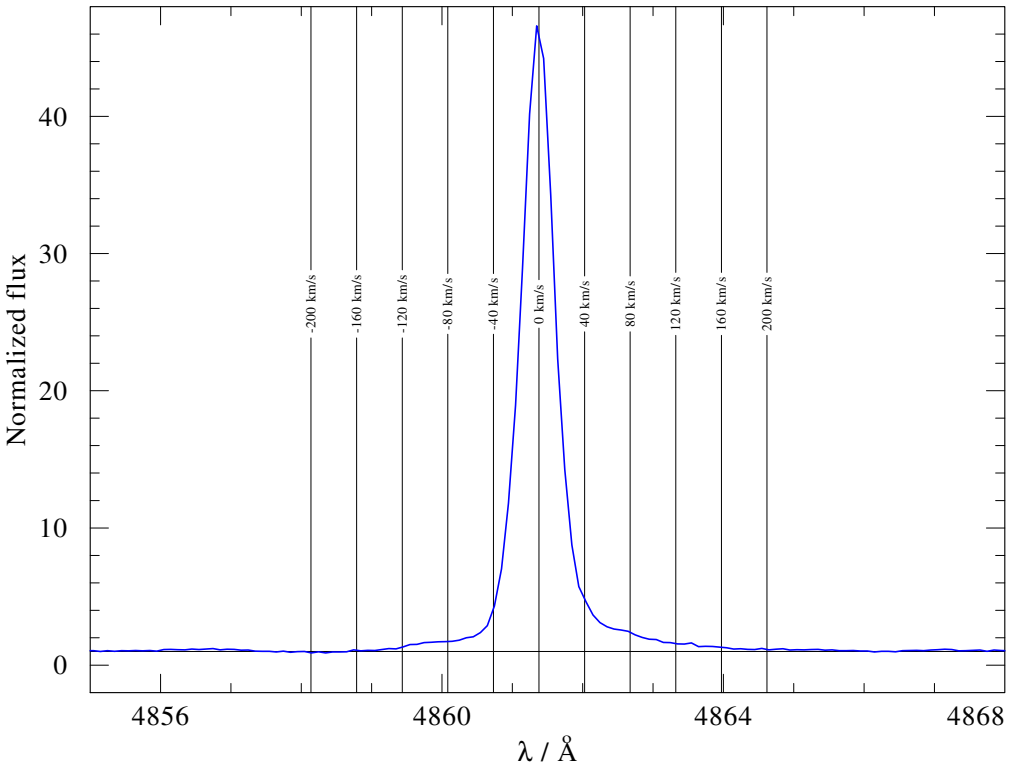

Figure 1.3: Hen 2-113: Hβ, shown together with a velocity scale.

Using two different codes that account for line blanketing by iron, De Marco et al.

(2001) derived for the [WCL] star SwSt1 two different He:C ratios, depending on which code is used for spectral modeling. From the analysis with CMFGEN the He:C ratio seems to be 53:32, very similar to the ratio found for [WCE] stars by Koesterke & Hamann (1997a), whereas the Sobolev approximation code ISAWIND, gives preference for a He:C ratio of 37:51 for the same object.

1.3.2 Analyses of [WCE] stars

Koesterke & Hamann (1997b) also analyzed early-type [WC] stars with temperatures above 100 000 K.

Their analyses of NGC 6751 and [S71d]3 resulted in He:C:O abundances of 54:31:15 and 62:26:12, respectively. They derived similar abundance ratios for other [WCE] stars (Koesterke & Hamann 1997a).

In the spectrum of [Sd71d]3 they also found nitrogen lines, and determined a nitrogen abundance of 0.04 % by mass.

Regarding the carbon to helium abundance ratio, analyses by the Potsdam group with unblanketed models, resulted in systematically different abundance patterns for early- and late-type [WC] stars (cf. Table 1.1 and Figure 1.7).

To check this discrepancy, Crowther et al. (2003) performed analyses of the [WCE] stars NGC 6751 and NGC 6905, and of the [WCL] stars NGC 40 and BD+30 3639 using line blanketed models from the CMFGEN code. Their analyses resulted in He:C:O abundances of roughly 50:40:10 for all of their sample stars. Hence, they claimed that the carbon abundances of [WCE] stars are not systematically lower than for [WCL] stars.

Similar analyses using CMFGEN were done by Marcolino et al. (2007) for the [WCE] stars NGC 6905 and NGC 5315, and for the [WCL] stars BD+30 3639 and NGC 40. While they found for NGC 6905 almost the same He:C:O abundances of 50:40:10 like Crowther et al. (2003), they determined He:C:O abundances of 40:50:10 for the other stars of their sample.

With line blanketed PoWR models, Stasińska et al. (2004) analyzed the early-type [WC] star LMC-SMP 61. They found He:C:O abundances of 45:52:3, which are very similar to those found for Galactic [WCL] stars by Leuenhagen & Hamann (1998). Moreover, from the weakness of the observed iron forest, Stasińska et al. (2004) found LMC-SMP 61 to be iron-deficient, with an upper limit for the iron group elements of 10^{-4} by mass (≈ 0.07 solar).

1.3.3 PG-1159 stars and white dwarfs

With larger telescopes, more sensitive spectrographs, and advanced observational techniques, the exploration of hydrogen-deficient low-mass stars with spectra dominated by absorption lines could be refined as well.

E.g., McGraw et al. (1979a,b) discovered the pulsation properties of PG 1159-035, that are similar to those of the pulsating white dwarfs, but with absorption lines of He, C,

and N, in combination with weak He II in emission. Similar objects have been found later and classified as PG 1159 stars according to their prototype.

Sion et al. (1985) found oxygen in five PG 1159 stars and claimed that the central star of the planetary nebula K 1-16 is also a PG 1159 star, establishing a link between hydrogen-deficient central stars of planetary nebulæ and the PG 1159 stars.

For the CSPNe A 66 30 (Abell 30) and A 66 78 (Abell 78), the indications of H deficiency were also found in the inner part of the nebula. There, an abundance ratio of He/H of about 6-10 (by number) was detected, indicating the ejection of the end product of the hydrogen-burning shell (Hazard et al. 1980; Jacoby & Ford 1983).

Based on these observations, Iben et al. (1983) suggested that some CSPNe experience a final thermal pulse at the start of the white dwarf cooling track that mixes the remaining hydrogen into the helium-burning convective shell, where it is completely burnt. From their model calculations Iben et al. (1983) deduce chemical surface compositions which are dominated by helium and carbon, but they also expect O and N enrichment.

With the advent of more appropriate non-LTE calculations for stellar atmospheres, first quantitative analyses of PG 1159 stars were performed by Werner et al. (1991). Their analysis confirms the presence of He, C, and N, and additionally O in the atmospheres of PG 1159 stars. The derived abundances (by mass fraction) are roughly as follows: 30 % He, 50 % C, 15 % O, and less than 0.4 % N, and 8 % H, tops.

1.3.4 Theory of the formation of hydrogen-deficient CSPN

The key to understand the formation of hydrogen deficient central stars are thermal pulses (TP), a thermal instability of the helium burning shell. TPs already occur during the asymptotic giant branch (AGB) phase, when the core helium burning has ceased but the stars still support both helium and hydrogen shell burning around the degenerate C/O core. As the hydrogen shell is located above the helium shell, the latter one is fed by the helium from the H-burning shell (see Fig. 1.4).

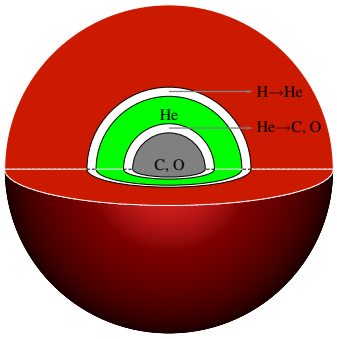

Figure 1.4: Sketch of an AGB star (not drawn to scale). Around the C/O core is the He-burning shell. Above the He shell lies the H-burning shell with the convective envelope on top.

In contrast to He-burning in a non degenerate core, He-burning in a shell is not stable, and thermonuclear runaways (Schwarzschild & Härm 1965), the so called thermal pulses (TP), occur repeatedly. The TP lasts until the He shell overexpands and cools. In the following longest part of the pulsation period, the H burning reignites. The thermal pulses have significant effects on the chemical structure of the star. The thermal pulse drives a convection zone that reaches from the C/O core to the intershell region and dredges He-burning products up. At the same time, H is mixed down to the core where it reacts with C to produce neutrons. These neutrons on the other hand can be captured by heavy elements, e.g. iron, in the s-process. Thus, AGB stars an very important source for elements with atomic numbers larger than iron, in fact they produce 50 % of the elements with nuclear numbers above 60.

AGB stars suffer heavy mass loss of up to $10^{-4} M_{\odot}\, a^{-1}$. When the cool envelope is lost, the former stellar core of the AGB star is displayed. Its surface temperature increases due to the contraction of the remaining envelope and the star evolves horizontally through the HRD. It becomes a white dwarf when helium and hydrogen burning have ceased. The evolutionary track in the HRD is plotted in Fig. 1.5 During this horizontal evolution, it can form a planetary nebula – usually with a central star of H-normal surface composition.

However, some of the central stars show hydrogen-deficiency. Following Herwig et al. (1999); Herwig (2001), there are at least three possible scenarios that result in a hydrogen-deficient central star. They vary in the time of occurrence of the last thermal pulse.

AFTP

If the last thermal pulse occurs just before the the star leaves the AGB (AGB final thermal pulse, AFTP), the dredge-up after the thermal pulse will dilute the H surface abundance and the star shows hydrogen deficiency with a small fraction of H left. Within the HRD, the star moves directly from the AGB regime through the phase of PNe and enters the white dwarf (WD) cooling branch before the next TP would occur. Hence, PNe ages are expected not to be different from those of H-normal O-type central stars.

LTP

If the time left of the pulsation period after leaving the AGB is not long enough for the star to finish its hydrogen-shell burning, the star will suffer a late thermal pulse (LTP) immediately before the exhaustion of the hydrogen-shell burning. By occurrence of the LTP, the star is thrown back to the post-ABG regime and evolves through the CSPN phase again. This is a so-called Born-Again scenario. In this case, the following dredge-up dilutes the surface material and thus leads to H depletion.

VLTP

A post-ABG star which has already ceased hydrogen burning and entered the white dwarf cooling track can still undergo a very late thermal pulse (VLTP). Then, there is no

entropy barrier and the hydrogen layer can be not only mixed completely downwards but also burnt in the presence of the intershell material, namely C, He and O. These stars will be born-again CSPNe completely lacking hydrogen.

The star is thrown back to the AGB regime (born-again) and becomes a hydrogen-free CSPN.

For the LTP and VLTP scenarios, it is expected to find a young PN within an older PN that originates from the first AGB phase.

Evolutionary tracks for all three scenarios are shown in Fig. 1.5.

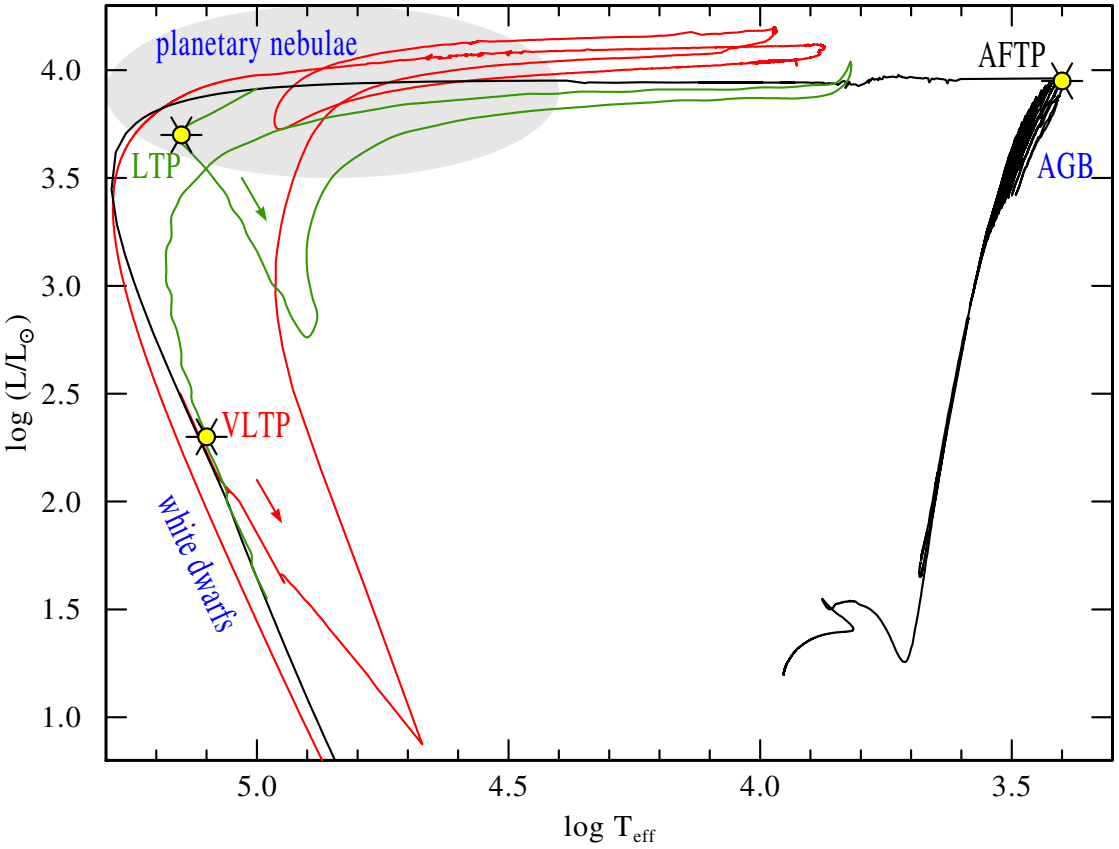

Figure 1.5: Hertzsprung-Russell diagram with evolutionary tracks for low mass stars. The black line represents a track for a star with $M_\mathrm{i} = 2\,M_\odot$, $Z = 0.02$ without any late thermal pulse (no-TP, Herwig 2005). It should also illustrate the evolution of a star which suffers an AFTP, as the tracks for both scenarios look very similar. For clarity, the tracks for LTP and VLTP are plotted in a way that they branch off from the track for the no-TP scenario. The late thermal pulse (LTP) scenario for a star with $M = 0.625\,M_\odot$ and $M_\mathrm{i} = 3\,M_\odot$ (Bloecker 1995) is illustrated by the green line. A VLTP is a final thermal pulse occurring on the WD cooling branch, represented by the red line (data from F. Herwig, 2006, priv. comm.).

Using codes that account for simultaneous burning and mixing, Herwig et al. (1999); Herwig (2001); Althaus et al. (2005) derived different abundance patterns for the stellar surface after the occurrence of an AFTP, LTP, or VLTP (see Fig. 1.6).

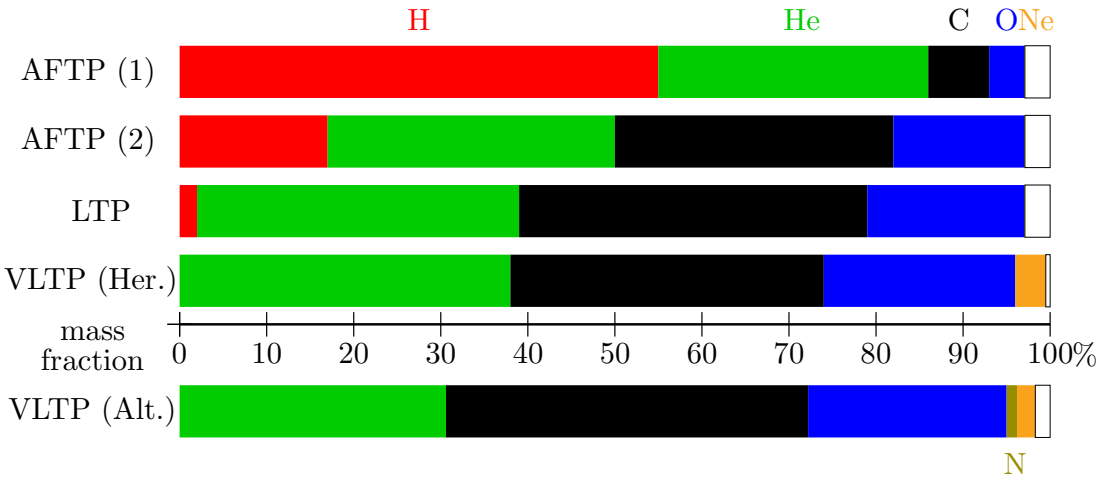

Figure 1.6: Results from models for the occurrence of the final thermal pulse in the different scenarios. Predicted abundances for an AGB final thermal pulse (AFTP), a late thermal pulse (LTP), and a very late thermal pulse (VLTP) in the upper panel from Herwig et al. (1999); Herwig (2001). In the AFTP(1) scenario, the envelope mass was $3 \times 10^{-2}\,M_{\odot}$ after the TP and before the dredge up, for AFTP(2) the envelope mass was $4 \times 10^{-3}\,M_{\odot}$. Predictions by Althaus et al. (2005) for a VLTP including the formation of neon an nitrogen are shown in the lower part.

1.3.5 Overview of previous [WC] analyses - Abundance patterns and the putative evolutionary sequence [WCL] → [WCE]

Hydrogen-deficient central stars have been analyzed by means of non-LTE codes to obtain stellar parameters and surface abundances. Stellar parameters suggested an evolutionary sequence from the cooler [WCL] stars with strong, slow stellar winds over the hot [WCE] stars and [WC]-PG 1159 stars with weaker, but faster winds to the PG 1159 stars, which show no more signs of stellar winds. This evolutionary link is not corroborated by the element abundances found for [WCL] and [WCE] stars: Analyses with unblanketed models resulted in systematically lower carbon abundances (30 % by mass on average) for [WCE] stars than for [WCL] stars (50 % on average), while analyses of PG 1159 stars found a broad range of carbon abundances (see Fig. 1.7).

At the moment, the correct carbon and helium abundances seem to be an open question (Marcolino et al. 2007), although these are the most abundant elements in [WC] winds.

For [WCL], wels, and PG 1159 stars, the He:C mass ratio seems to be 1:1 on the average with a large scatter in the case of the PG 1159 objects, whereas the He:C ratio

for [WCE] is 2:1.

The abundance discrepancy between [WCL] and [WCE] stars can result from systematic errors in the analyses as well: Different lines are used for [WCE] and [WCL] as they are located in different temperature regimes. If the difference is significant, this would be evidence against a unique evolutionary sequence.

In contrast to the apparent uncertain helium and carbon abundances, all analyses obtain similar abundances for oxygen, in the range of $1 \ldots 15\,\%$.

Furthermore, Leuenhagen & Hamann (1998) detected nitrogen and neon with abundances of a few percent in some of the [WCL] stars, which is super-solar and therefore must be processed material.

There is still no certain detection of s-process elements in [WC] star winds, although Stasińska et al. (2004) and Marcolino et al. (2007) observed iron-deficiency in some of the [WC] stars. This depletion can be explained as the result of iron consumption by neutron capture in the s-process nucleosynthesis.

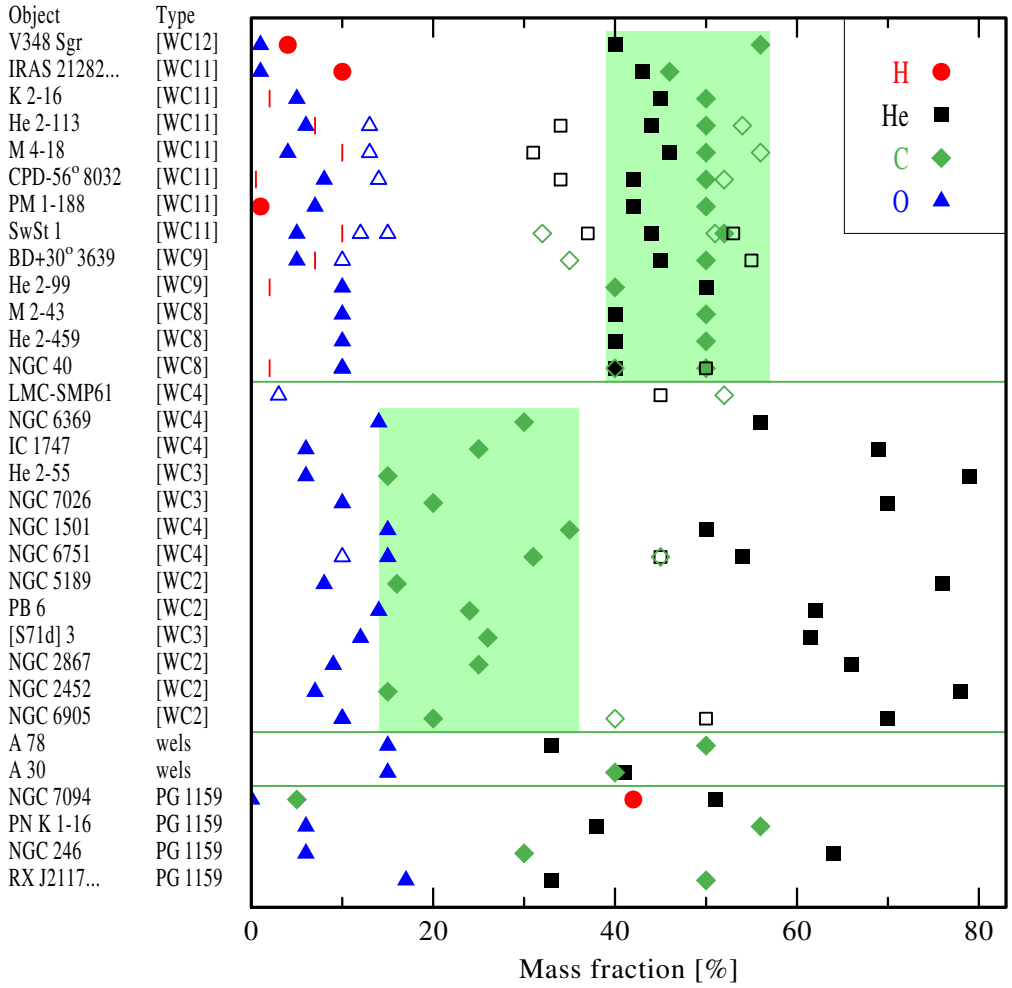

Figure 1.7: Surface abundances of hydrogen-deficient central stars. Filled symbols represent results from analyses with unblanketed models, while open symbols represent results from analyses with blanketed models. The diagram is from Hamann & Graefener (2005) and shows the status of analyses in 2004. The range of carbon abundances found for [WCE] and [WCL] stars with blanketed models is indicated by the green boxes. Note that the carbon abundances of [WCE] stars from analyses by Koesterke (2001) are systematically lower than for [WCL] stars.

Table 1.1: Results of previous analyses of [WC]-type central stars. References in column 7 can be found in Table 1.2, there it is also written, whether the models include micro-clumping and iron line blanketing. Values between parenthesis for $\log(R_\mathrm{t}/R_\odot)$ are obtained from models that include micro-clumping. Hydrogen abundances are not listed, but mentioned in Sect. 1.3.1.

object	type	C:He:O	T_*/ kK	$\log(\frac{R_\mathrm{t}}{R_\odot})$	v_∞	ref.	comment
NGC 2867	2	25:66: 9	141	0.6	1800	1	
PB 6	2	24:62:14	140	0.7	3000	1	
NGC 5189	2	16:76: 8	135	0.7	3000	1	
NGC 2452	2	15:78: 7	141	0.6	3000	1	
NGC 6905	2-3	25:60:15	141	0.5	1800	1	
		40:50:10	150	0.7	2450	2	
		40:49:10	150	0.7 (1.0)	1890	10	$\beta_\mathrm{N} < 0.1$
NGC 7026	3	20:70:10	131	0.8	3500	1	
Hen 2-55	3	15:79: 6	128	0.7	3000	1	
[S71d]3	3	26:42:12	140	0.5	2200	1, 8	
NGC 2371/2	3						
IC 1747	4	25:69: 6	126	0.8	1800	1	
NGC 1501	4	35:50:15	135	0.5	1800	1	
NGC 6369	4	30:56:14	150	0.3	1200	1	
NGC 5315	4	51:43: 6	76	0.81 (1.1)	2400	10	$\beta_\mathrm{N} < 0.1$, [Fe]< 1
NGC 6751	4	31:54 15	135	0-0.4	1600	8	
		45:45:10	140	0.18	2350	2	
NGC 40	8	50:40:10	78	0.3	1000	5	
		40:50:10	90	0.44	1100	3	
		51:43: 6	73	0.53 (0.87)	1000	10	$\beta_\mathrm{N} < 0.1$
Hen 2-459	8	50:40:10	77	0.3	1000	6, 9	
M 2-43	8	50:40:10	65	0.6	850	6, 9	
Hen 2-99	9	40:50:10	49	0.8	900	5	
BD+30 3639	9	50:45: 5	47	0.7	700	5	
		35:55:10	55	0.52	650	3	
		51:43: 6	48	0.83 (1.1)	700	10	$\beta_\mathrm{N} < 0.2$, [Fe]< 1
SwSt 1	9	53:44: 3	35	1.4	400	6, 9, 9b	$\beta_\mathrm{N} < 0.5$, $\beta_\mathrm{Ne} = 2-4$, $\beta_\mathrm{Si} = 1-2$
		51:37:12	40	1.8	900	11	(ISAWIND)
		32:53:15	46	1.7	800	11	(CMFGEN)
PM 1-188	11	50:42: 7	35	0.8	360	6, 9, 9b	$\beta_\mathrm{N} = 1$, $\beta_\mathrm{Ne} = 2-4$, $\beta_\mathrm{Si} = 2-3$
Hen 2-113	11	50:44: 6	30	1.1	200	5, 9b	$\beta_\mathrm{N} = 0.5$, $\beta_\mathrm{Si} = 0.5-1$
		54:34:13	31	1.0	160	7	
K 2-16	11	50:45: 9	30	1.3	300	5, 9b	$\beta_\mathrm{N} > 1$, $\beta_\mathrm{Ne} > 4$, $\beta_\mathrm{Si} = 0.5-1$
CPD-56°8032	11	50:42: 8	30	0.9	240	5, 9b	$\beta_\mathrm{N} < 0.1$, $\beta_\mathrm{Si} = 0.5-1$
		52:34:14	35	0.5	225	7	
M 4-18	11	50:46: 4	31	1.1	350	5, 9b	$\beta_\mathrm{N} < 0.5$, $\beta_\mathrm{Si} = 0.5-1$
		56:31:13	31	0.9	160	3	
IRAS 21282	11	46:43: 1	28	1.7	180	9, 9b	$\beta_\mathrm{N} < 0.5$, $\beta_\mathrm{Si} < 0.1$
V 348 Sgr	12	55:40: 1	20	1.7	190	4, 5, 9b	$\beta_\mathrm{N} = 0.5-1$, $\beta_\mathrm{Ne} = 2$, $\beta_\mathrm{Si} < 0.1$

Table 1.2: References to Table 1.1.

nr.	ref.	comment
1	Koesterke & Hamann (1997a)	
2	Crowther et al. (2003)	$f = 0.1$; blanketed models
3	De Marco & Crowther (1999)	
4	Leuenhagen & Hamann (1994)	
5	Leuenhagen et al. (1996)	
6	Leuenhagen & Hamann (1998)	
7	De Marco & Crowther (1998)	
8	Koesterke & Hamann (1997b)	
9	Leuenhagen (1997b)	
9b	Leuenhagen (1997a)	
10	Marcolino et al. (2007)	$f = 0.1$; blanketed models
11	De Marco et al. (2001)	$f = 0.1$, but not applied; blanketed

2 Methods

Spectral modeling

To derive parameters from the emission line spectrum of the central star we employ the Potsdam Wolf-Rayet (PoWR) models of expanding atmospheres. The PoWR code solves the non-LTE radiative transfer in a spherically expanding atmosphere, simultaneously with the statistical equations while accounting for energy conservation. Iron-line blanketing is treated by means of the superlevel approach (Gräfener et al. 2002), and wind clumping in first-order approximation is taken into account (Hamann & Gräfener 2004). We do not calculate hydrodynamically consistent models, but assume a velocity field following the β-law with $\beta = 1$. The model calculations in this work account for the hydrogen, helium, carbon, oxygen, nitrogen, phosphorus, and the iron-group elements.

Once the synthetic stellar spectra are calculated, they include simulated interstellar absorption before we are finally able to compare them with the observations. To account for the reddening, we apply the extinction law of Cardelli et al. (1989). Interstellar line absorption in the FUSE range is calculated for H_2 with the templates from McCandliss (2003), and for the Lyman lines following Groenewegen & Lamers (1989).

Spectral fitting

As the emission-line spectrum of a Wolf-Rayet star is mainly formed in its wind by recombination processes, the continuum-normalized spectrum shows a useful scale-invariance: for a given stellar temperature T_* and chemical composition, the equivalent widths of the emission lines depend in first approximation only on the ratio between the volume emission measure of the wind and the area of the stellar surface. An equivalent quantity, which has been introduced by Schmutz et al. (1989), is the *transformed radius*

$$R_\mathrm{t} = R_* \left[\frac{v_\infty}{2500\,\mathrm{km\,s^{-1}}} \Big/ \frac{\dot{M}\sqrt{D}}{10^{-4}\,\mathrm{M_\odot\,a^{-1}}} \right]^{2/3} . \tag{2.1}$$

Thus, different combinations of stellar radii R_* and mass-loss rates $\dot{M}$ can lead to the same strength of the emission lines. In the form given here, the invariance also includes the micro-clumping parameter D which is defined as the density contrast between wind clumps and a smooth wind of same mass-loss rate. Consequently, a mass-loss rate derived empirically from fitting the emission-line spectrum depends on the adopted value for D. The latter can be constrained from fitting the extended wings of strong emission lines which are formed by electron scattering (e.g. Hamann & Koesterke 1998a).

3 Analyses of [WC] stars

3.1 Parameters of [WCE]-type central stars

For first orientation, a grid of [WCE]-type model atmospheres was calculated. The following parameters are kept constant for the whole grid:

- The luminosity of $\log(L/L_\odot) = 3.7$ ($5000\,L_\odot$). This value is chosen according to earlier analyses by Koesterke (2001). Note that for the analyses of PB 8 and PMR 5 a luminosity of $6000\,L_\odot$ is assumed, according to Schönberner et al. (2005b); Miller Bertolami & Althaus (2007).

- The stellar mass of $M = 0.6\,M_\odot$. The value of M has no noticeable influence on the synthetic spectra. However, we chose $0.6\,M_\odot$ as this is the mean of the distribution of CSPN masses, presented by Tylenda (2003), see Fig. 3.30.

- The terminal velocity of $v_\infty = 2000\,\mathrm{km\,s^{-1}}$. This is a typical value found for most [WCE] stars (cf. Table 1.1).

- The density contrast $D = 10$, corresponding to a volume filling factor of $f = 0.1$. In the absence of precise determinations of f, most authors refer to this value, e.g. Marcolino et al. (2007), see also Sect. 3.2.

- The chemical composition He:C:O:Fe=60:30:10:0.16 by mass. The He/C abundance ratio is derived from the diagnostic line pair, see Sect. 3.3.1. An oxygen abundance of roughly 10 % was found for all [WCE] and most [WCL] stars in previous analyses (cf. Table 1.1). The iron group elements, Sc, Ti, V, Cr, Mn, Fe, Co, and Ni, are included with solar metallicity (Gräfener et al. 2002), and are always referred to as "Fe". By default, only the ionization stages Fe III up to Fe X are included in the models. The first and the last ionization stages are not complete, each of them consists only of one level. As in previous analyses, no hints of hydrogen in [WCE] stars were found, thus we do not account for it within in the model grid. Nitrogen and neon are expected with abundances between zero and a few percent. Moreover, some ions of these elements have a complicated structure with thousands of spectral lines. Thus, their consideration in the model atmosphere can slow down model calculations substantially. Hence, our strategy was to first find the best fitting model within our [WCE] grid and then calculate models that include these elements, if necessary. We do not account for any other element.

3.1.1 Determination of T_* and R_t

The grid spans a temperature range from $\log(T_*/\mathrm{K}) = 4.85$ to $\log(T_*/\mathrm{K}) = 5.30$ in steps of $\Delta\log(T_*/\mathrm{K}) = 0.05$, and the range for the transformed radius runs from $\log(R_t/R_\odot) = 2.0$ to $\log(R_t/R_\odot) = -0.5$ with $\Delta\log(R_t/R_\odot) = 0.1$.

This spacing reflects the relation for the parameter degeneracy for WC star atmospheres, described by Hamann et al. (2003). They mention that for hot, dense stellar winds [1] of WC stars with $T_* > 100\,\mathrm{kK}$ and $R_t \lesssim 2.5\,R_\odot$, contours of equivalent widths in the R_t-T_* plane align with $R_t \sim T_*^{-2}$, meaning that only one free parameter is left, which is defined as

$$R_{t100kK} = R_t \left(\frac{T_*}{100\,\mathrm{kK}}\right)^2 \tag{3.1}$$

Their explanation of the parameter degeneracy is that in "dense" winds all emergent radiation escapes from fast moving layers, with velocities close to v_∞.

Then, for a given opacity, the density structure and hence the optical depth scale depends only on $\dot{M}/v_\infty$. The temperature structure, in addition, is fixed by the requirement of a luminosity L. Hence, models depend only on two parameters, L and $\dot{M}$ (v_∞ fixed). Note that constant $\dot{M}$ implies $R_t \sim T_*^{-2}$.

The same parameter degeneracy is also found in a moderate form for less dense models along lines of $\log R_t \sim -2\log T_*$, i.e. along lines with same $\dot{M}$, see e.g. Fig. 3.8, left panel.

The relative strength, i.e. the equivalent widths or the peak height normalized to the continuum, of most of the spectral lines is almost the same along these lines, as long as T_* is above some specific value. Then, a higher temperature can be compensated by an appropriate reduction of R_t to obtain the same line strengths. For the hot [WCE] stars, the spectrum is dominated by C IV and He II (recombination) lines, as helium is completely ionized (He III) and carbon exists predominantly as C V throughout the stellar wind. Hence, the derived T_*, usually determined with help of spectral lines from different ions of the same element, is more uncertain as for [WCL] stars.

De Marco (2002) refers to it as an ambiguity of the stellar temperature in the case of [WC] CSPN, but attributes it to the different atomic data used for analyses and our lack of knowledge of the velocity law of Wolf-Rayet stars, as the wind is generally not modeled hydrodynamically consistent. Although this cannot be dismissed, the spectra of not too dense [WC] winds along these T_*^{-2}-lines do not look exactly the same, as the "degeneracy" does not exist for all of the spectral lines, usually not for the oxygen lines. As an example one may have a look on the sequence shown in Fig. 3.1, showing three different models with almost the same line strengths for most of the spectral lines but not for all lines.

[1] By definition, "dense" winds are those with $\log(R_t/R_\odot) < 10.8 - 2\log(T/\mathrm{K})$, or, in other words, those with $\frac{1}{2}v_\infty$ at $\tau_{\mathrm{Ross}} \geq \frac{2}{3}$

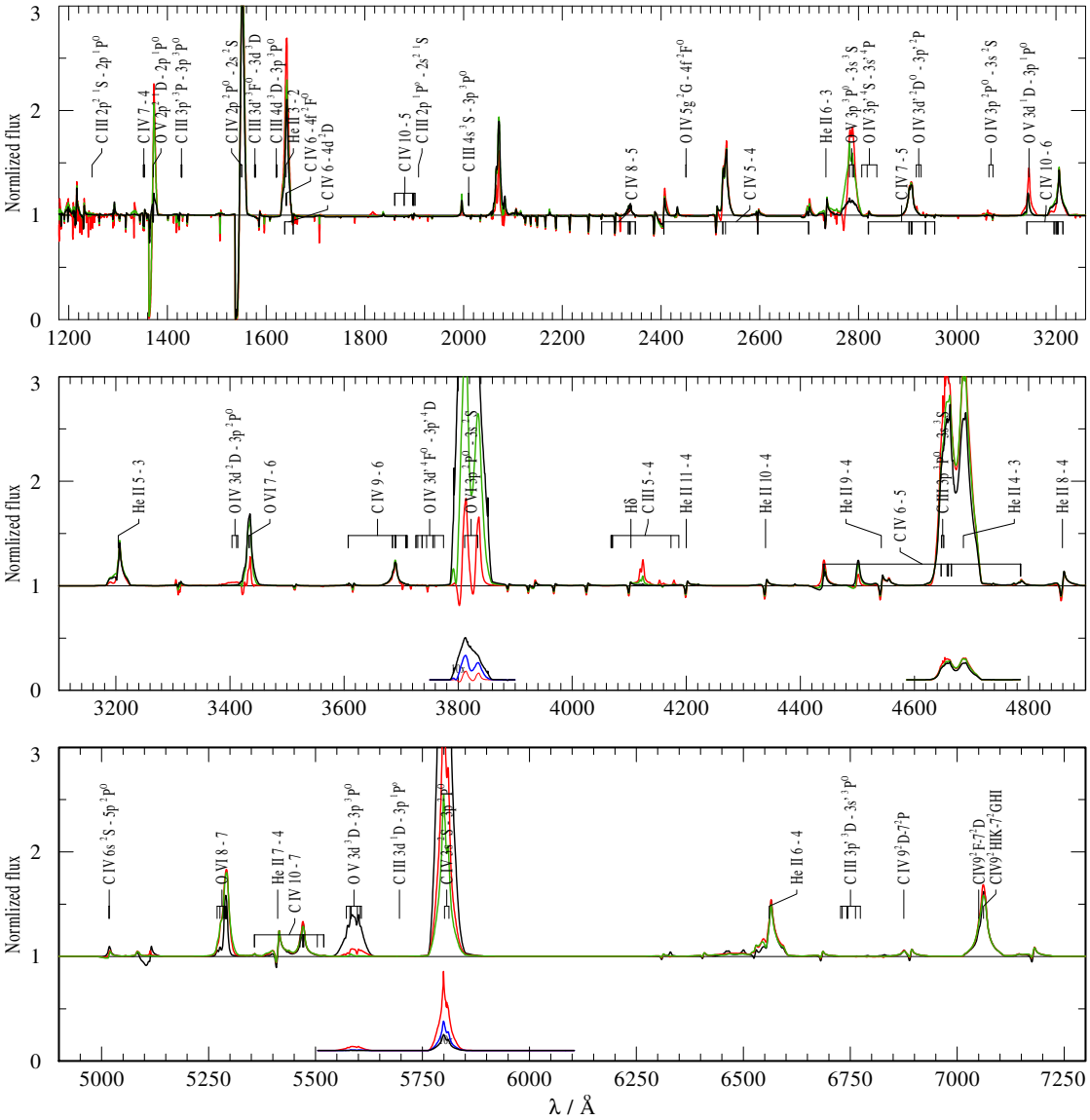

Figure 3.1: Sequence of three models (grid numbers) along a T_*^{-2}-line in the $(T_* - R_t)$-plane: $\log(T_*/\mathrm{K}) = 5.05, \log(R_t/R_\odot) = 1.1$ (black lines); $\log(T_*/\mathrm{K}) = 5.10, \log(R_t/R_\odot) = 1.0$ (red); $\log(T_*/\mathrm{K}) = 5.15, \log(R_t/R_\odot) = 0.9$ (green). The diagnostic line pair C IV-He II, and most of the other spectral lines show almost equal line strengths for all three models. However, some of the spectral lines, e.g. the oxygen lines obviously look different, thus breaking the "weak degeneracy".

Hence, when determining T_* and R_t we rely mostly on the O V and O VI lines, in particular the strength of the O VI 3811/34 Å line, although this line is strongly affected

by line blanketing (cf. Sect. 3.3.2). The C IV 5805 Å line is also a very sensitive to changes in T_* and R_t.

3.2 Clumping in the winds of [WC]-type central stars

While there is strong evidence for clumping in the winds of massive hot stars, very little is known about clumping in the winds from Central Stars. We have checked [WC]-type CSPN winds for clumping by inspecting the electron-scattering line wings. At least for three stars we found indications for wind inhomogeneities.

Grosdidier et al. (2002) observed large-scale inhomogeneities, so-called blobs, via the line profile variability at a time scale of hours, which is comparable with the flight time of the clumps.

Hillier (1991) showed for WR atmospheres that clumpiness can be estimated from the strength of electron-scattering line wings. Clumps are defined by an enhanced density, so that $\varrho_{\mathsf{clump}} = D \cdot \overline{\varrho}$ with the clumping factor D. The empirical mass-loss rates scale with the adopted $D^{-1/2}$. Hamann & Koesterke (1998b) found $D \approx 4$ for WN stars and even higher values of D for WC stars.

Although the spectra of [WC] Central Stars resemble those of massive WC stars, the clumping of their winds is not well investigated. Koesterke & Hamann (2002) derive $D \gtrsim 4$ for Sand 3, which is assumed to be a former Central Star with a dissolved nebula. For O-type, hydrogen-rich CSPN Kudritzki et al. (2006) find $D = 1 \ldots 50$ from the relative strengths of Hα and He II 4686Å lines.

Electron-scattering (e.s.) wings in [WC] spectra are difficult to measure. The stellar spectra are contaminated by nebular lines which often outshine the e.s. wings.

The uncertainty of the stellar continuum is often comparable with the strength of e.s. wings. Moreover the e.s. wings in [WR] CSPNe spectra are weaker than for massive stars of same spectral type due to the different scaling properties of the line emission and the e.s. wings (providing a potential way to discriminate between [WR] CSPN and massive WR stars).

In spite of the problems mentioned before, we found evidence for wind clumping in three early-type [WC] stars NGC 6751, NGC 5189, and NGC 1501. For these stars, homogenous wind models yield e.s. wings that are definitely stronger than observed. The clumping contrast D is constrained to values higher than 4. To achieve comparability to the results of other [WC] analyses, we choose a value of 10. By the way, Gräfener et al. (2008) suggested a clumping factor of $D = 100$ to obtain a hydrodynamically consistent model for the stellar wind of NGC 6905. Although such values cannot be excluded from our spectral analyses, one should consider results of hydrodynamic modelling to be rather preliminary.

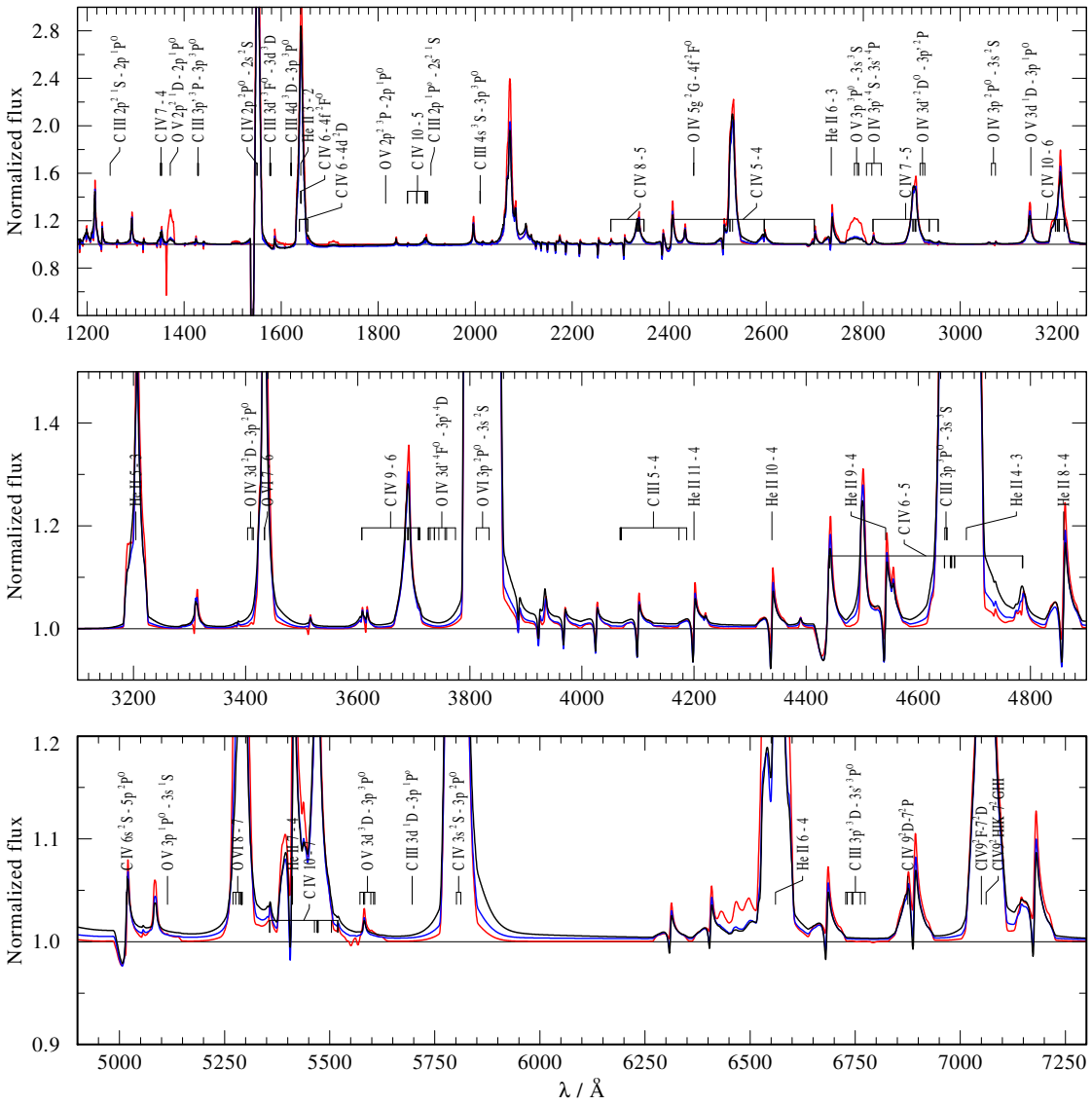

Figure 3.2: PoWR model spectra for [WCE] CSPN with different density contrasts $D = 1$ (black line), $D = 4$ (blue line), $D = 16$ (red line) but same $\dot{M}\sqrt{D}$ and $T_* = 158\,\mathrm{kK}$, demonstrating the impact of different values of the density contrast. The electron-scattering wings of strong lines are weaker for stronger wind clumping.

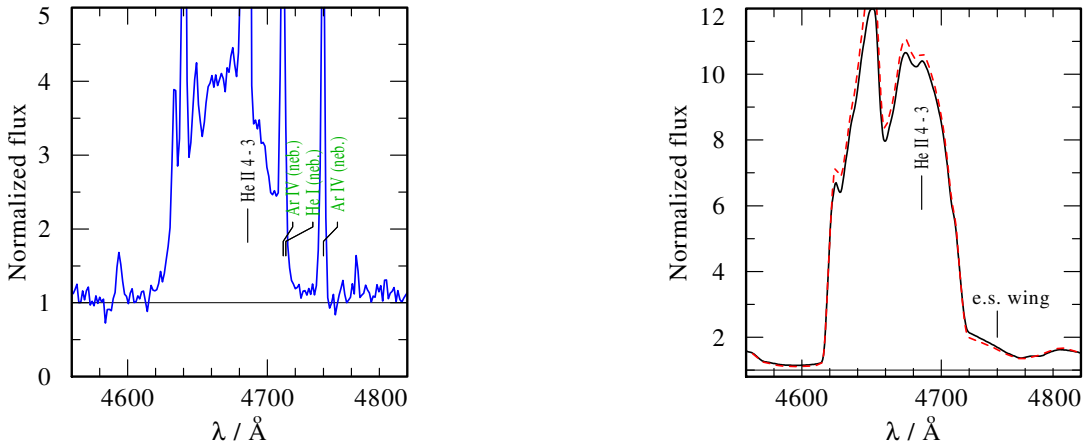

Figure 3.3: NGC 7026 (left panel), observed spectrum: nebular lines mask e.s. wings. PoWR model spectra (right panel) for same T_*, R_t but different D and luminosity, $\log(L/L_\odot) = 3.7$, $D = 1$ (black solid) and $\log(L/L_\odot) = 5.3$, $D = 10$ (red dashed), showing similar strength of e.s. wings.

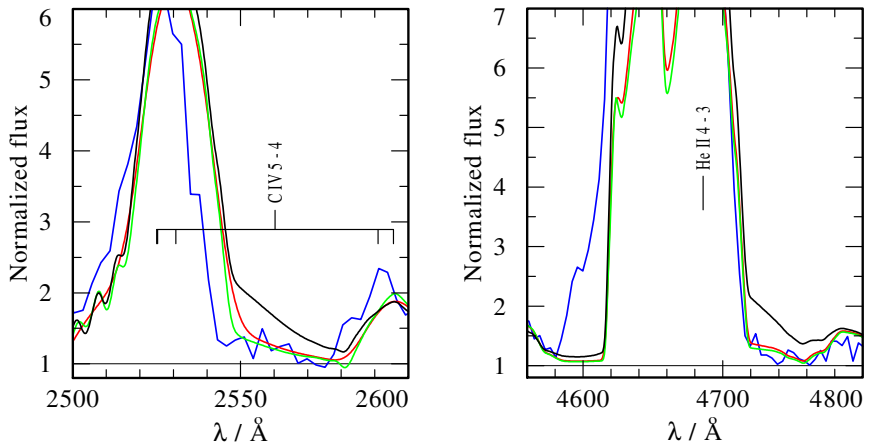

Figure 3.4: NGC 6751, type [WC4]: Observation (blue line) with PoWR models: no clumping (black), $D = 10$ (red), and $D = 16$ (green) clumping. The model without clumping can be excluded.

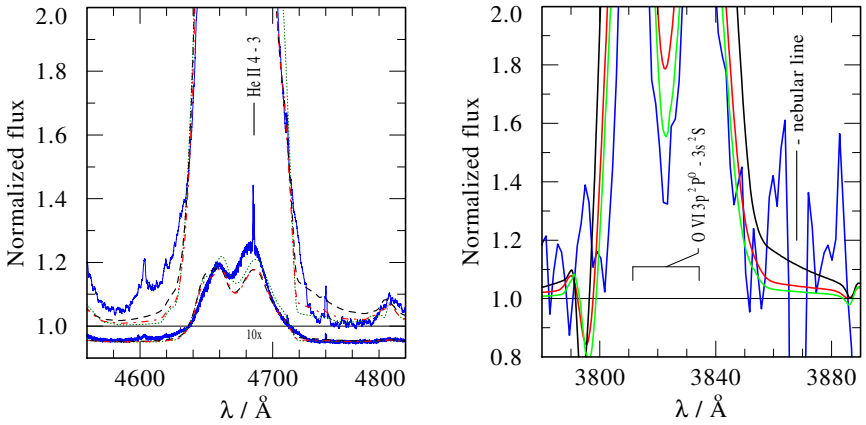

Figure 3.5: Left panel: NGC 5189: Observation (blue solid) and PoWR models without clumping (black dashed), $D = 10$ (red dashed-dotted) and $D = 16$ (green dotted). Right panel: NGC 1501 with same colors as in Fig. 3.4.

3.3 Chemical abundances of [WC] CSPNe and spectroscopic diagnostics

As pointed out, the determination of chemical abundances is key to understand the evolutionary channel by which the H-deficient CSPNe were created. Different scenarios - LTP, VLTP, AFTP - lead to different abundances.

3.3.1 Carbon and Helium

The strongest lines in a [WC] stellar spectrum arise from carbon and helium. It should be easy to determine their abundances, but as shown before, different authors and atmosphere model codes result in extremely different carbon and helium abundances for the same star. Therefore a reliable diagnostic tool for the He:C ratio is needed.

Diagnostic line pair He II 5412 and C IV 5470

Analogously to spectral analyses of massive WC stars, the carbon-to-helium ratio can be determined from the ratios of line strengths of the diagnostic line pair He II 5412 and C IV 5470, at least for the hotter [WC] stars. The ratio of the line strengths is more sensitive to the abundance ratio of helium to carbon (see Fig. 3.6) than to T_* or R_t.

This is due to the fact that the conditions for the formation of both lines are similar, so both lines form at the same location in the atmosphere. This can be illustrated by the quantity ξ, introduced by Hillier (1987) as

$$\xi \quad = \quad N_\mathrm{u}(r) r^3 \int_{-1}^{+1} \beta(\mu) \exp[-\tau_\mathrm{c}(\mu)] d\mu \tag{3.2}$$

with the escape probability β in Sobolev approximation. This describes the line emission per radial shell and thus makes sense only for emission lines. The energy emitted in the line is $E \sim \int_{R_\mathrm{core}}^{\infty} \xi d(\log r)$, and ξ is therefore normalized by division through the line energy. In Fig. 3.7 the normalized ξ is plotted for the diagnostic lines.

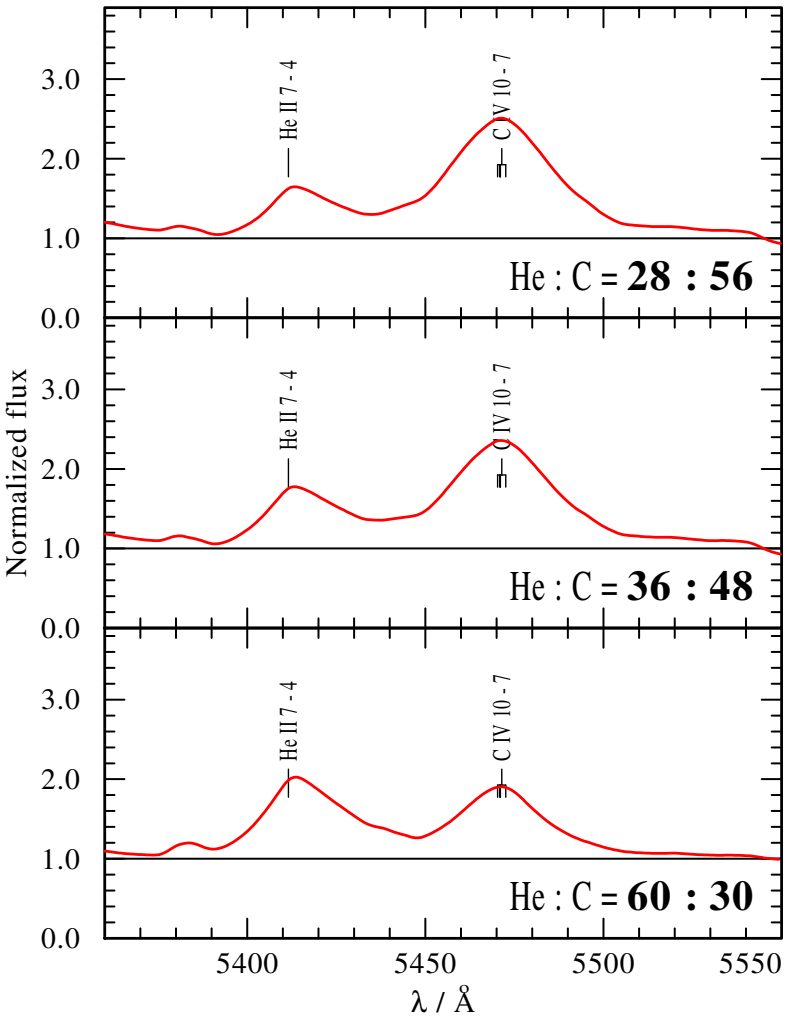

Figure 3.6: The pair of neighboring lines He II 5412 and C IV 5470 for models with different He:C mass ratios as given in the plots, while all other parameters are the same for the whole model series. Roughly equal line strength is only achieved for a He:C mass ratio of about 2:1.

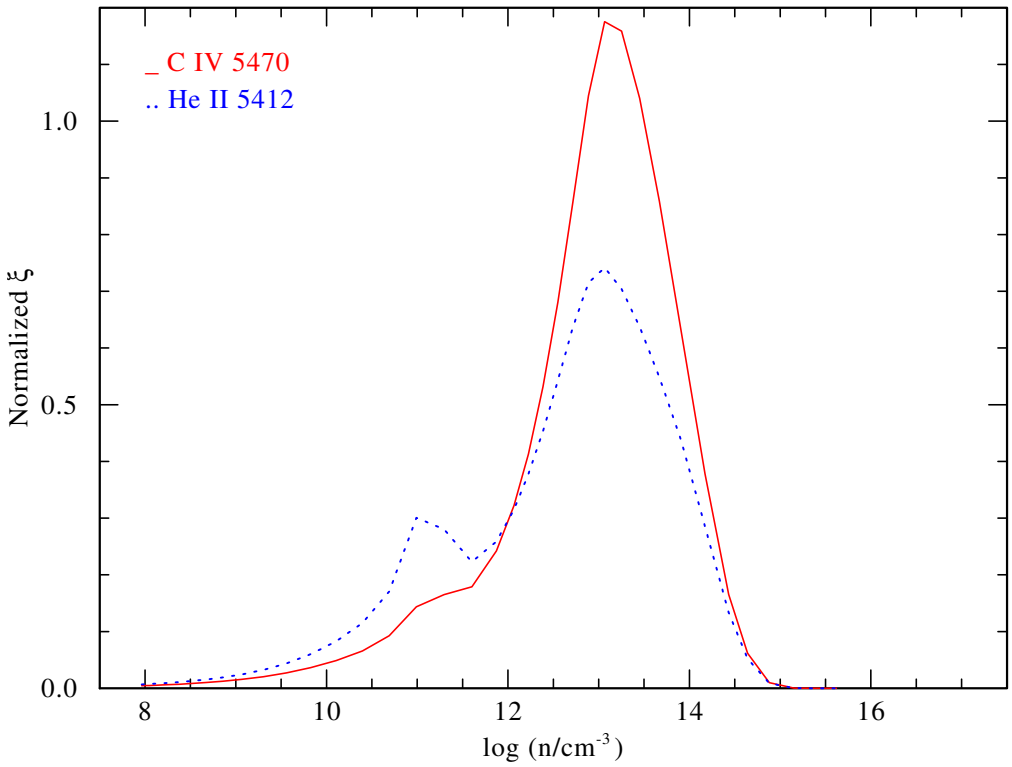

Figure 3.7: Line forming region of the He II $7-4$ (blue dotted) and the C IV $10\mathrm{g}\,^2\mathrm{G}$ - $7\mathrm{f}\,^2\mathrm{F}^\mathrm{o}$ (red solid) emission lines, from a [WCE] model atmosphere with $T_* = 158\,\mathrm{kK}$ and $\log(R_\mathrm{t}/R_\odot) = 0.7$. Plotted is the normalized ξ over the number density within the stellar wind as indicator of the radial location, the outer boundary is left, the stellar core is on the right. Both lines form in about the same layers.

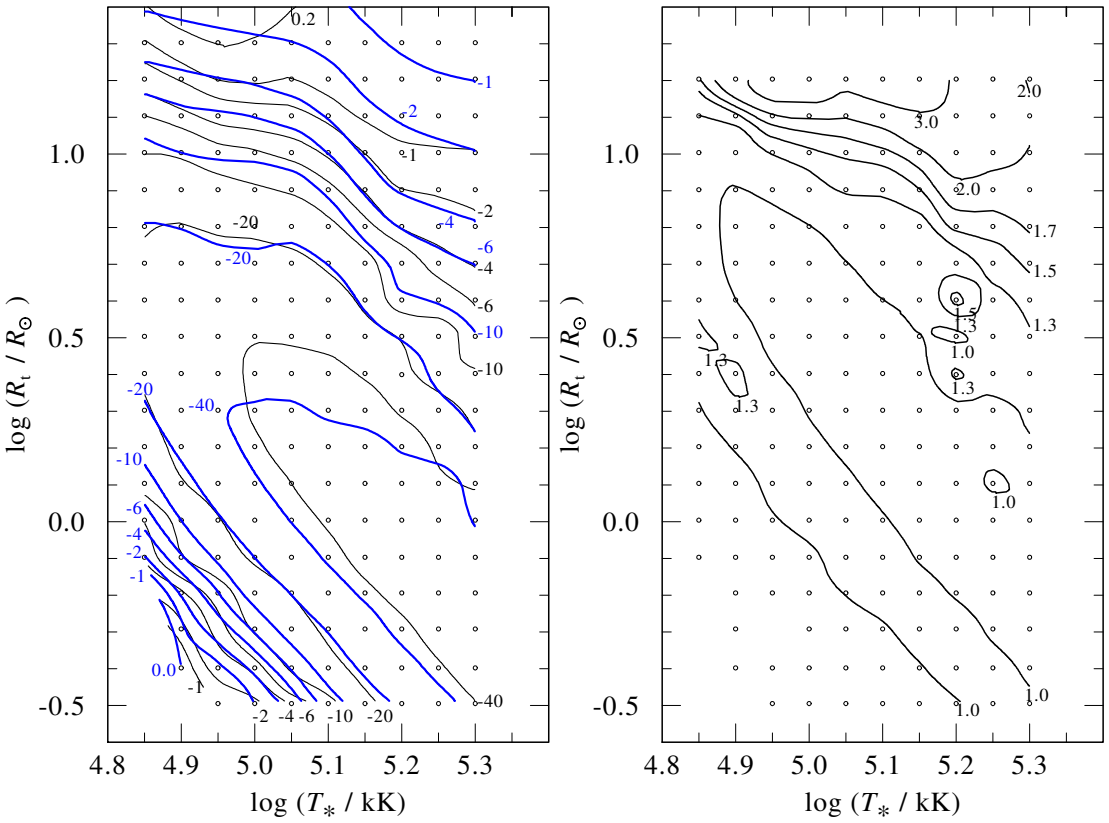

Figure 3.8: Contour plot of equivalent widths (left panel, labels in Å) for C IV 5470 (blue thick line) and He II 5412 (black thin) over the model grid (C:He=30:60). In the interesting range, the contour lines of both spectral lines are almost aligned. Therefore the ratio of the equivalent widths of both lines depends only weakly on T_*, R_t, as shown in the contour plot of the ratio (right panel), giving a robust measure for the carbon to helium ratio.

3.3.2 Oxygen

For the hot [WC] stars, there is only a small number of strong spectral lines from oxygen, mostly O VI and O V. For [WCE] stars, our abundance determination is based on the oxygen lines given in Table 3.1.

Table 3.1: Spectral lines from oxygen, used for determination of the oxygen abundance.

Ion	transition	wavelength [Å]
O VI	7 - 6	3434
O VI	8 - 7	5291
O VI	10 - 8	4500.2
O V	$3d\,^3D$ - $3p\,^3P^o$	5580

The O VI 3811/34 Å line

The hottest [WC] stars are classified as [WO]-types according Acker & Neiner (2003), where the presence of the strong O VI 3811/34 Å line is the main criterion. The line is formed by the transition $3p\,^2P^o$ – $3s\,^2S$. Equivalent widths of −250 Å up to −400 Å are observed for the [WCE] stars [S71d]3, NGC 2867, NGC 5189, PB 6, and NGC 6905.

First unblanketed PoWR models, as e.g. shown in Koesterke (2001), failed to reproduce this line with the observed strength. Even by models of higher temperatures ($T_* = 170$ kK) the observed strength cannot be reproduced.

However, by accounting for iron-group elements, and in particular by inclusion of the ionization stages above IX, it is possible to reproduce the observed emission line strength of O VI. The opacity of the higher iron-group ions alters considerably the ionization stratification of oxygen. Especially in the outer parts of the model atmosphere, the population numbers of O VI levels are increased on cost of the O VII ground state (see Figure 3.9).

To explain the anomalous strength of the O VI 3811/34 Å emission line, it is suggested that this is an effect of fluorescence due to iron lines. For the line forming region, we checked the rates of the transitions that have the upper level of the 3811/34 Å line, O VI $3p\,^2P^o$, as their target. We found the highest rate for the transition from the ground state 2s, which is 200 times larger than than the next smaller rate. However, the 2s-3p rate for the upward going transition is fully balanced by the competing downward transition (both transitions are radiative transitions, corresponding to a wavelength of ca. 150 Å). Moreover, the rates are smaller for the model with the stronger O VI 3811/34 line. Regarding the difficulty to interprete the processes in a multi-level atom, the effective process driving the O VI 3811/34 line remains unclear.

O VII and higher ions

Although some authors claim the discovery of spectral lines from O VII, e.g. Feibelman (1999), our models fail to reproduce such features even for the hottest stars in the sample. In the case of the alleged O VII 1522 Å line, it should be mentioned that the data quality of the IUE spectra is very poor for most of the considered targets and a definite distinction between noise and spectral features is often questionable. Some of the identifications of e.g. O VIII have been already revised to Ne VIII instead (Werner et al. 2007).

3.3.3 Hydrogen

In principle H abundances could discriminate between the scenarios, but the H lines are always blended with He II and nebular emission. Small amounts of hydrogen have been found in some [WCL] stars, while some PG 1159 stars – presumably also evolutionary related to the [WC]-type central stars – show even more hydrogen. In the hot [WCE] stars, a possible spectral signature from hydrogen would be weak. For our [WCE] program stars we can establish an upper limit of 5 . . . 10% for the hydrogen mass fraction (see also Sect. 3.4.3).

3.3.4 Nitrogen

In our models for [WCE] stars, the conditions (high T_*, thin winds) are usually sufficient to ionize nitrogen to N VI throughout the wind. Hence, spectral lines from N V may be visible for sufficiently large nitrogen abundances.

N V lines that are sufficiently strong for an identification can be found in the UV and optical range (cf. Table 3.2). These lines are also visible in the Galactic WN stars (e.g. Hamann et al. 2006), which have a nitrogen abundance of 1.5 % by mass.

Table 3.2: Spectral lines from N V.

Ion	transition	$J_\mathrm{u} - J_\mathrm{l}$	wavelength [Å]
N V	$2\mathrm{p}\,^2\mathrm{P^o}$ - $2\mathrm{s}\,^2\mathrm{S}$	$1/2 - 3/2$	1238.8
		$1/2 - 1/2$	1242.8
N V	$3\mathrm{p}\,^2\mathrm{P^o}$ - $3\mathrm{s}\,^2\mathrm{S}$	$3/2 - 1/2$	4603.8
		$1/2 - 1/2$	4619.9
N V	$7\mathrm{f}\,^2\mathrm{F^o}$ - $6\mathrm{d}\,^2\mathrm{D}$		4933.9
	7ghi - 6fgh		4943.1, 4943.9, 4945.2

3.3.5 Neon

For the VLTP scenario, calculations by Herwig et al. (1999) predict a neon mass fraction of 3.5 % on the the surface as a result of the mixing during the convective hydrogen

burning. A similar amount of 2.1 % results from the model calculations of Althaus et al. (2005). Neon is already produced in the helium burning shell of AGB stars by the reaction chain (Iben & Tutukov 1985) $^{14}\mathrm{N}(\alpha,\gamma)^{18}\mathrm{F}(\mathrm{e}^{+}\nu)^{18}\mathrm{O}(\alpha,\gamma)^{22}\mathrm{Ne}$. In the He burning shell it reaches an amount of 2 %. On the basis of Ne III lines, Leuenhagen & Hamann (1998) derived neon abundances in the range of $2-4$ % for some [WCL] stars. In PG 1159 stars, Werner & Rauch (1994) detected neon by identification of spectral lines from Ne VII. For [WCE] stars, the first detection of neon lines was reported by Herald & Bianchi (2004) for NGC 2371/2. They found a strong Ne VII resonance line (973.33 Å) in the FUSE spectrum. Unfortunately this line is almost saturated already at solar neon abundance, and other lines like the Ne VI multiplet around 2225 Å or the Ne VII absorption line at 3644.3 Å are needed for the determination of neon abundances.

Werner et al. (2007) reported the detection of a Ne VIII line at 6068 Å for a PG 1159 star. This line can be also seen in some of our [WCE] program stars (see Sect. 3.4.3). As exact calculations of the atomic structure of Ne VIII from the Iron project are incomplete, Werner et al. (2007) obtained parts of the atomic data for Ne VIII via extrapolation. Hence, they recommend not to use the Ne VIII lines for determination of abundances.

Table 3.3: Neon lines, wavelengths and identifications. 1: Ralchenko & NIST ASD Team (2008) and references therein, 2: Herald & Bianchi (2004), 3: Werner et al. (2004), 4: Werner et al. (2007), atomic data are taken from `http://astro.uni-tuebingen.de/~rauch/TMAD/NE/NE_VIII_LF`

Ion	transition	$J_\mathrm{u}-J_\mathrm{l}$	wavelength [Å]	Reference
Ne VI	3d ^{2}D - 3p ^{2}P$^\mathrm{o}$	$5/2-3/2$	2233.9	1, 2
		$3/2-3/2$	2237.7	1, 2
		$3/2-1/2$	2221.7	1, 2
Ne VII	2p^2 ^{1}D - 2s2p ^{1}P$^\mathrm{o}$	$2-1$	973.3	1, 2
Ne VII	2s3p ^{1}P$^\mathrm{o}$ - 2s3s ^{1}S	$1-0$	3644.3	1
Ne VII	3d ^{3}D - 3p ^{3}P$^\mathrm{o}$	$3-2$	3894.0	3
		$2-2$	3905.1	3
		$2-1$	3873.2	3
		$1-2$	3912.3	3
		$1-1$	3866.8	3
		$1-0$	3853.3	3
Ne VII	11 - 9		4555	1
Ne VII	9kl-8ik		5665	1, 4
Ne VIII	9l-8k		4340.77	4
Ne VIII	10m - 9l		6068.63	4

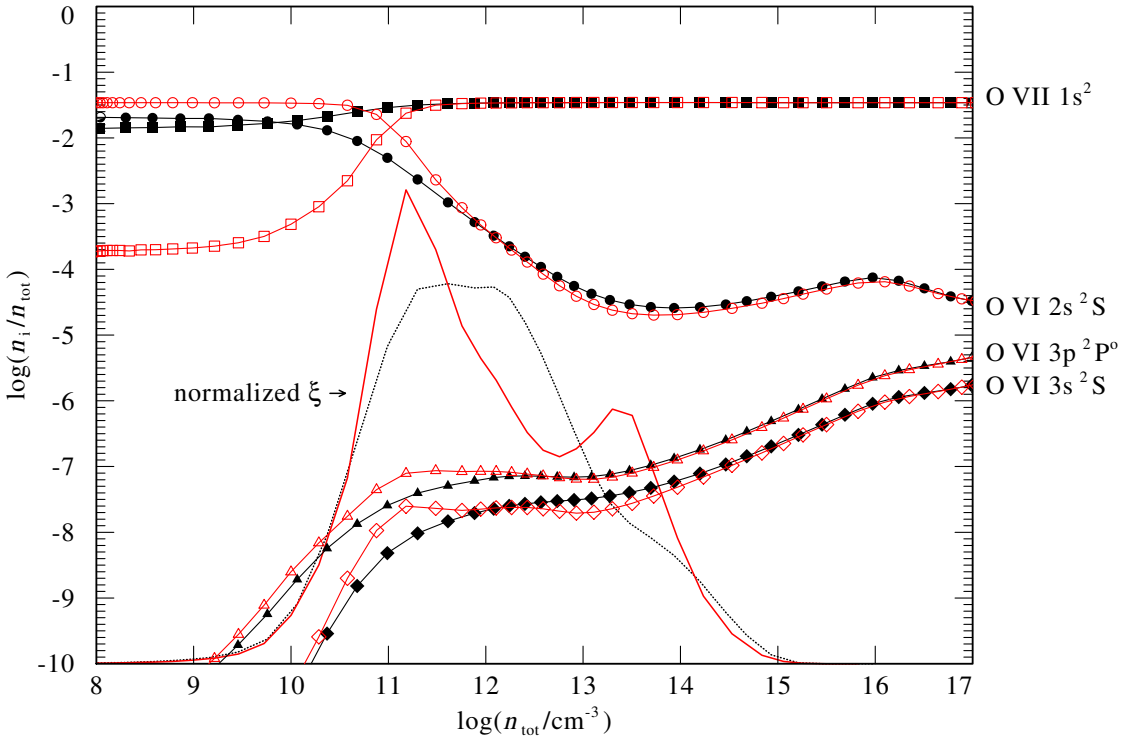

Figure 3.9: Population numbers of O VI and O VII for a grid model with $T_* = 158\,\mathrm{kK}$ and $R_\mathrm{t} = 5.0\,R_\odot$ plotted over density as indicator of radial location. The outer boundary is left, the inner boundary right. Shown is the ionization stratification for two models with same parameters but with different stages of completion of the iron group elements: grid model with ionization stages up to Fe X (black lines, filled symbols) and model with ionization stages Fe XI (red lines, open symbols), thus with complete Fe X. The model with Fe XI shows enhanced recombination to O VI in the outer region compared to the model with Fe X. The increase in the occupation numbers of the O VI $3\mathrm{p}\,^2\mathrm{P}^\mathrm{o}$ level results in an increase of the equivalent width of the 3811/34 Å line by 90 %. Additionally the (normalized) ξ of the spectral line is plotted for both models (black dotted line: Fe X, red solid line: Fe XI), indicating that the line forming regions are slightly different for both models. Due to the normalization of ξ the areas below both curves are almost equal and do not indicate the absolute equivalent width.

3.4 New line-blanketed analyses of individual [WCE] stars

Our sample of [WCE] stars contains those, which were already analyzed with unblanketed models by Koesterke & Hamann (1997b) and Koesterke (2001) and for which optical spectral are available. Additionally, we have analyzed NGC 5315, but excluded NGC 2452 from our sample due to insufficient S/N of the optical spectrum. For the following objects of our sample we obtained new optical spectra with higher spectral resolution and better S/N ratio by M. Peña in 2006: NGC 2867, PB 6, NGC 5189, and Hen 2-55. See Sect. 5.1.2 for details.

FUSE spectra with sufficient quality are available for NGC 2867, PB 6, NGC 5189, NGC 6905, NGC 5315, and are included in our SED fits. In most cases the FUSE fluxes cannot be reproduced consistently with the IUE and optical fluxes.

Johnson photometry is taken from NOMAD (Zacharias et al. 2004), 2MASS JHK colors from Skrutskie et al. (2006).

Table 3.4: Archive identifiers of the IUE observations used for the analyses.

Object	IUE SHORT	IUE LONG
NGC 2867	SWP05215LL	LWR04510LL
PB 6	SWP36238LL	LWP17426LL
NGC 5189	SWP25364LL	LWR07171LL
NGC 6905	SWP13405LL	LWR10067LL
NGC 7026	SWP51698LL	LWP28800LL
Hen 2-55	SWP54033LL	-
Sand 3	SWP06773LL	lwr05737-mx
		+ lwr05765-mx
IC 1747	SWP35634LL	LWP15112LL
NGC 1501	SWP28953LL	LWP08948LL
NGC 6369	-	LWP15973LL
NGC 5315	SWP36245LL	LWP15491LL

3.4.1 NGC 2867

The whole spectral fit for NGC 2867 is plotted in Fig. 3.10. The upper panel shows the spectral energy distribution (SED) as observed, i.e. flux calibrated spectra (blue lines) and photometric values (blue blocks), together with the model SED (red line) in a double logarithmic representation. The units on the abscissa are log Å.

The quality of the IUE and the optical spectra of NGC 2867 suffers from strong nebular emission. Even the nebular continuum emission is so intense, that it distorts the observed stellar continuum flux (cf. Fig. 3.10, upper panel). Especially the IUE satellite, with its large aperture of $10'' \times 20''$ collects a lot of the nebular continuum emission.

In the second panel, the IUE spectrum (blue line), normalized to the model continuum is shown together with the model spectrum (red line). If normalization of the IUE observation cannot achieved with a single fit to the SED, the alternative procedure is described in the corresponding caption.

In the lower panels, the observed optical spectrum (blue line) is shown together with the model spectrum (red line). Flux calibrated spectra are usually normalized to the model continuum, otherwise the normalization is done by eye.

For the normalized spectra, line identifications are given.

The determination of nitrogen is hampered by the strong nebular emission, as the observed spectrum close to the N v 4944 Å line is contaminated by the [O iii] 4959 Å nebular line (cf. Fig. 3.11). The feature close to the position of the usual N v 7-6 line seems to be rather an artifact of the data reduction than the N v 7-6 line. Moreover, in absence of a strong N v 2p-2s UV line, we give an upper limit for the nitrogen abundance based on the weak N v 3p-3s line of 0.5 % by mass.

A similar artifact from data reduction can be seen in the red wing of the Hβ/He ii 8-4 line, which one could otherwise confuse with a stellar Hβ line.

By the inclusion of higher ionization stages of Fe and the high temperature of 158 kK for our model, we obtain an extremely strong O vi 3811/34 Å line. The strength of the synthetic line is even larger than in the observation. However, the other O vi lines are matched well, using this temperature and with an abundance of 10 % by mass.

Both lines of the diagnostic line pair He ii 5412 and C iv 5470 have almost equal strength in the observation. As the nebular He ii is narrower than the stellar line, they can be easily distinguished. With our He:C abundance of 60:30 the observed line strengths, in particular the equal peak heights, are sufficiently reproduced. Note the small absorption or P Cygni feature of the synthetic He ii line. This can also be seen for other He ii lines of the model, e.g. for He ii 8-4, as well as for other models, e.g. in the model for Hen 2-55. This feature is not visible in the observation and may be indicative for a different velocity field than our standard $\beta = 1$-law.

3.4.2 PB 6

The N/O ratio in the nebula was found by García-Rojas et al. (2009) to be 1.5 by number (see Table 3.5). From comparison with stellar evolutionary tracks, Kaler & Jacoby (1989)

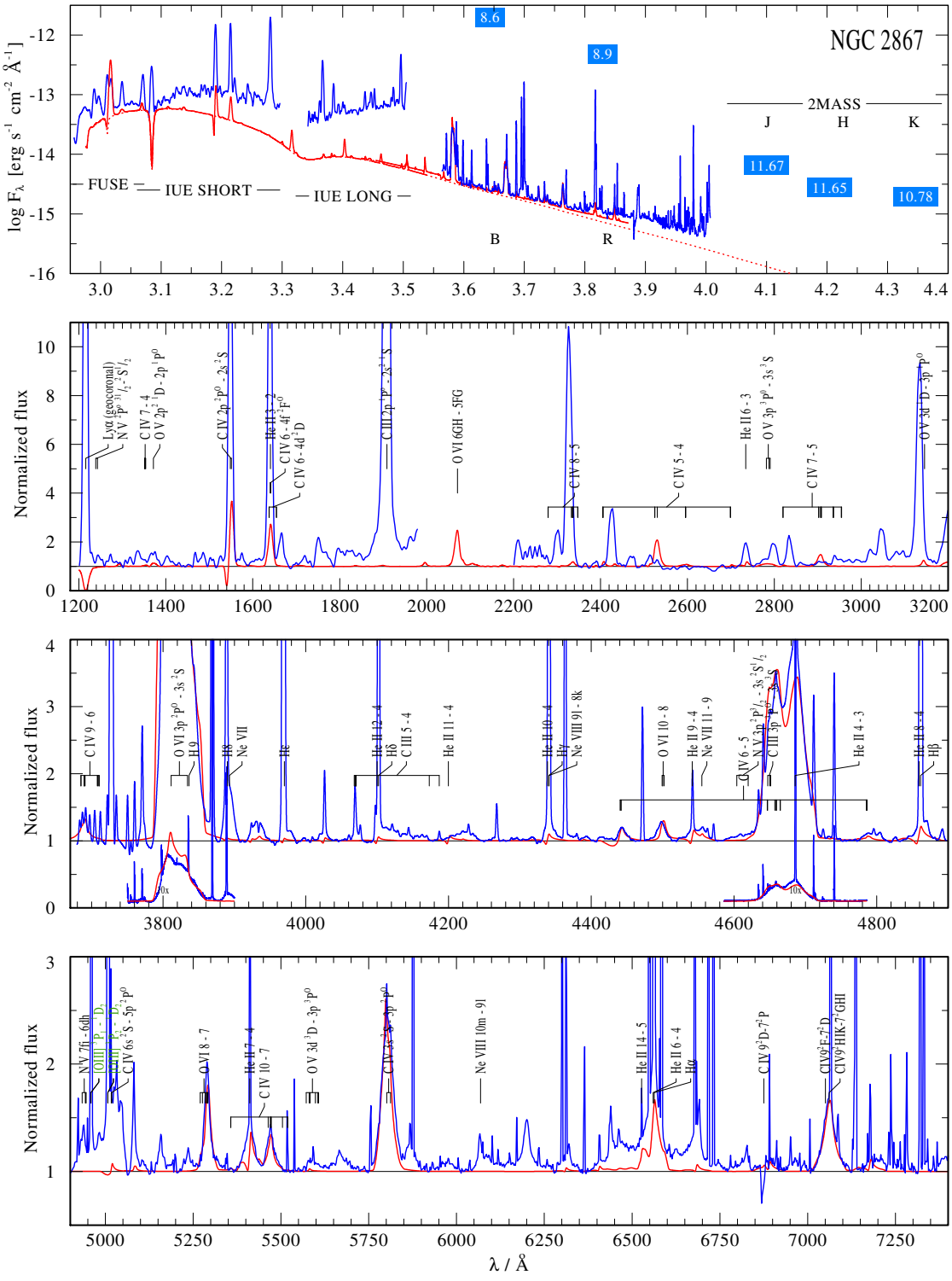

Figure 3.10: NGC 2867: observation (blue line) vs. PoWR model (red). Upper panel: stellar model continuum (red dotted) and stellar plus nebular continuum (red solid). Rectification of the IUE and optical spectra is done by eye.

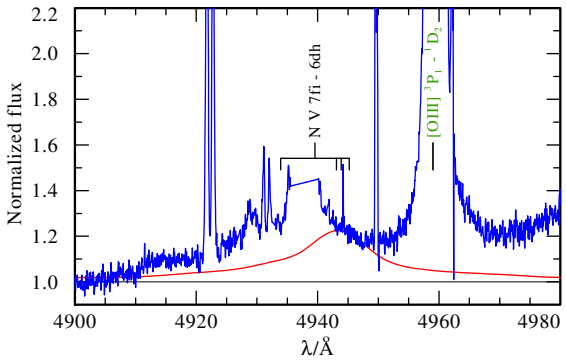

Figure 3.11: Detail of the optical spectrum of NGC 2867, showing the N V 7-6 line. Due to the strong emission of the neighboring nebular line, the observed "N V line" (blue line) appears to be more like an artifact of the data reduction than a real spectral line. The "line" has a flat top profile and is shifted by ca. 10 Å against the N V line from the PoWR model (red line).

have deduced that N/O> 0.8 indicates that hot bottom burning (HBB) has been effective in the former AGB-star. This implies that the core mass is larger than $M_{\rm core} > 0.8 M_{\odot}$, therefore our luminosity distance would be too small.

Table 3.5: Nebula abundances for PB 6 (number ratios), from García-Rojas et al. (2009)

He / H	O / H	C / O	N / O	Ne / O
0.19	3.8×10^{-4}	0.95	1.5	0.35

Our best fit for this star is shown in Fig. 3.12. To fit the strong N V 7-6 line at 4944 Å we include 1.5 % nitrogen by mass in our model. Like this, the other N V lines at 4604/20 Å and the N V resonance line in the UV are also well fitted.

The strength of the O VI 3811/34 Å line can be reproduced by the model.

3.4.3 NGC 5189

Our best spectral fit for the central star NGC 5189 is shown in Fig. 3.14. The spectrum shows strong spectral lines of neon. The PoWR model in Fig. 3.14 accounts for neon with an abundance of 3 % by mass.

With this neon abundance, the synthetic absorption profile of the Ne VII $3p\,^1P^o$-$3s\,^1S$ lines is already much deeper than in the observation, while the Ne VII $3d\,^3D$-$3p\,^3Po$ emission line as well as the Ne VI 3d-3p line in the UV, are still weaker than observed.

For the Ne VI 3d-3p line the discrepancy can also be an effect of a inaccurate normalization of the observed IUE flux. Moreover, this neon line is close to the absorption

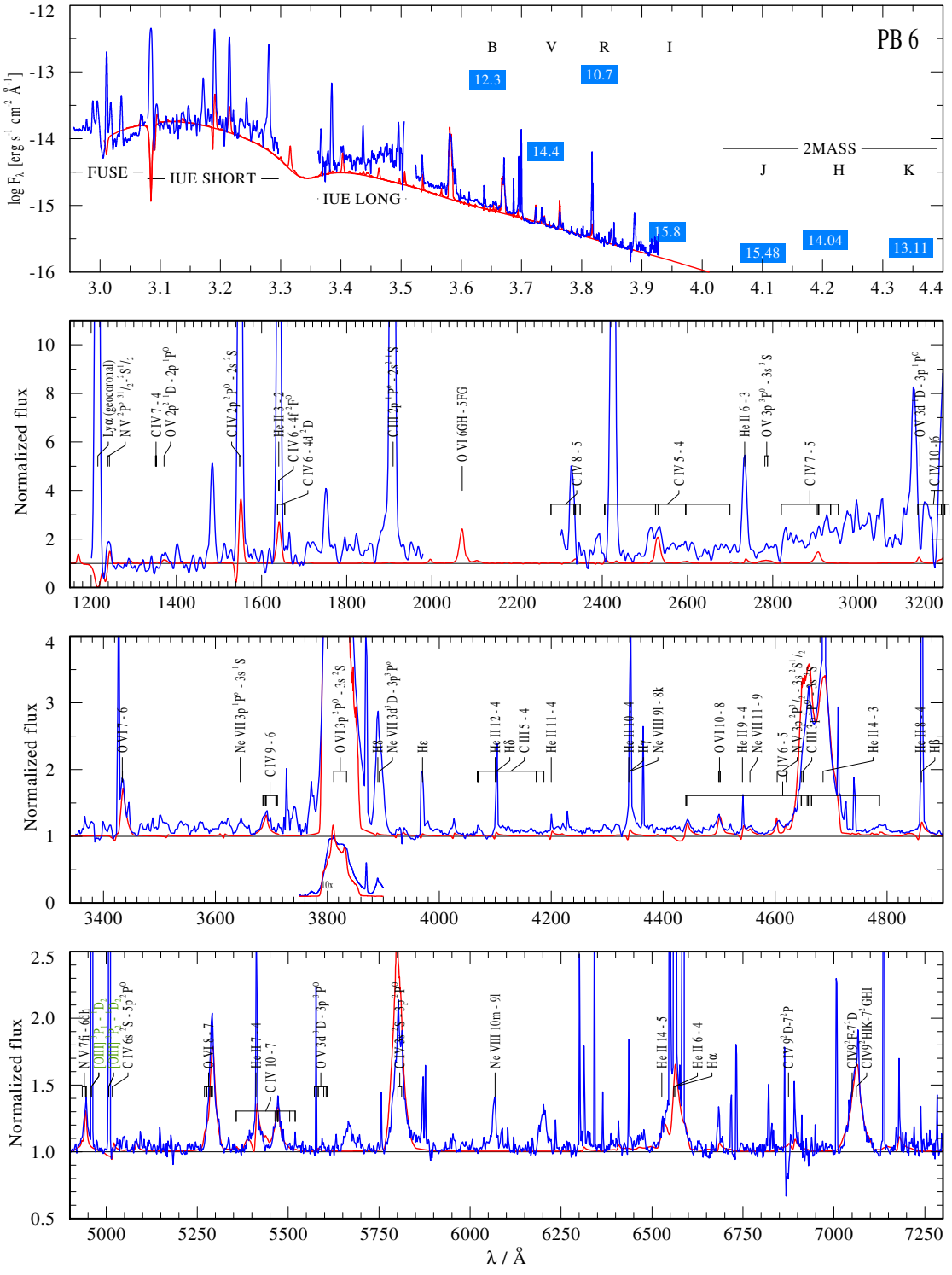

Figure 3.12: PB 6: observation (blue line) vs. PoWR model (red).

maximum of the interstellar medium, which makes it even more difficult to obtain a good estimate for the stellar continuum at this wavelength.

Note the deep absorption lines of the synthetic spectrum in the IUE range, which cannot be clearly seen in the observation, although the observation is perhaps too noisy for a clear evidence.

We also calculated a model including Ne VIII from Werner et al. (2007), but show only the interesting region of the optical spectrum in Fig. 3.13. Although the Ne VIII 6068.6 Å line can be reproduced qualitatively, the synthetic line is weaker than in the observation.

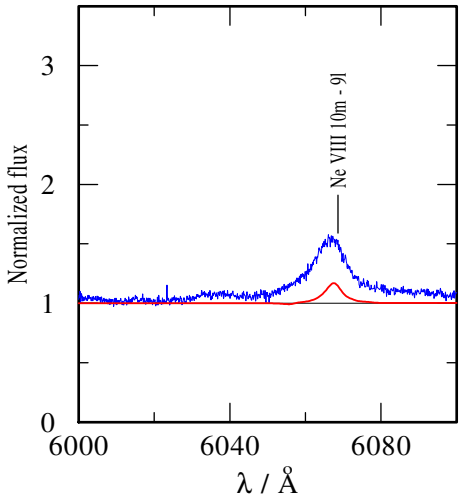

Figure 3.13: Ne VIII 6068.6 Å in the spectrum of NGC 5189: observation (blue line) vs. PoWR model (red line) including 1 % of neon (by mass).

The diagnostic line pair He II 5412 and C IV 5470 is nearly perfectly fitted. In contrast to the model for e.g. NGC 2867, the He II lines of this model do not show P Cygni-like features, although both models have almost the same parameters. The model for NGC 5189 accounts for neon. Hence, the absence of the P Cygni-profiles of the He II lines may be an effect of the line-blanketing by neon lines.

According to the good agreement between the observed and synthetic He II 7-4 *and* He II 8-4 lines, we infer an upper limit for the hydrogen mass fraction or 5 %. With a higher hydrogen abundance, the He II 8-4/Hβ line blend would be stronger than the pure He II 7-4 line (cf. Sect. 5.1.3).

3.4.4 NGC 6905

Optical spectra were taken at Calar Alto Observatory in 1993 for the ranges from 3340 Å to 4810 Å, 4590 – 5979 Å and 5820 – 7200 Å. The spectral resolution is roughly 1.5 Å and the S/N ratio ca. 20. All three spectra are already normalized by eye.

Our best fit for this star is shown in Fig. 3.15

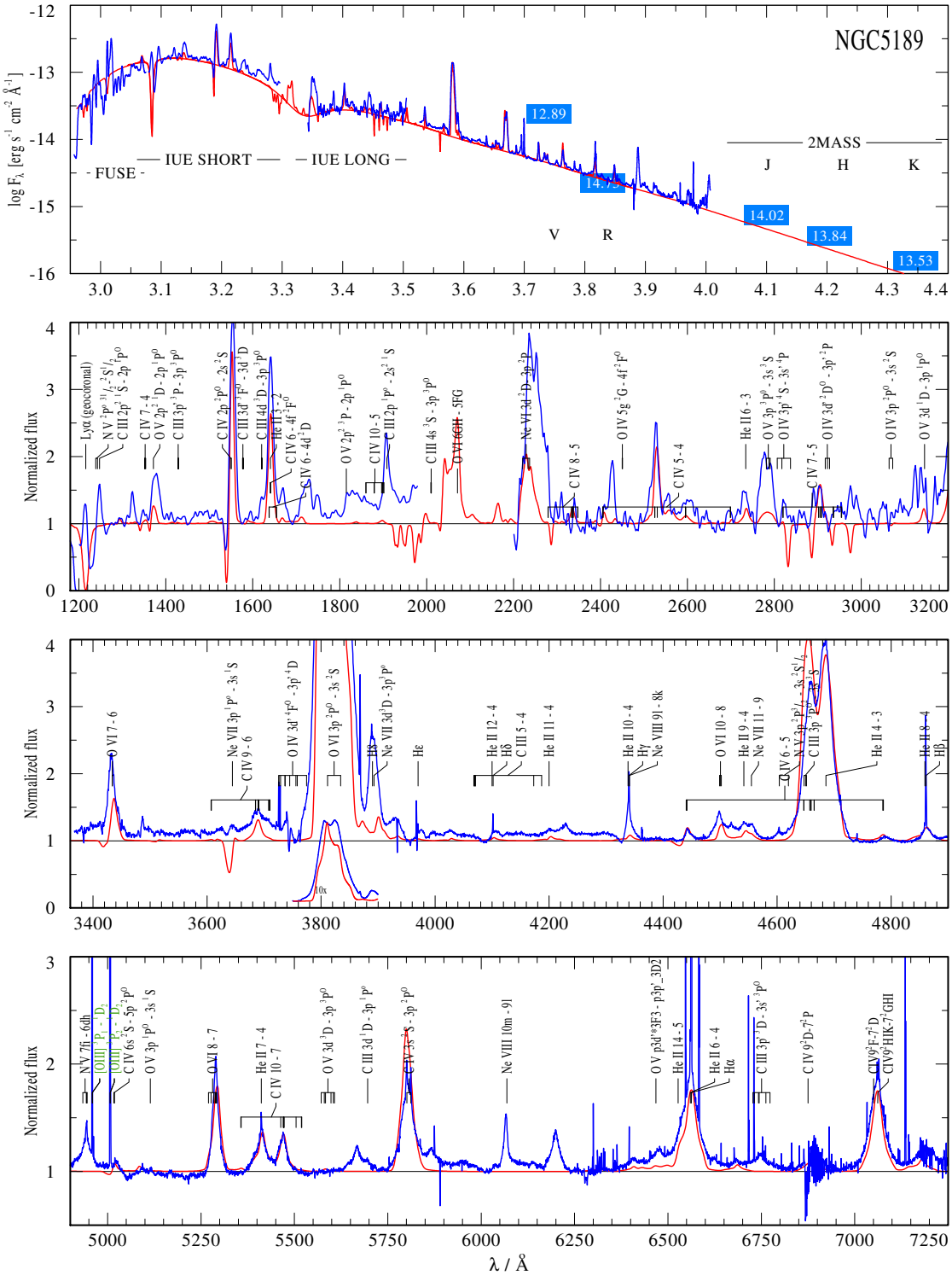

Figure 3.14: NGC 5189: observation (blue line) vs. PoWR model (red), which includes Ne V - VII, but not Ne VIII and N.

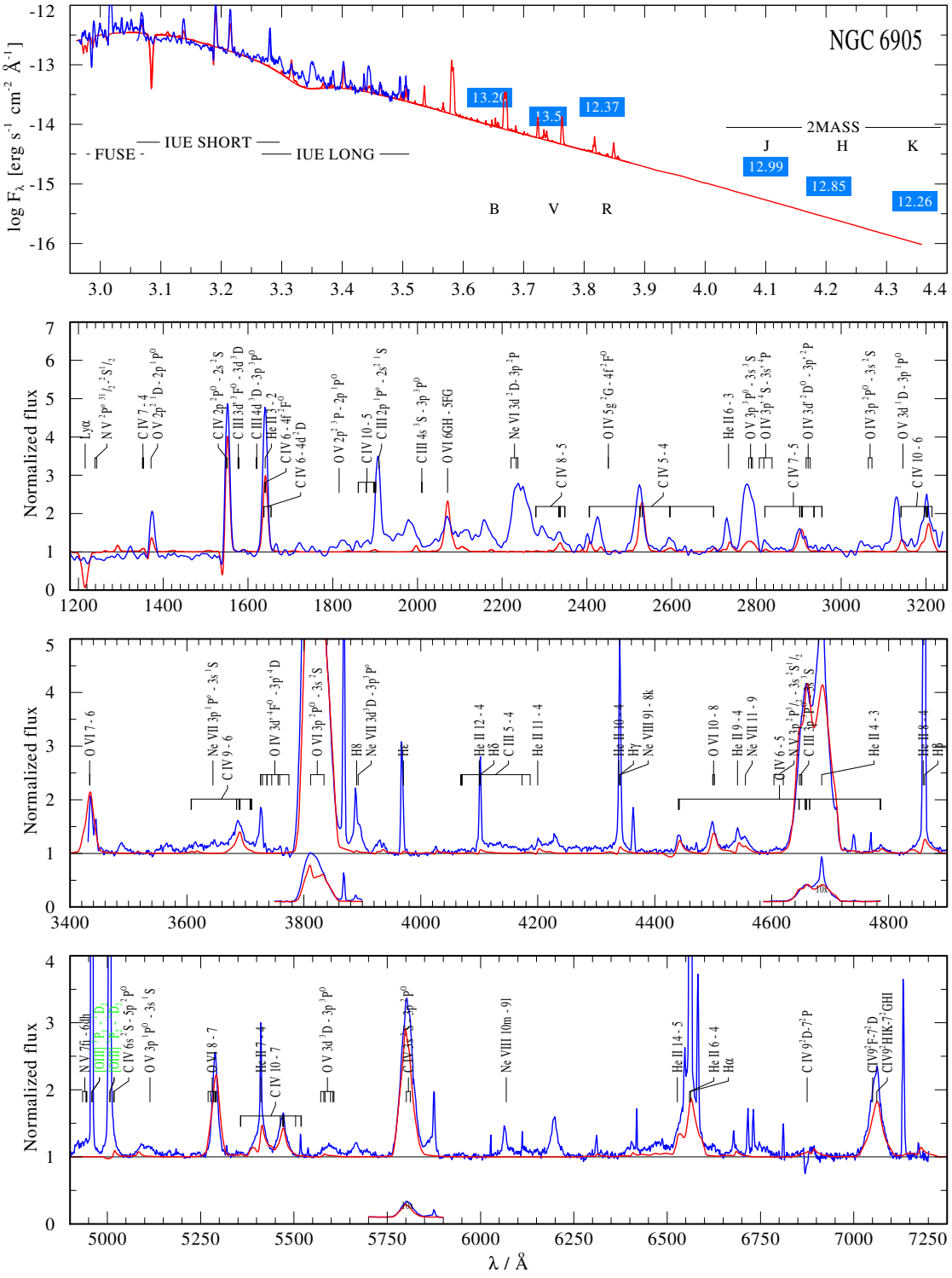

Figure 3.15: NGC 6905: observation (blue line) vs. PoWR model (red).

We obtain a sufficiently good fit to the C IV, He II, and O VI lines with $T_* = 150$ kK and $R_t = 4.5$. The O V lines, e.g. the O V $3d^3D$-$3p^3P^o$ line, are a bit too weak. However, by a lower temperature of $T_* = 140$ kK, which would reproduce the O V lines much better, the O VI 3811/34 Å line would become too weak.

Interestingly, when using the parameters by Marcolino et al. (2007), with helium abundance of only 50 %, the carbon lines are still reproduced nicely - due to the higher R_t, but then all helium lines become too weak.

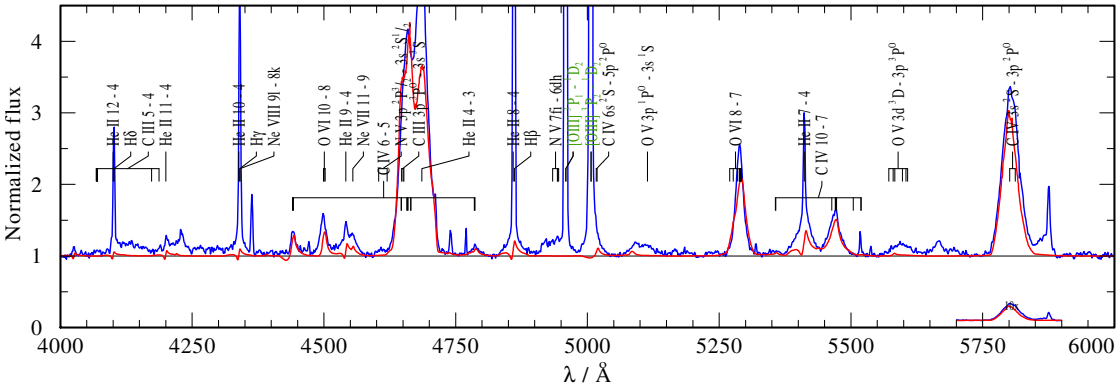

Figure 3.16: NGC 6905: Detail of optical spectrum with C IV and He II lines, observation vs. PoWR model with parameters from Marcolino et al. (2007): $T_* = 149.6$ kK, $R_t = 10.5\,R_\odot$, He:C:O=40:49:10. With this helium abundance, which is lower than the value we derived, all He II lines are weaker than in the observation, in particular the He II 7-4 line of the diagnostic line pair.

3.4.5 NGC 7026

Our optical spectrum for NGC 7026 is not flux calibrated and obtained at Calar Alto in 1993. The S/N ratio, especially above 5000 Å, is very low. We try to get a fit to the most prominent lines, O VI 3811/34 Å and the blend of helium and carbon lines at 4680 Å, and try to reproduce the O V $3d^3D$-$3p^3P^o$ line at the same time. Our compromise shown in Fig. 3.17 fit is achieved with a T_* of 130 kK and an R_t of $6.3\,R_\odot$. Regarding the low S/N ratio, the diagnostic line pair is sufficiently reproduced with our usual abundances. Our model includes nitrogen with solar abundance. For a higher abundance, the N V resonance line in the UV would be clearly detectable.

3.4.6 Hen 2-55

To fit the observed SED in the optical and IUE range consistently to the model SED, it is necessary to choose $R_V = 2$, which is a rather unusual value for the reddening law from Cardelli et al. (1989). The lowest value of R_V, found by Cardelli et al. (1989) is 2.85. The SED fit shown in Fig. 3.18 uses $R_V = 2$, $E_{B-V} = 0.35$, and $DM = 13.87$, implying a

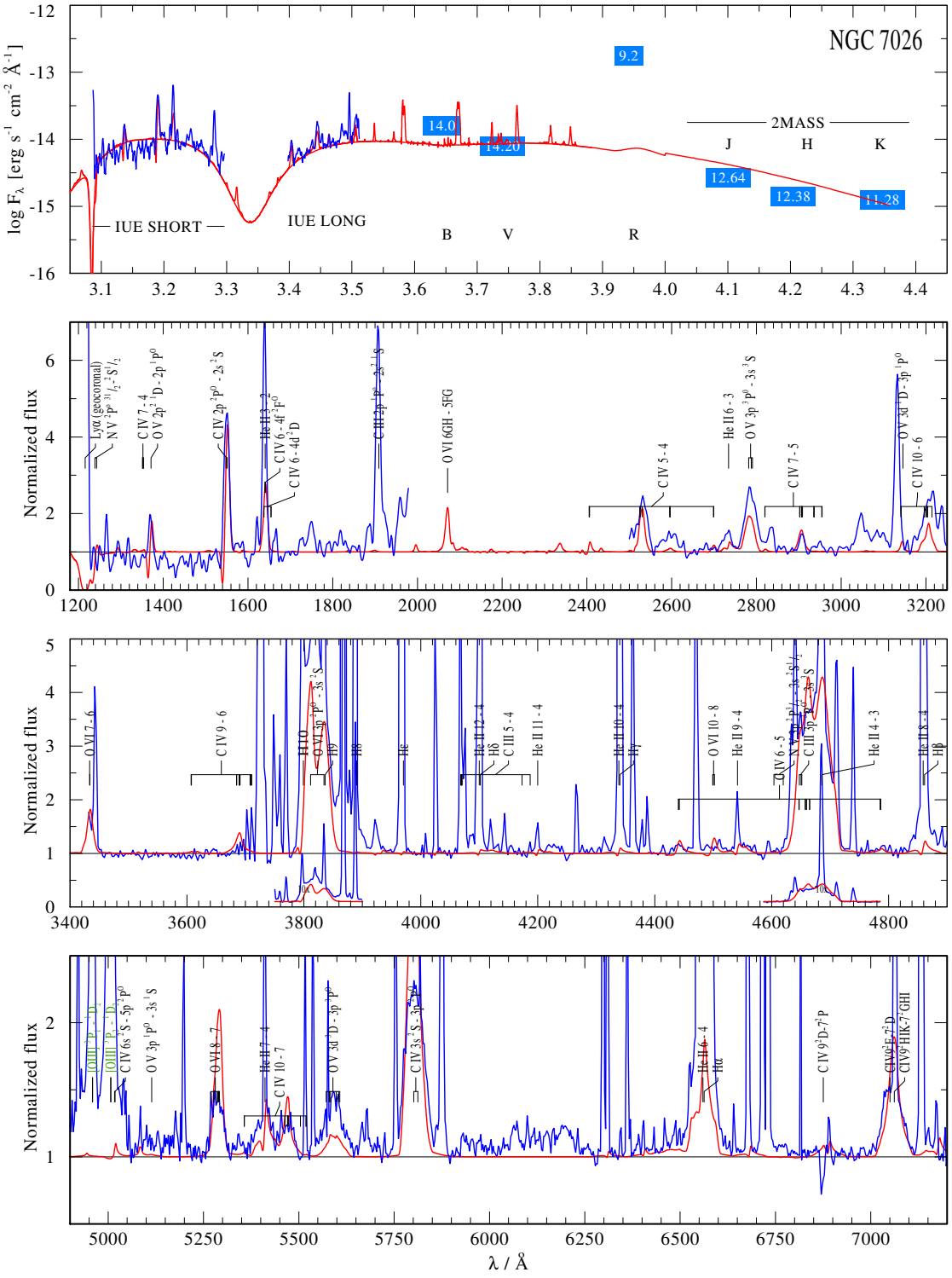

Figure 3.17: NGC 7026: observation (blue line) vs. PoWR model (red).

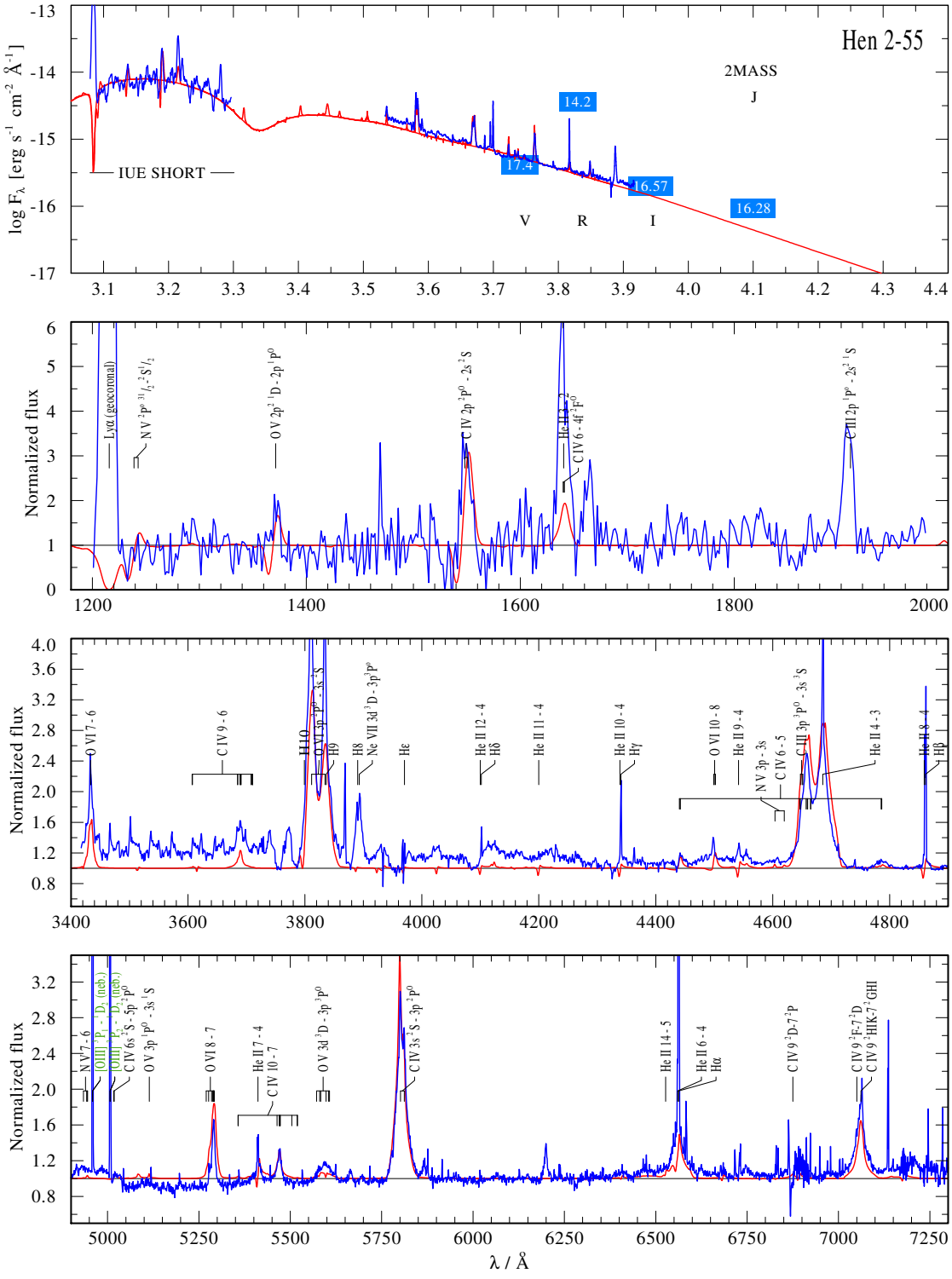

Figure 3.18: Hen 2-55: observation (blue line) vs. PoWR model (red).

distance of 5.9 kpc. By neglecting the IUE observation, a better fit of the model SED to the optical observation can be achieved by a more common value for $R_V = 3.1$, together with $E_{B-V} = 0.3$, and $DM = 13.65$, which corresponds to a distance of 5.4 kpc.

Our temperature estimate of 126 kK is close to the temperature determined by Koesterke (2001).

The feature at 3893 Å, where Werner et al. (2004) found a Ne VII line, appears like a strong stellar line. Although for some hot stars, e.g. NGC 5189, our models can reproduce the Ne VII line in emission, it is rather unlikely that this is also the case for Hen 2-55, as it has a much lower temperature. Moreover, in the spectra of other [WCE] that clearly show Ne VII lines, there is always the the Ne VIII 6069 Å line present as well, e.g. for NGC 5189 and PB 6. For Hen 2-55, this Ne VIII line is completely missing, although the putative Ne VII line is almost as strong as for NGC 5189. Hence, we suggest that this feature generally does not arise from Ne VII, although for the hotter [WCE] stars, it may be blended with the Ne VII line.

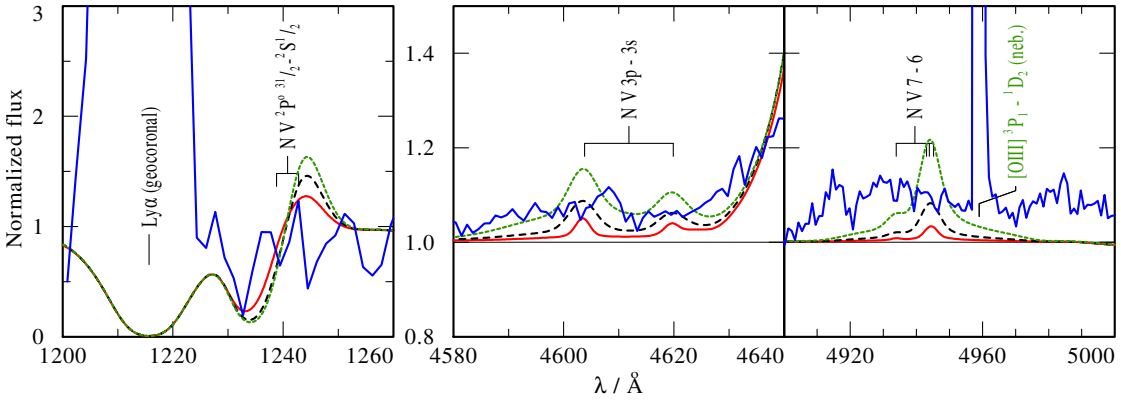

Figure 3.19: Hen 2-55: Spectral lines from N V, observation vs. PoWR models with $\beta_N = 0.1\,\%$ (red solid line), with 0.3 % (black dashed), and 1 % (green dotted) by mass fraction. In both observations, IUE and optical, the nitrogen lines can be hardly detected. Therefore only an upper limit of 0.3 % nitrogen can be given.

3.4.7 [S71d]3 – Sanduleak 3

So far, a planetary nebula has not been detected around this object, although it is listed as PN G341.5+12.1 in the ESO catalogue of Galactic planetary nebulæ (Acker et al. 1992).

Sanduleak 3 was first identified by Sanduleak (1971) and classified as a (massive) WC star on the basis of its spectrum, which shows a strong O VI 3811/34 Å line. It was listed as WR 72 in "The Sixth Catalogue of Galactic Wolf-Rayet stars" as type WC4pec. (van der Hucht et al. 1981). It is often referred to as Sand 3, which should not be confused with WD 1201+296, which is also called Sand 3. Therefore the unambiguous designation

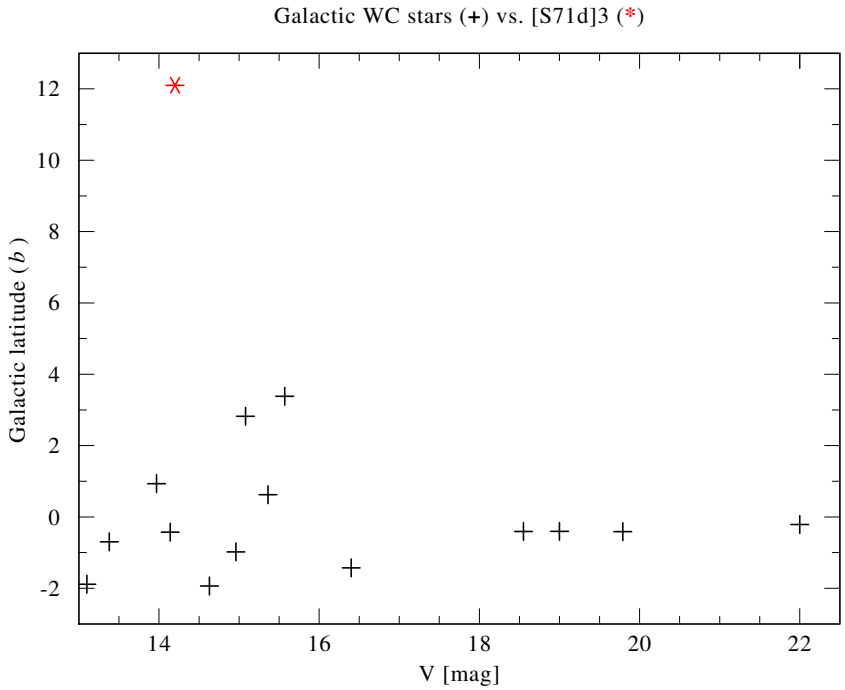

Figure 3.20: Galactic latitude (b) plotted over Johnson V (data from SIMBAD). If [S71d]3 were a massive WC star, its luminosity would be comparable to the luminosities of other Galactic WC stars and the apparent magnitude in the V band would be an indicator of the distance d (neglecting reddening). In this case, its absolute height above the fundamental plane of the Galaxy given by $d \sin b$ would be much higher than for other WC stars.

[S71d]3 is used here.

Barlow & Hummer (1982) excluded [S71d]3 from the WC sequence for the following reasons, from which we repeat the most important ones:

If [S71d]3 were a massive Pop I WC star, it would have a luminosity of at least $\log(L/L_\odot) = 5.3$, shifting its distance from 1.0 (for a typical CSPN luminosity of $\log(L/L_\odot) = 3.7$) to 6.3 kpc (our values). With a Galactic latitude of 12.1° this corresponds to a height of 1.4 kpc above the fundamental plane of the Galaxy. This is much more than the scale height of the thin disk, and therefore an unlikely location for a massive star (cf. Fig. 3.20).

The UV-spectra look very similar to the UV-spectra of the CSPN NGC 5189 and NGC 6905 (see figure 3.21). The presence of a strong N V resonance line in the spectra of [S71d]3 and NGC 5189 indicates supersolar abundance of nitrogen, which is not expected for evolved WC stars.

Therefore, WR 72 has been removed from the catalogue of galactic Wolf-Rayet stars (van der Hucht 2001).

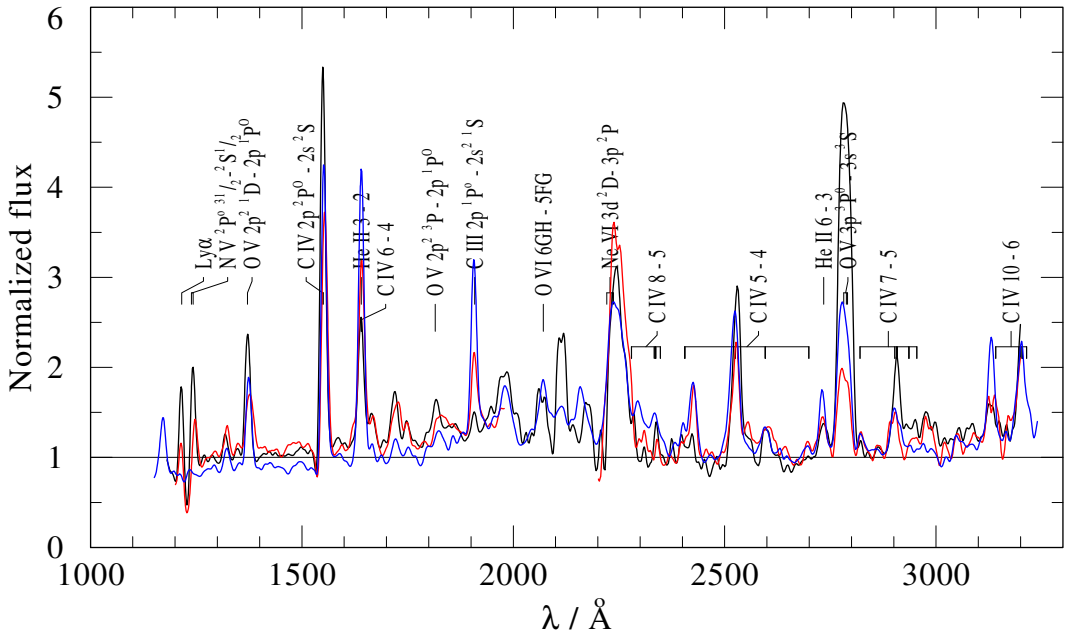

Figure 3.21: Continuum normalized IUE spectra of [S71d]3 (black line) and the [WC] central stars NGC 5189 (red) and NGC 6905 (blue). The spectra show the same features (e.g. the probable Ne VI emission line), but in different strength.

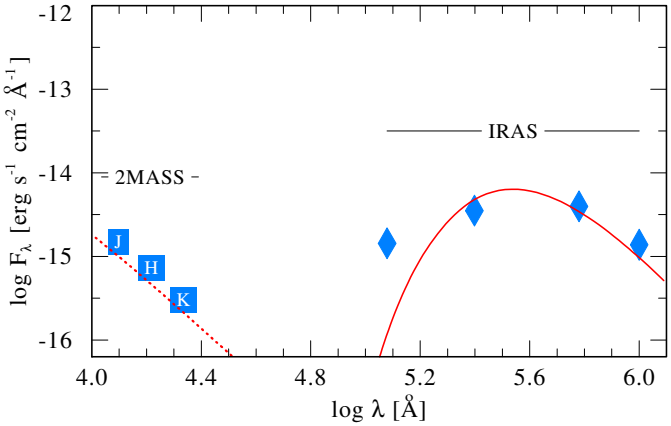

Figure 3.22: SED of [S71d]3 in the infrared range. Photometric observations (blue blocks) for JHK are from 2MASS and $12, 25, 60, 100\,\mu$m from IRAS (IPAC V2.0 1986, blue diamonds). Also shown is the synthetic stellar continuum (red dotted) and a blackbody spectrum (red line) for $T = 85$ K, as reported by van der Hucht et al. (1985), indicating warm dust as a remnant of a former PN.

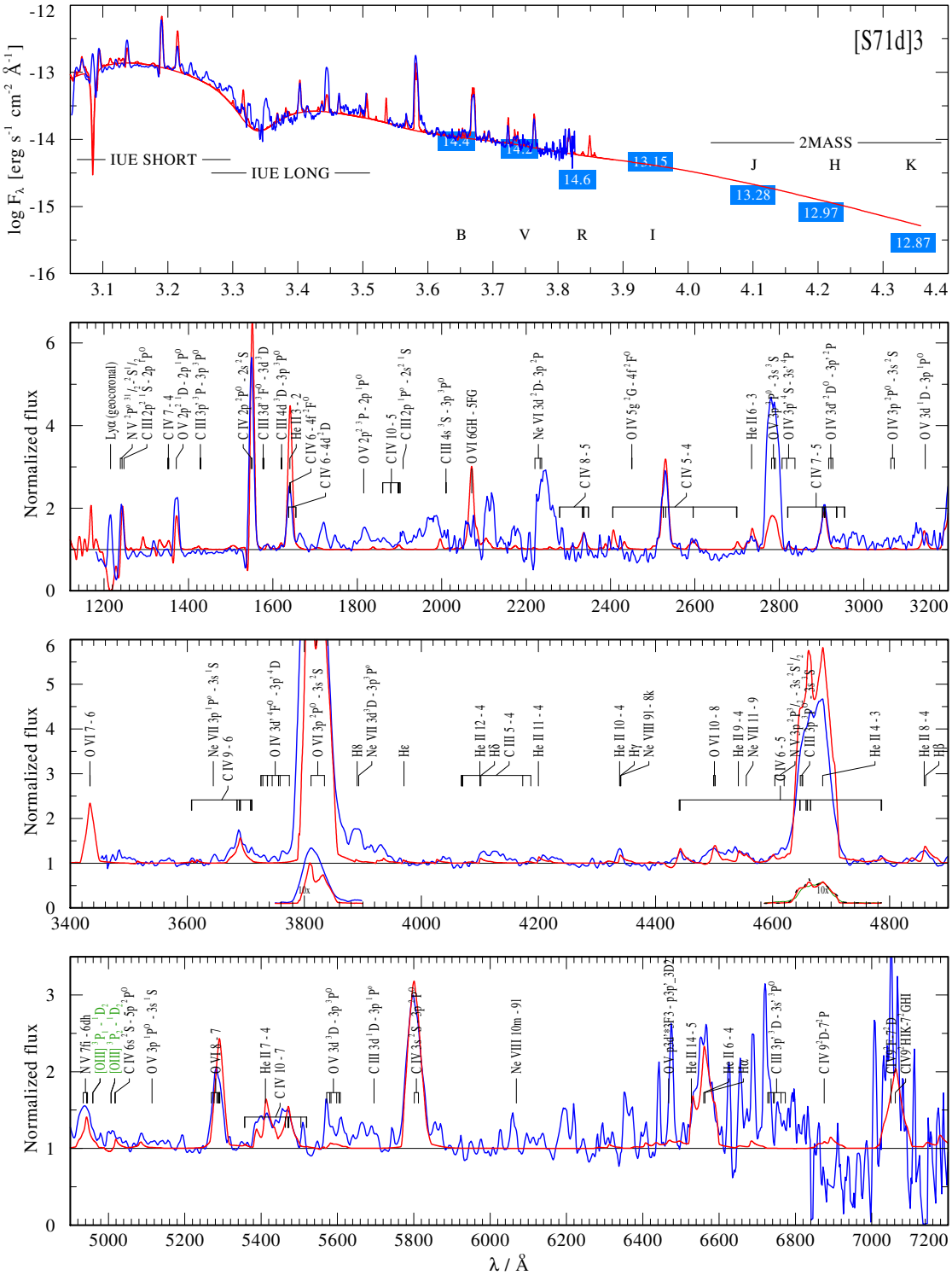

Figure 3.23: [S71d]3: observation (blue line) vs. PoWR model (red).

An IR excess was found by van der Hucht et al. (1985) from IRAS observations at the position of [S71d]3, which they attribute to "warm dust" of a temperature of 85 K (see Fig. 3.22). IR emission from warm dust is typical for PNe (see e.g. Pottasch 1984). However, this is not a strong argument, as the the other star in their sample, WR 124, showing a similar IR excess is a WR star (Hamann et al. 2006).

As mentioned in Sect. 3.2, the different scaling properties of the line emission and the e.s. wings provide a way to discriminate between [WR] CSPN and massive WR stars. In Fig. 3.24 is demonstrated that for a massive WC star a stronger e.s. wing is expected than observed. Due to the low S/N ratio of the observed spectrum, this is rather weak evidence for the true nature of [S71d]3.

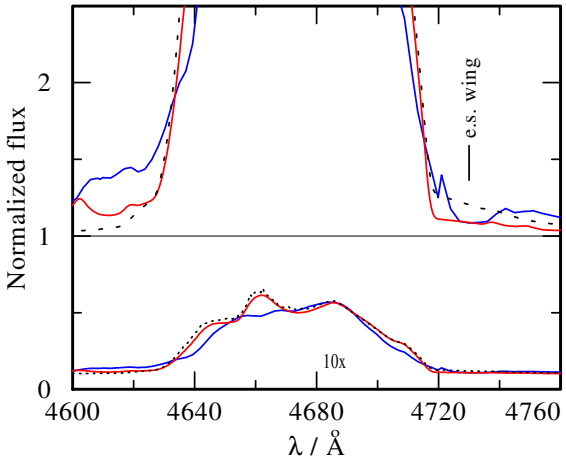

Figure 3.24: Detail of the optical spectrum of [S71d]3 (blue thin line) demonstrating different strengths of e.s. wings for a [WC] model (red solid line) and a WC model (black dashed) in spite of the same density contrast $D = 10$.

In the absence of a PN, the stellar spectrum is not contaminated by nebular emission lines. In principle, this allows for a more precise determination of the strength of the electron-scattering line wings. Unfortunately the quality of the spectra by Torres & Dodgen 1987 and 1988 is not sufficient to benefit from these special circumstances. Moreover, the part of the optical spectrum containing the diagnostic line pair He II/C IV is too noisy for reliable determination of the He:C abundance ratio. However, the observed spectra are roughly reproduced by our model.

Our best spectral fit is shown in Fig. 3.23.

From the strong N V lines we conclude that the nitrogen abundance must be as high as for PB 6 and NGC 5189, which show similar spectra.

3.4.8 IC 1747

The best spectral fit for IC 1747 is shown in Fig. 3.25.

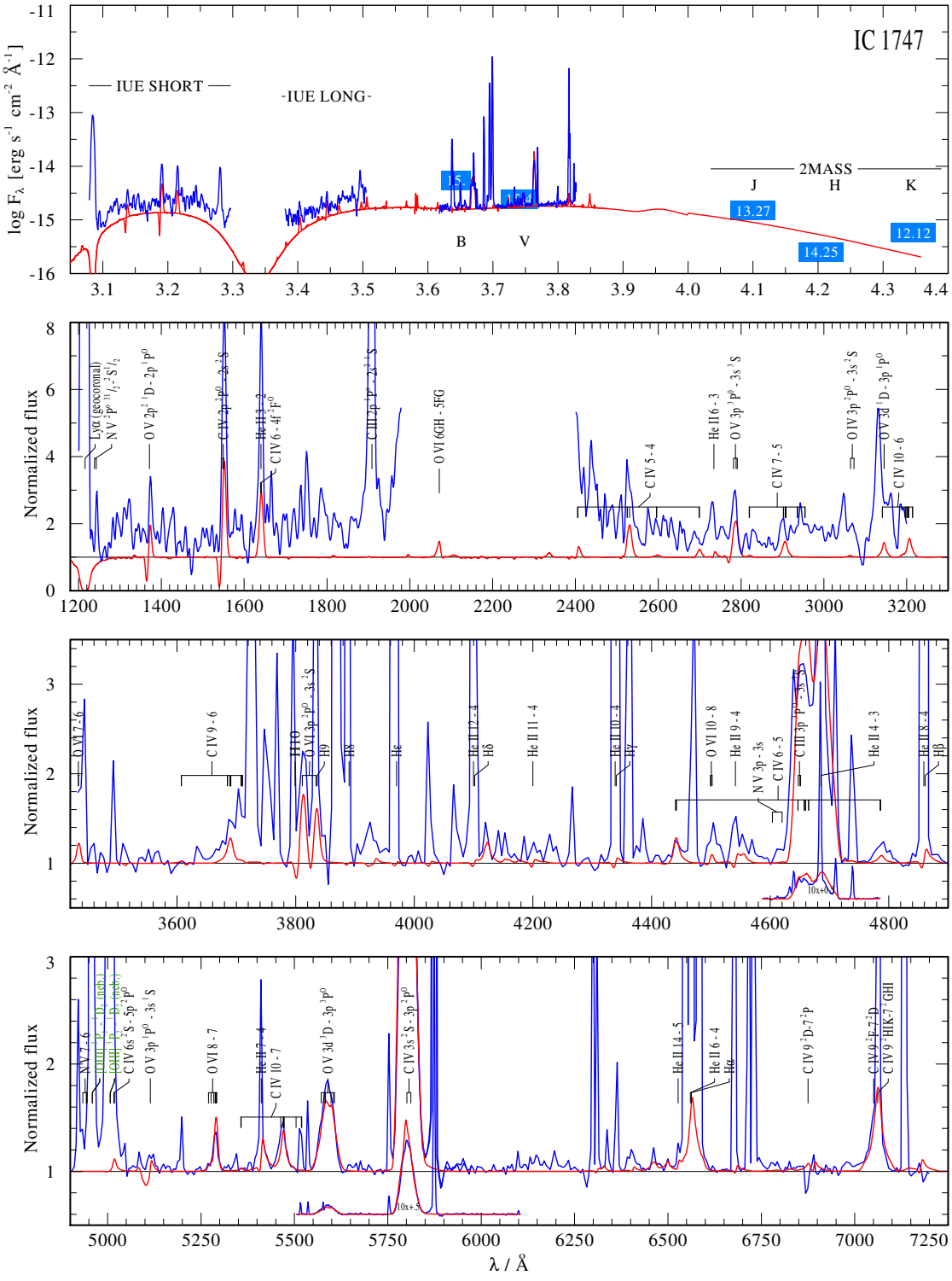

Figure 3.25: IC 1747: observation (blue line) vs. PoWR model (red).

Although the quality of the IUE and optical spectra for IC 1747 is low, the stellar lines can be sufficiently well distinguished from the strong nebular lines. We achieve a consistent fit of the O V and O VI lines together with the C VI 3p-3s line with a temperature of $T_* = 112\,\mathrm{kK}$ and an R_t of $10\,R_\odot$.

As the IUE spectrum is somehow noisy, we use for the SED fit the optical spectrum by M. Peña, obtained in July 1999 at the SPM observatory (Mexico) with a Boller and Chivens spectrograph (600 l/mm) at the 2.1m-telescope.

The N V 4934-4945 Å line is outshined by nebular emission. From the N V4604/20 Å line (cf. Fig. 3.26), we derive an upper limit for nitrogen abundance of 0.5 %, otherwise this line appears stronger than observed.

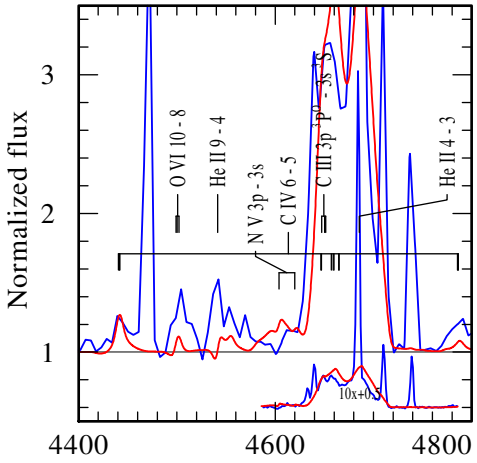

Figure 3.26: IC 1747 observation vs. model with 0.5 % nitrogen by mass.

3.4.9 NGC 1501

Bond et al. (1996) have observed this star in 1991 for two weeks seeking for pulsation periods. They find 10 independent pulsation periods, ranging from 1154 s up to 5235 s. They offer a model with a common period spacing of 22.3 s and a stellar rotation period of 1.17 days. From the period spacing they derive a astroseismological mass of $0.55 \pm 0.03\,M_\odot$.

Our best fit for this star is shown in Fig. 3.27.

With a T_* of 128 kK we can roughly reproduce the ratio between the line strength of the O VI and O V lines. With a lower temperature the O V become stronger, but on cost of the O VI lines. The C VI 3p-3s line is much stronger in the observation than in the model. As the line strength of this line reacts very sensitive to a change of R_t, T_*, the discrepancy may be overcome by a small change of the parameters.

The observed N V lines can be fitted with an abundance of 0.5 %.

For the SED fit, we rely on the optical spectrum by M. Peña, obtained in July 1999 at the SPM observatory (Mexico) with a Boller and Chivens spectrograph (600 l/mm) at

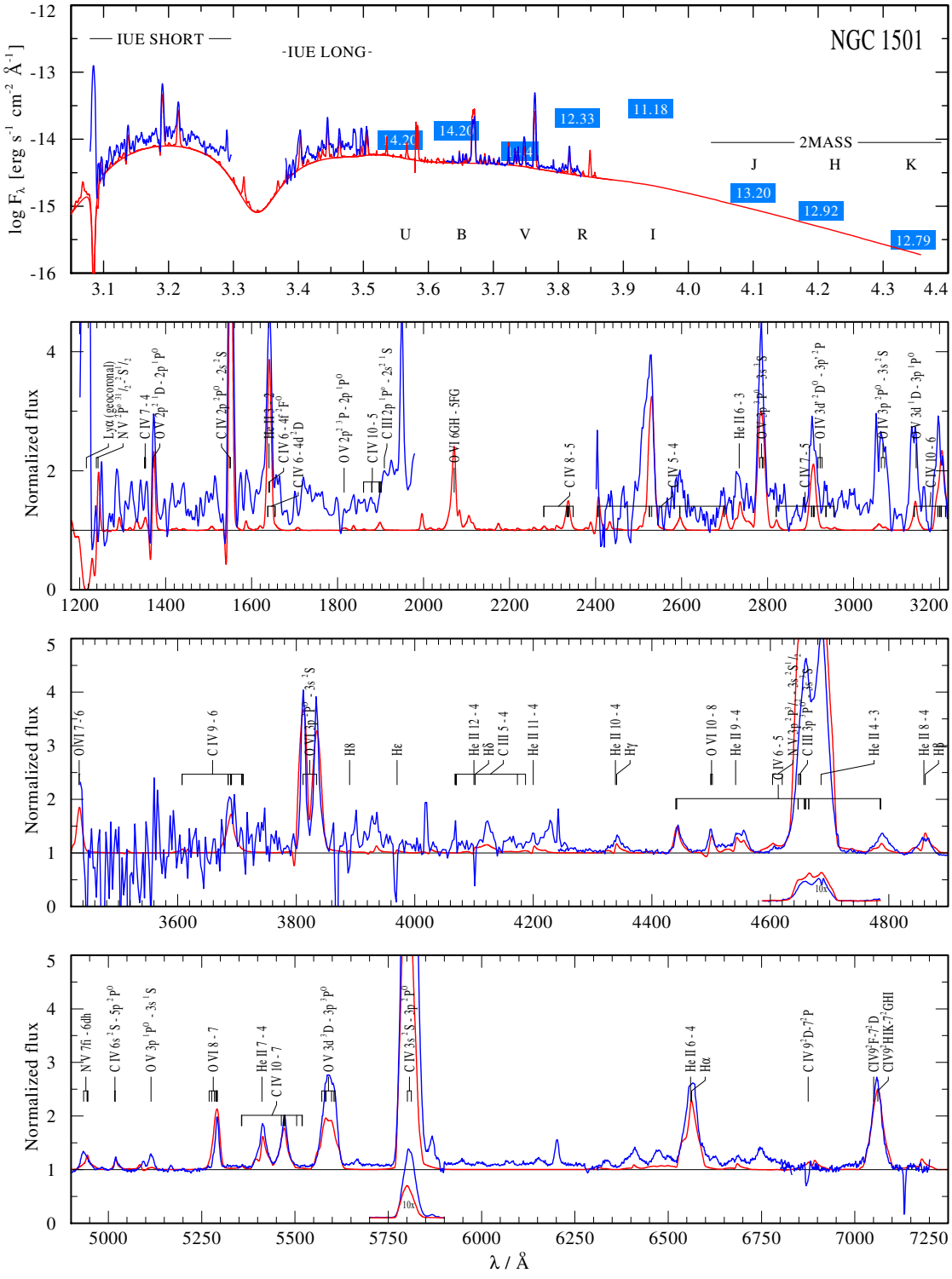

Figure 3.27: NGC 1501: observation (blue line) vs. PoWR model (red).

the 2.1m-telescope. In the optical spectrum the stellar continuum can be clearly seen, while the IUE spectra is too noisy for a certain identification of the stellar continuum.

3.4.10 NGC 6369

Our best fit for NGC 6369 is shown in Fig. 3.28. For NGC 6369 we have only photometric data and an optical spectrum that is not flux calibrated, but rectified by eye. Hence, the SED fit is based on the photometry only. The IUE flux seems to be completely wrong: it is much higher than the photometric values and shows a steep increase to longer wavelength a fit of the model SED to the IUE spectrum would imply a distance of only 3 pc for a CSPN luminosity of 5000, $L_\odot$.

The optical spectrum was obtained at the Calar Alto observatory in 1993. A consistent fit to most of the spectral lines in the optical range, especially to the O VI 3812/34 and the O V $3d^3D$-$3p^3P^o$ line, is achieved with a T_* of 158 kK, an R_t of 1.8 and the abundances and v_∞ by Koesterke (2001).

Although the C IV 5801/12 Å line cannot be reproduced in the observed strength, the other C VI lines are fitted well, the diagnostic line pair even almost perfectly.

3.4.11 NGC 5315

Our optical spectrum was obtained with the ESO-EFOSC in 1992. It is not flux-calibrated and was rectified by eye. Fitting the observed SED from UV spectra and photometry is difficult, as we cannot find a consistent fit of all observations. In particular, the steep increase of the IUE LONG flux cannot be reproduced by any set of parameters. Therefore, our SED fit is based on the IUE SHORT spectrum. Then, our model SED also fits the FUSE flux sufficiently well. For the plot of the normalized flux, the IUELONG spectrum is rectified by eye. Our best fit for NGC 5315 is plotted in Fig. 3.29. A PoWR model with the parameters taken from Marcolino et al. (2007) (see Table 1.1) shows emission lines that are much stronger than in our observation. In particular, the equivalent width of the C III $3d\,^1D$-$3p\,^1P^o$ line would be 10× higher than in the observation. Hence, we choose a model with a smaller mass-loss rate (larger R_t) and lower temperature from our [WC] grid to achieve a mostly consistent fit. The observed iron forest in the IUE range is reproduced only partially by the grid model, but more consistent with the observation than the model with the parameters taken from Marcolino et al. (2007). The higher mass-loss rate of Marcolino et al. (2007) results in an iron forest that is much stronger than in the observation and hence a reduction of the iron abundance in the model would be necessary to reproduce the observation.

However, even with our reduced mass-loss rate, the line strength of the diagnostic line pair is larger than in the observation, although the ratio between the line strengths is the same in observation and model. To keep the line strength of the C III-IV/He II 4-3 line blend, we refrain from a further reduction of the mass-loss rate.

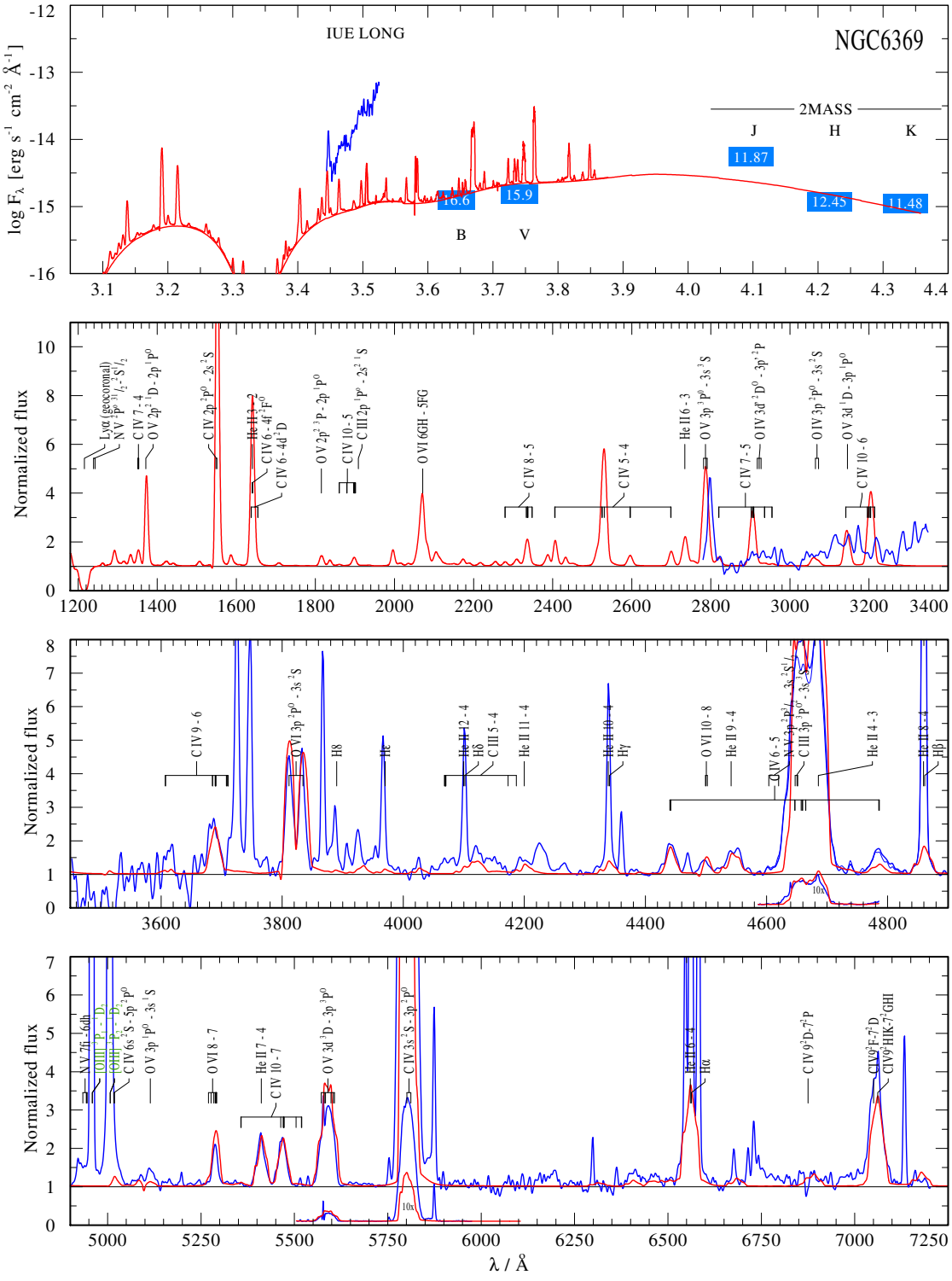

Figure 3.28: NGC 6369: observation (blue line) vs. PoWR model (red). The IUELONG spectrum is normalized by the model continuum, but using arbitrary values for E_{B-V} and distance.

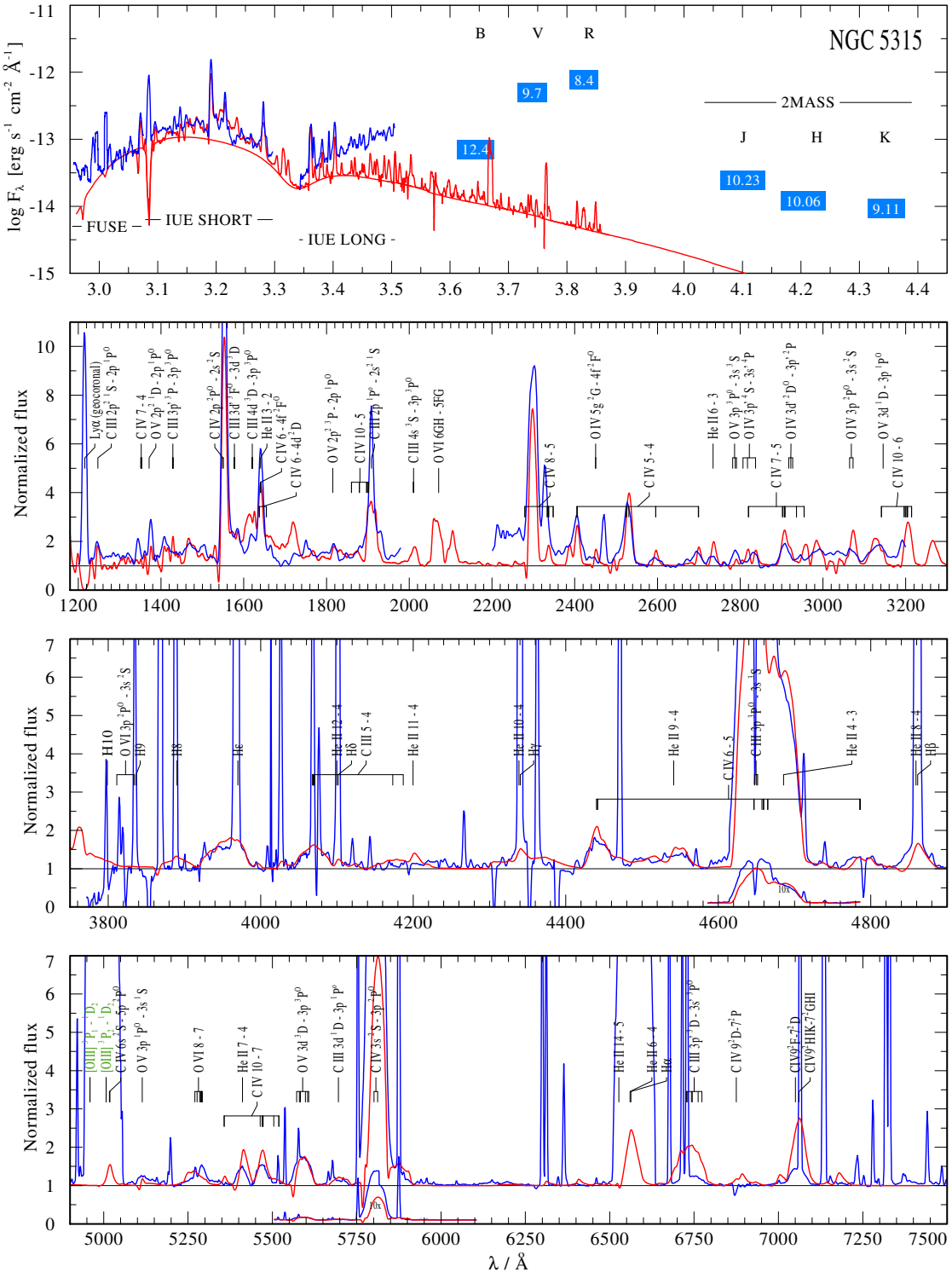

Figure 3.29: NGC 5315: observation (blue line) vs. PoWR model (red). The IUELONG spectrum is normalized by the model continuum, but using arbitrary values for $E_{\mathrm{B-V}}$ and distance.

3.4.12 Summary of the [WCE] spectral analyses

The stellar parameters from our [WCE] analyses are summarized in Table 3.6.

Note that the given mass-loss rates are derived from the transformed radius R_t with help of Eq.(2.1), by assuming a luminosity of $5000\,L_\odot$ and a density contrast of $D = 10$. For constant R_t, $\dot{M}$ scales linearly with v_∞, i.e. if v_∞ differs by 50 % from our mean estimate of $2000\,\mathrm{km\,s^{-1}}$, the given mass-loss rate also differs by 50 %. The dependence of $\dot{M}$ on the luminosity is even weaker with $\dot{M} \propto L^{3/4}$. The largest uncertainty of $\dot{M}$ may arise from the uncertainty of the density contrast D, or in other words from the unknown density structure of the wind. While accounting for microclumping results in a reduction of $\dot{M}$ by a factor of $\sqrt{D}$, calculations that take macroclumping into account have shown that the neglect of the porosity effect may result in an underestimation of the mass-loss rates (Oskinova et al. 2007).

Table 3.6: Results of our analyses of [WCE] stars with line-blanketed models. Given are the revised stellar parameters and abundances. For most of the objects we find the best fit to He, C, and O lines with our default abundances of He:C:O=60:30:10. We also give N abundances, if N lines are clearly visible in the spectrum, otherwise we try to determine an upper limit.

object	X_C	X_He	X_O	X_N	T_*	R_t	$\log \dot{M}$	v_∞
	% mass fraction				[kK]	$R_\odot$	$\log M_\odot\,\mathrm{a}^{-1}$	$\mathrm{km\,s^{-1}}$
NGC 2867	30	60	10	< 0.5	158	5.0	−7.2	2000
PB 6	30	60	10	1.5	158	5.0	−7.2	2000
NGC 5189	30	60	10	1.5	158	5.0	−7.2	2000
NGC 6905	30	60	10	–	150	4.5	−7.0	2000
NGC 7026	30	60	10	< 0.06	130	6.3	−7.1	2000
Hen 2-55	30	60	10	≤ 0.1	126	10	−7.4	2000
[S71d]3	30	60	10	1.5	158	3.2	−6.9	1800
IC 1747	30	60	10	< 0.5	112	10	−7.2	2000
NGC 1501	35	54	10	0.5	128	4.8	−6.9	1700
NGC 6369	30	56	14	–	158	1.8	−6.7	1200
NGC 5315	30	60	10	–	71	5.0	−6.1	2000

3.5 Mass-loss rates from radio observation

For only *one* of our program stars, [S71d]3, radio data have been published. And only for this star, a meaningful radio observation of the stellar wind can be obtained, as there is no contamination by nebular emission expected (see Sect 3.4.7).

Assuming spherically-symmetric expansion of the stellar wind at constant v_∞, and also at constant temperature and constant degree of ionization γ (number of free electrons per ion), that is assured in the outer regions of the wind, where most of the radio emission originates from, the free-free emission of this wind predicted by Wright & Barlow (1975) is

$$f_\nu = 23.2\,\mathrm{Jy}\left(\frac{\dot{M}}{\mu v_\infty}\right)^{4/3}\frac{\nu^{2/3}}{D^2}\gamma^{2/3}g^{2/3}Z^{4/3} \tag{3.3}$$

$$f_\nu = 23.2\,\mathrm{Jy}\,\gamma^{2/3}\left(\frac{Z}{A}\right)^{4/3}\left[\frac{\dot{M}/(\mathrm{M}_\odot\,\mathrm{a}^{-1})}{v_\infty/(\mathrm{km\,s}^{-1})}\right]^{4/3} \times\left(\frac{\nu}{\mathrm{Hz}}\,g_{\mathrm{ff}}\right)^{2/3}\left(\frac{d}{\mathrm{kpc}}\right)^{-2}, \tag{3.4}$$

where Z is the charge of the ion, A the atomic weight, and $g_{\mathrm{ff}} = g_{\mathrm{ff}}(\nu, T)$ is the free-free Gaunt factor. For the radio range, g_{ff} is

$$g \approx 9.77\left(1 + 0.13\log\frac{T^{3/2}}{Z\nu}\right) \tag{3.5}$$

(Abbott et al. 1986).

As the measured radio fluxes are upper limits, the inferred mass-loss rates (each corresponding to a radio observation for a given frequency) are upper limits. The mass-loss rate from our PoWR model is $\log(\dot{M}/[\mathrm{M}_\odot\,\mathrm{a}^{-1}]) = -6.9$, hence much lower than the mass-loss rates obtained from the radio observation, and therefore not in contradiction to it.

Table 3.7: Radio mass-loss rates for [S71d]3, $\mu = 5.5$, $v_\infty = 2000\,\mathrm{km\,s}^{-1}$, and $D = 1.2\,\mathrm{kpc}$.

ν MHz	f_ν Jy	$\log \dot{M}$ $\log(\mathrm{M}_\odot\,\mathrm{a}^{-1})$
1465	< 0.0038	-3.64256
4885	< 0.0009	-4.34666
14965	< 0.0034	-4.12884

3.6 Distances of planetary nebulæ

Although the existence of circumstellar matter like PNe usually hampers the spectral analysis of the star by line contamination, in some cases it can help to estimate the distance to the star and by this allow for the determination of the stellar luminosity.

Unfortunately, the distances of Galactic PNe are quite uncertain as only a few precise parallax measurements exist. Therefore alternative methods have been applied, most of which make use of some assumption about the PN, e.g. recovering the absolute nebular brightness.

Phillips (2004) used a correlation between the 5-GHz luminosity L_5 and the brightness temperature T_B to derive the nebular luminosity. The distance to the PN is obtained from comparison of the derived luminosity and observed brightness.

Tajitsu & Tamura (1998) assumes a uniform dust mass for all PNe. From IRAS fluxes, a blackbody temperature of the dust envelope can be derived and the observed flux is fitted with this temperature and a scaling factor. Tajitsu & Tamura (1998) found a good correlation between this scaling factor and published distances of PNe. Hence, the scaling factor can be calibrated with these PNe distances and used to determine other PNe distances.

Expansion parallax distances

For non-compact, sufficiently extended PNe, which have been observed over years, a more reliable method can be applied: By the determination of the expansion velocity v_exp from the width or splitting of spectral lines in the nebular line spectrum together with the angular expansion $\dot{\theta}$, taken from a time series, the distance d can be obtained by

$$d = v_\mathrm{exp} \,/\, \dot{\theta}\,. \tag{3.6}$$

However, this method assumes, that both velocities originate from the expansion of the nebula material. In fact, this is obviously true only for v_exp, whereas $\dot{\theta}$ usually describes the expansion of the ionization front, which always proceeds faster than the expansion of the matter. Therefore, distances from expansion parallaxes usually underestimate the physical distance and must be corrected by a factor of 1.3 to 3 (Schönberner et al. 2005a). Moreover, the method requires that the expansion in the radial and in the transversal direction proceeds with the same speed (as in a spherically symmetric nebula), or that at least their ratio is known.

At the moment, the only [WC] star, for which an expansion parallax distance has been published, is BD +30 3639. Li et al. (2002), taking the elongated shape of the nebula into account, derive a distance of 1.2 kpc, but without applying any correction for the ionization front expansion.

From this distance estimate, Crowther et al. (2003) and also Marcolino et al. (2007) derive a luminosity of 4250 $L_\odot$ for BD +30 3639, which is reasonable for a CSPN.

CSPN-luminosity distances

By comparison of the observed quantities g and $T_{\rm eff}$ with evolutionary tracks for post-AGB stars of different masses, it is possible to obtain "spectroscopic masses" of CSPNe.

These CSPN masses are found to scatter only mildly around $0.6 \pm 0.3\,M_\odot$ (cf. Fig. 3.30, which is also consistent with the mass distribution found for white dwarfs, which are the presumed descendants of the CSPNe. Therefore it is expected that for a given mass-luminosity relation the range of CSPN luminosities is not too extended.

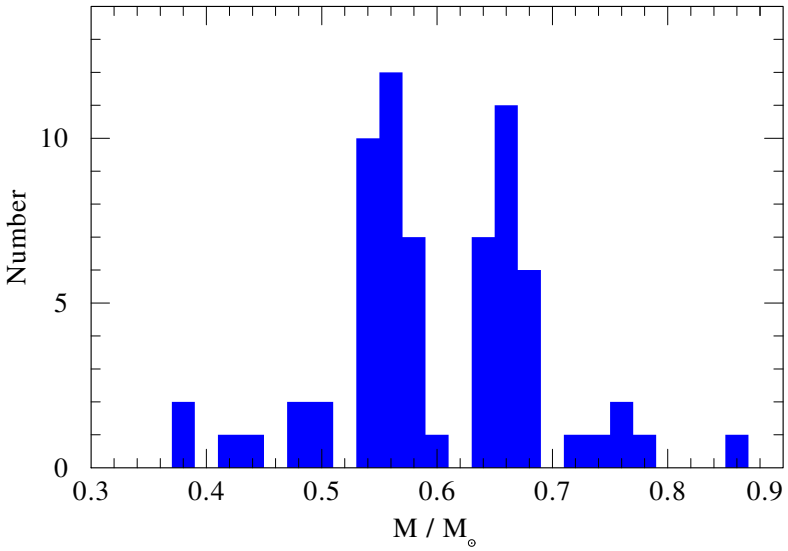

Figure 3.30: Distribution of "spectroscopic" CSPN masses (Tylenda 2003). The masses fall all in the range between 0.38 and $0.86\,M_\odot$. The distribution is bimodal with a mean of $0.6\,M_\odot$. Interestingly, the distribution has a clear minimum at the mean value.

Surprisingly, theoretical models by Paczyński (1970) for Pop I stars after core helium burning predict a linear core-mass luminosity relation of

$$L/L_\odot = 59250\,M_{\rm core}\,/\,M_\odot - 30950 \tag{3.7}$$

for $0.57 < M_{\rm core} < 1.39$. According to the evolutionary tracks, the luminosity stays constant through the regime of CSPNe as long as there is enough envelope material to support nuclear shell burning.

This relation can be violated in the case of models with hot-bottom burning or efficient third dredge-up (Herwig et al. 1998). Then the core-mass luminosity relation is a function of the core radius, too:

$$L \sim M_{\rm core}^2\,R_{\rm core}^{-1}\ . \tag{3.8}$$

If the electrons in the core are degenerated, as for a white dwarf, the relationship between mass and radius is simply $M \sim R^{-1/3}$, and the core-mass luminosity relation of Eq. (3.8)

can be written as

$$L \sim M_{\rm core}^{7/3} \approx M_{\rm core}^{2.3}. \tag{3.9}$$

H-deficient central stars, especially those that have suffered a very late thermal pulse, cannot longer support hydrogen shell burning. Instead they support helium shell burning only. However, the evolutionary tracks of H-normal and H-deficient central stars lie in the same $T_{\rm eff} - L$ regime, albeit the time scales may be different. So, tracks of H-normal central stars may be used as a tool for determination of masses of H-deficient stars (Werner & Herwig 2006).

Following Paczyński (1970), an $0.6\,M_\odot$ H-normal post-AGB star has a luminosity of $\log(L/L_\odot) = 3.67$. Therefore we have chosen a canonical value of $\log(L/L_\odot) = 3.7$. This is similar to the luminosity of H-normal central stars according to Schönberner et al. (2005b) of $\log(L/L_\odot) = 3.78$. By assuming a luminosity for our sample stars we can compare the synthetic and observed stellar SEDs, and obtain the distance. Luminosity distances, together with $E_{\rm B-V}$ and $R_{\rm V}$ from the SED fit are presented in Table 3.8.

Table 3.8: Distances to [WC]-type central stars derived from the PN or stellar luminosity (4th column), respectively. D(Phillips) by (Phillips 2004) and D(Tajitsu) from (Tajitsu & Tamura 1998). Uncertainties in D(Phillips) are of the order of $\sigma(D) \sim 0.18$. Also given are $E_{\rm B-V}$ and $R_{\rm V}$ from the SED fit. For NGC 6369, the fit is based on the photometry only.

object	D(Phillips) [kpc]	D(Tajitsu) [kpc]	$D_{5000\,L_\odot}$ [kpc]	$E_{\rm B-V}$	$R_{\rm V}$
NGC 2867	1.69	2.3	3.2	0.24	3.1
PB 6	3.55	4.1	4.8	0.28	3.1
NGC 5189	0.55	0.9	1.6	0.29	3.1
NGC 6905	1.62	2.2	1.8	0.21	3.1
NGC 7026	1.91	1.8	0.5	1.0	3.1
Hen 2-55	–	7.2	5.9	0.35	2.0
[S71d]3	–	–	0.9	0.5	4.0
IC 1747	2.23	4.7	1.0	1.1	3.0
NGC 1501	1.03	2.6	1.5	0.72	2.5
NGC 6369	–	0.8	1.0	1.2	3.1
NGC 5315	2.14	0.9	3.8	0.35	3.1

Zanstra temperatures

From the nebular emission lines, it is possible to get an estimate of the stellar temperature. The method is known as Zanstra method (Zanstra 1927) and gives a lower limit for the blackbody temperature of the star within the nebula.

Although the method can also be applied for He emission lines, it is briefly explained for the Balmer lines, for which it was originally used (cf. Ambarzumjan & Mustel 1957). The Balmer emission lines are formed by recombination of H II in the nebula (together with a Lyα photon), where the hydrogen is ionized by H-ionizing photons (L_c photon) emitted by the central star. Thus, for every photon of a Balmer line, a stellar L_c photon is needed and for their numbers, there is a simple relation

$$N(\mathrm{Balmer})_{\mathrm{neb.}} \leq N(\mathrm{L_c})_{\mathrm{star}}. \tag{3.10}$$

Equality holds for nebulæ that are optically thick to L_c photons.

Assuming blackbody radiation from the star, the number of ionizing photons $N(\mathrm{L_c})_{\mathrm{star}}$ is given by

$$N(\mathrm{L_c})_{\mathrm{star}} = 4\pi R_*^2 \frac{2\pi}{c^2} \int_{\nu_0}^{\infty} \frac{\nu^2 d\nu}{e^{\frac{h\nu}{kT_*}} - 1}, \tag{3.11}$$

where ν_0 represents the Lyman-limit.

The number of Balmer photons can be estimated by adding up a dimensionless quantity A_i over all Balmer lines plus the Balmer continuum. A_i is the energy E_i of the i-th Balmer line normalized to the energy emitted by the star at the line frequency (stellar continuum):

$$A_i = \frac{E_i}{\nu_i \left(\frac{\partial E_*}{\partial \nu}\right)_i}. \tag{3.12}$$

A_i can be retrieved from observation, but is also given by

$$\left(\frac{\partial E_*}{\partial \nu}\right)_i = 4\pi R_*^2 \frac{2\pi h \nu_i^3}{c^2} \frac{1}{e^{\frac{h\nu_i}{kT_*}} - 1} \tag{3.13}$$

Hence, from the inequality (3.10) another inequality can be derived, from which a lower limit of T_* can be obtained:

$$\sum_i \frac{\nu_i^3 A_i}{e^{\frac{h\nu}{kT_*}} - 1} \leq \int_{\nu_0}^{\infty} \frac{\nu^2 d\nu}{e^{\frac{h\nu}{kT_*}} - 1} \tag{3.14}$$

The method can be applied analogously for the nebular He I and He II emission lines.

In Table 3.9 we give the Zanstra temperatures as predicted by our PoWR models and compare it with the Zanstra temperatures measured from the nebula.

Note that according to Pakull (2009), for the same T_*, PoWR models predict roughly 10× less He^+-ionizing photons than CMFGEN models. If the PoWR models underestimated the He^+-ionizing flux, the He II-Zanstra temperatures that are predicted from our models would be lower than the observed He II-Zanstra temperatures, e.g. as for NGC 5315.

For NGC 2867 and NGC 6369, our Zanstra temperatures are higher than those inferred from the nebular emission. This discrepancy could mean that the nebula is not optically thick in all directions of the ionizing radiation, as indicated by inequality (3.10).

Table 3.9: Zanstra temperatures: from observations (Shaw & Kaler 1989) of the nebula vs. predictions of PoWR models. We do not give Zanstra temperatures for [S71d]3, since it has no PN.

PN	T_Z(H I) neb.	T_Z(H I) model	T_Z(He II) neb.	T_Z(He II) model
NGC 2867	85	134	115^{+15}_{-11}	125
PB 6	–	134	–	125
NGC 5189	–	135	–	124
NGC 6905	–	120	–	111
NGC 7026	–	115	–	97
Hen 2-55	–	125	–	99
IC 1747	–	113	–	80
NGC 1501	–	104	–	87
NGC 6369	58 ± 2	84	–	78
NGC 5315	56	54	61 ± 8	18

4 Discussion

To explain the formation of hydrogen-deficient central stars, different scenarios of late or final thermal pulses have been developed, e.g. Iben et al. (1983); Herwig et al. (1999); Herwig (2001); Althaus et al. (2005). Referring to the time of occurrence, the models are classified as AGB final thermal pulse (AFTP), late thermal pulse (LTP), or very late thermal pulse (VLTP). Now, to choose the appropriate scenario, one has to compare the predictions of the different scenarios with the observations of hydrogen-deficient central stars. The most important differences between the scenarios are the predicted ages of the PNe and the abundance patterns. While the age of a PN that is derived from observations depends on its adopted distance, which is usually very uncertain, the surface abundance of the central star provides a distances-independent indicator to choose the adequate scenario from stellar evolution theory.

With help of the PoWR code we have determined surface abundances of hydrogen-deficient central stars. In the following, the derived element abundances are discussed and compared to the predictions from stellar evolution theory.

4.1 Chemical abundances of [WC] central stars

4.1.1 Helium and carbon abundances

Regarding the carbon and helium abundances, previous analyses, using the PoWR code, resulted in different abundance patterns for galactic [WCE] and [WCL] stars. Within the favored evolutionary scenario for [WC] stars (see e.g. Werner 2001), which claims the existence of a sequence of [WCL] → [WCE] stars, this discrepancy cannot be understood (cf. Sect. 1.3.5).

As the first analyses of [WC] stars have been performed with unblanketed PoWR models, which also have not accounted for microclumping, we started a re-analyses of the [WCE] stars with the most recent version of the PoWR code.

Our analyses of [WCE] stars with line-blanketed models confirmed the He:C abundances of 60:30 by mass on average. This abundance ratio is necessary to reproduce the spectral lines of the diagnostic line pair C IV-He II in equal strength as it is observed for the [WCE] stars of the sample. He:C abundances of 40:50 as reported by Crowther et al. (2003); Stasińska et al. (2004); Marcolino et al. (2007) do not reproduce the observed line strengths of the diagnostic line pair. Instead, in the simulated spectra the C IV is stronger, and the He II is weaker than observed.

The nebulæ of the hottest [WCE] stars show He II emission, which may contaminate the diagnostic stellar He II 7-4 line. However, with sufficient spectral resolution ($R > 6000$) the different contributions can be distinguished. The stellar line is broadened by the

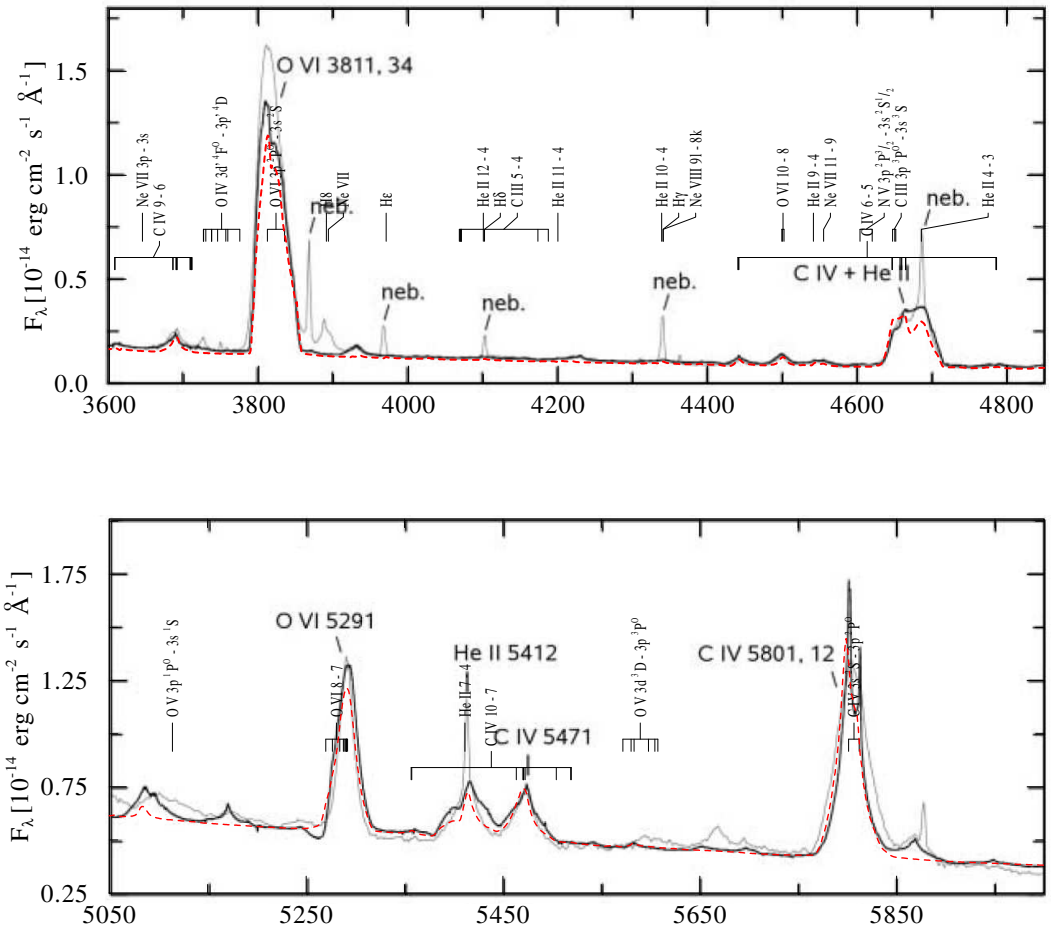

Figure 4.1: NGC 6905: Observation (grey thin line) and CMFGEN model (black thick line) adopted from Marcolino et al. (2007), plotted together with our best fit PoWR model (red dashed line). Both models have similar parameters, but differ mainly in the He:C abundance. While the model by Marcolino et al. (2007) contains 49 % He and 40 % C, our PoWR model has 60 % He and 30 % C. However, both models seem to fit sufficiently the observation.

stellar wind with $v_\infty \approx 2000\,\mathrm{km\,s^{-1}}$, while the nebular lines only show the nebular expansion with $v_\mathrm{exp} < 100\,\mathrm{km\,s^{-1}}$.

The accuracy of the element abundances which we derive from the fits is hard to estimate. Different spectral lines often require models with slightly different parameters for a perfect match. The "final model" is usually a compromise.

This may be illustrated for NGC 6905: We adopted the figure that shows the observation

and the model from Marcolino et al. (2007) and plot it together with our PoWR model in Fig. 4.1. Although having slightly different parameters (cf. Tab. 1.1 and Tab. 3.6), both model fit more or less the observation - none of the spectral lines is matched really perfectly in the given resolution, but a good agreement between the models and the observation can be stated in general. However, both models do not differ that much in their parameters and abundances, and therefore we should consider these differences to be uncertainties in the determination of parameters from stellar wind models.

It would be interesting do the same comparison of models for NGC 5315, because of the larger discrepancy between the He:C abundance ratio obtained by our analyses and those of Marcolino et al. (2007). Unfortunately, our spectral fit for this star is worse than for NGC 6905. In particular, the absolute line strengths of the C IV 3p-3s line and the diagnostic line pair (cf. Fig 3.29) are not reproduced sufficiently. However, the ratio between the line strengths of the diagnostic line pair C IV-He II is reproduced by our PoWR model with 60 % He and 30 % C, as usual. Moreover, the model of Marcolino et al. (2007) shows stronger emission lines of the diagnostic line pair than observed (like for our PoWR model). Furthermore, the discrepancy between the observed and calculated line fluxes seems to be larger for the C IV line than for the He II line. This could mean that the carbon abundance in the model is too high.

Again, we would like to emphasize the value of the diagnostic C IV-He II line pair. As we had shown and discussed in Section 3.3.1, its line strengths depends almost only on the He:C abundance ratio.

Models for [WCE] stars predict that almost all carbon is ionized to C V throughout the wind, and helium is completely ionized to He III. As most of the emission lines are formed in a recombination cascade, the dominant lines are those of ionization stage below the leading ion, i.e. of C IV and He II. The situation is different for the [WCL] stars, which are cooler and hence, show a more complex ionization stratification. So, for [WCL] stars, spectral lines arising from lower ionization stages are expected to appear in the spectrum. One may have C III and C IV lines of equal strength, but depending strongly on the chosen R_t, T_*. Thus it is not longer possible to derive an abundance ratio of He:C directly from only two spectral lines. Instead, carbon and helium abundances are determined separately from the absolute strengths of all spectral lines. Therefore, the uncertainty of the He:C abundance ratio may be larger than occasionally thought.

In summary, we find the He:C abundances to be roughly 60:30 by mass. In comparison to the analysis of NGC 6905 by Marcolino et al. (2007), we estimate the uncertainty for the carbon and helium abundances to be roughly ± 10 % by mass. Hence, while relying on the diagnostic C IV-He II line pair, even with line-blanketed models, the carbon abundances of [WCE] stars are found to be systematically lower than those for [WCL] stars, for which carbon abundances of about 50 % have been established (see previous analyses in Tab. 1.1).

4.1.2 Hydrogen

The clear detection of hydrogen in [WC] stars would be interesting, as the VLTP scenario predicts a completely hydrogen-free [WC] star.

De Marco et al. (1997) attributed the red wing of the nebular Balmer line of Hen 2-113 to nebular emission by comparison with the (nebular) [O I] line (Fig. 1 in De Marco et al. 1997) and therefore refuted the detection of stellar hydrogen by Leuenhagen et al. (1996). However, for IRAS 21282+50, a nebular origin of the broad red wing of the Hα lines seems to be unlikely, as the nebular [N II] line has no similar feature (cf. Fig. 1.2).

Furthermore, the optical spectrum of V 348 Sgr in the analysis of Leuenhagen & Hamann (1994) is not contaminated by nebular emission, as the nebular spectrum is outshined by the central star. There, the Hα line has a P Cygni line profile, typical for spectral lines arising from expanding atmospheres. In contrast to hotter [WCL] stars, for V 348 Sgr with $T < 25\,000$ K, no He II emission is expected, which could be confused with the Balmer lines.

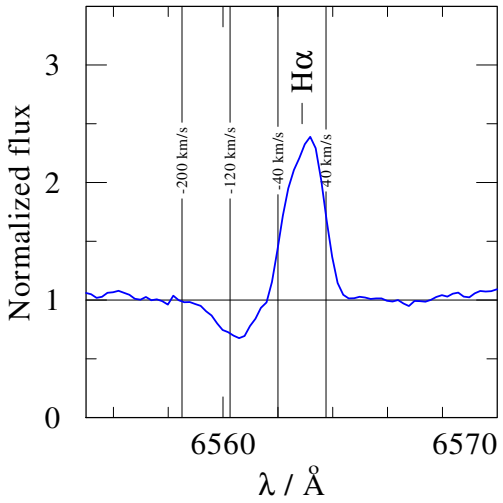

Figure 4.2: Detail of the optical spectrum of V 348 Sgr, showing a P Cygni line profile of the Hα line and hence indicating a stellar origin of the spectral line. Note the velocity scale, for V 348 Sgr the terminal velocity of the stellar wind is $v_\infty = 190\,\mathrm{km\,s^{-1}}$.

4.1.3 Oxygen

With an oxygen abundance of 10% by mass, we find generally a good agreement between the calculated and observed O VI lines. As aforementioned (see Sect. 3.3.2), the considerable strength of the O VI 3811/34 Å line of the [WO] stars is a non-LTE effect caused by iron line blanketing and occurring only for $T_* > 150$ kK. In some of the observed [WCE] spectra, O V lines are visible as well. Models that can reproduce the very strong O VI 3811/34 Å line fail to reproduce the observed line strength of the O V lines (e.g. for

[S71d]3), due to the high T_*. However, our oxygen abundance of 10 % by mass agrees very well with values found by other authors for [WCE] stars. Among the existing scenarios that can explain the formation of [WC] stars, only the AFTP scenario predicts oxygen abundances of about 10 % by mass. The LTP and VLTP scenarios predict much higher mass fractions of oxygen of about 20 %.

4.1.4 Nitrogen

As pointed out by Werner & Herwig (2006), nitrogen is a tracer element for the VLTP scenario, because only by the VLTP it can be produced via $^{12}\mathrm{C}(\mathrm{p},\gamma)^{13}\mathrm{N}$ in a considerable amount of a 1 . . . 2 %. E.g., the VLTP model by Althaus et al. (2005) yields 1.2 % by mass.

For three objects of our sample - PB 6, NGC 5189, [S71d]3 - we find strong N V lines, from which we infer a nitrogen abundance of 1.5 % by mass.

This result is different from the findings of Koesterke & Hamann (1997b), who determined a mass fraction of nitrogen of only 0.005 for [S71d]3. Our analyses of nitrogen abundances are based on three N V line multiplets: in the IUE at 1239/43 Å, in the optical range at 4604/4620 Å, and at 4933-4944 Å. The latter one is a very strong line, but which was confused with an O V line by Koesterke & Hamann (1997b) and therefore not included in their analyses.

However, the N V 4933-4944 Å line is a reliable indicator for the nitrogen abundance, as its line strength depends only weakly on T_*, R_t (see Fig. 3 in Hamann & Gräfener 2004).

Unfortunately, this line is close to the extremely bright [O III] nebular emission line. Hence, for many [WCE] stars, e.g. for NGC 2867, this part of the spectrum is contaminated by the nebular emission and cannot be used for the determination of the nitrogen abundance. Instead, we have to rely on the N V 4604/4620 Å line, which is much weaker and blended with a strong carbon emission line. For weak lines, the uncertainty in the continuum used for normalization limits the accuracy of the analyses. This problem is also for the strong N V resonance line in the UV range, where the observed stellar continuum is strongly affected by the interstellar reddening and Lyα absorption. Moreover, a fit of our reddened stellar continuum to the IUE observation in this part of the spectrum is often complicated by geocoronal Lyα emission.

However, for the three [WCE] stars, PB 6, NGC 5189, and [S71d]3, the nitrogen abundances are certainly supersolar with a mass fraction of 1.5 %, similar to the nitrogen abundance created by the CNO cycle.

4.1.5 Neon

As mentioned in Sect. 1.3, neon abundances of a few percent by mass are predicted from the VLTP scenario, e.g. Herwig et al. (1999); Althaus et al. (2005).

For NGC 5189, NGC 6905, [S71d]3, at 2220-2234 Å we find a strong emission line that we identify as the Ne VI 3d-3p line, according to Herald & Bianchi (2004). Additionally, lines of Ne VII and Ne VIII are found in the FUSE and optical range.

Our PoWR models, accounting for neon, are able to reproduce the observed neon lines qualitatively, i.e. absorption lines, emission lines and P Cygni profiles.

However, we cannot reproduce the observed line strengths of Ne VI - VIII consistently. Even by a mass fraction of 3 %, most of the neon emission lines are much weaker than in the observation, while the Ne VII 3644 Å absorption line is much stronger than observed.

Interestingly, these stars have also strong neon lines in their spectra. Neon abundances of a few percent are predicted from the VLTP scenario as well. Note that the correlation found in the [WCE] spectra of our sample is not strict: the spectrum of NGC 6905 shows strong neon lines, but the N V are much weaker than for NGC 5189 etc., and the UV resonance line seems to be completely absent.

4.1.6 Iron

The recent PoWR models account for line-blanketing by the iron-group elements. For some [WC] stars, with certain parameters, the iron spectral lines form a pseudo continuum ("iron forest") in the UV range, found e.g. for LMC-SMP 61 by Stasińska et al. (2004). However, only for NGC 5315, the model reproduces an iron forest that is also visible in the observation. Although the observed iron forest in the IUE SHORT range is reproduced only partially, we do not find clear indications for an iron deficiency, as reported by Marcolino et al. (2007). As the strength of the iron forest is also influenced by T_*, R_t, a too strong iron forest can also be the result of an inappropriate temperature or mass loss rate.

4.2 Conclusion

New observations with improved spectral resolution and recent models accounting for iron-line blanketing, wind inhomogeneities (microclumping) and new atomic data, including higher ions, are used to determine element abundances and stellar parameters of [WCE]-type central stars.

In particular, we revisited the abundances of [WCE] stars to check for the carbon abundances, which are found to be systematically lower than for [WCL] stars, as found by Leuenhagen and co-workers. We confirm the lower carbon abundances of [WCE] stars as determined by Koesterke & Hamann (1997a); Koesterke (2001), and which are in contrast to other authors.

We conclude that the putative evolutionary sequence [WCL] → [WCE] is challenged by the different abundance pattern with respect to helium and carbon.

For the first time, we find clear evidence of nitrogen to be overabundant with 1.5 % by mass in three of our [WCE] stars, NGC . Following (Werner & Herwig 2006), nitrogen abundances of a few percent by mass can be only created in the VLTP scenario, but not in the AFTP or LTP scenario. However, for NGC 2867, whose spectrum looks almost identical to those of PB 6 and NGC 5189, we infer an upper limit of the nitrogen abundance of 0.5 %. For other stars, like NGC 7026 we find even lower nitrogen abundances. So, according to the scenarios by Herwig (2001) and if the [WC] stars, or at least the [WCE]

stars formed a homogeneous class, originating from the same scenario, one would expect similar nitrogen abundances in all of the [WC] stars.

Neon lines are identified and can be qualitatively reproduced with our wind models for [WCE] stars. At the moment our models do not allow for a certain determination of the neon abundances, although the strength of the observed neon lines for e.g. NGC 5189 suggests a neon abundance of a few percent. Stellar evolutionary models by Herwig et al. (1999); Althaus et al. (2005) for the VLTP scenario predict similar values of the neon abundance. The presence of strong neon *and* nitrogen lines in the spectra of PB 6, NGC 5189, and [S71d3] suggests a VLTP origin of these stars. However, for the late-type [WC] star V 348 Sgr, Leuenhagen and co-workers determined a neon abundance of 2 % and a nitrogen abundance of $0.5 \ldots 1$ % (by mass) as well, although stellar hydrogen lines can be found in its spectrum. From the hydrogen lines, Leuenhagen & Hamann (1994) derived a hydrogen abundance of a few percent by mass. Hydrogen in small amounts is predicted to be left after the occurrence of an AFTP or LTP, but not for the VLTP scenario, where the mass fraction of the remaining hydrogen is predicted to be below 10^{-7}. However, only for the VLTP scenario a nitrogen and neon abundance of few percent by mass is predicted.

Moreover, only for the AFTP scenario oxygen abundances of 15 % are predicted, which would be still consistent with the results from spectroscopic analyses. VLTP models by Herwig et al. (1999); Althaus et al. (2005) yield oxygen abundances of roughly 20 % by mass, which is not observed for any of the [WC] stars.

5 Analyses of hydrogen-deficient non-[WC] stars

5.1 PN PB 8

5.1.1 Introduction

The central star (CS) of the planetary nebula PB 8 (PN G292.4+04.1) was first classified by Méndez (1991) as a hydrogen-rich Of-WR(H) star due to the Hγ P Cygni profile and the appearance of an unusually strong He II 4686 emission line.

In contrast, Acker & Neiner (2003) classified this star as a [WC5-6] type star.

In the following, we analyze optical, IUE, and FUSE spectra of the central star PB 8 by means of the Potsdam Wolf-Rayet (PoWR) model atmosphere code. The observations are introduced in section 5.1.2. In Sect. 5.1.3 we describe the spectral analysis, and finally the results are discussed in the final section (Sect. 5.1.4).

5.1.2 Observations

Optical spectrum

High resolution spectroscopy for PB 8 was performed on May 9, 2006 at Las Campanas Observatory (Carnegie Institution) with the Clay 6.5m-telescope and the double echelle spectrograph MIKE (Magellan Inamori Kyocera Echelle). This spectrograph operates with two arms which allow the observer to obtain blue and red spectrum simultaneously. The standard grating settings provided wavelength coverage of $3350 - 5050$ Å for the blue and $4950 - 9400$ Å for the red. Three spectra with exposure times of 300, 600 and 900 s were obtained. The slit width was $1''$ and was centered on the central star. A binning of 2×2 pixels was used, providing a plate scale of $0.26''$ per pixel. The spectral resolution varied from 0.14 Å to 0.17 Å in the blue and from 0.23 Å to 0.27 Å in the red as measured by using the comparison lamp.

The data was reduced using standard procedures from the IRAF reduction packages. Spectra were extracted with a $1.52''$ wide window and flux calibrated with respect to standard stars. The three spectra were then weighted by exposure time and were finally combined.

UV spectra

A low-resolution spectrum from the International Ultraviolet Explorer (IUE) in the range from 1200 to 2000 Å and a high-resolution spectrum from the Far Ultraviolet Spectroscopic Explorer (FUSE) from 960 to 1190 Å have been retrieved from the MAST archive. For the IUE range, we use an exposure-time weighted combination of the spectra SWP28434LL ($t_{\rm exp} = 2400$ s) and SWP30476LL ($t_{\rm exp} = 7800$ s), both were taken using

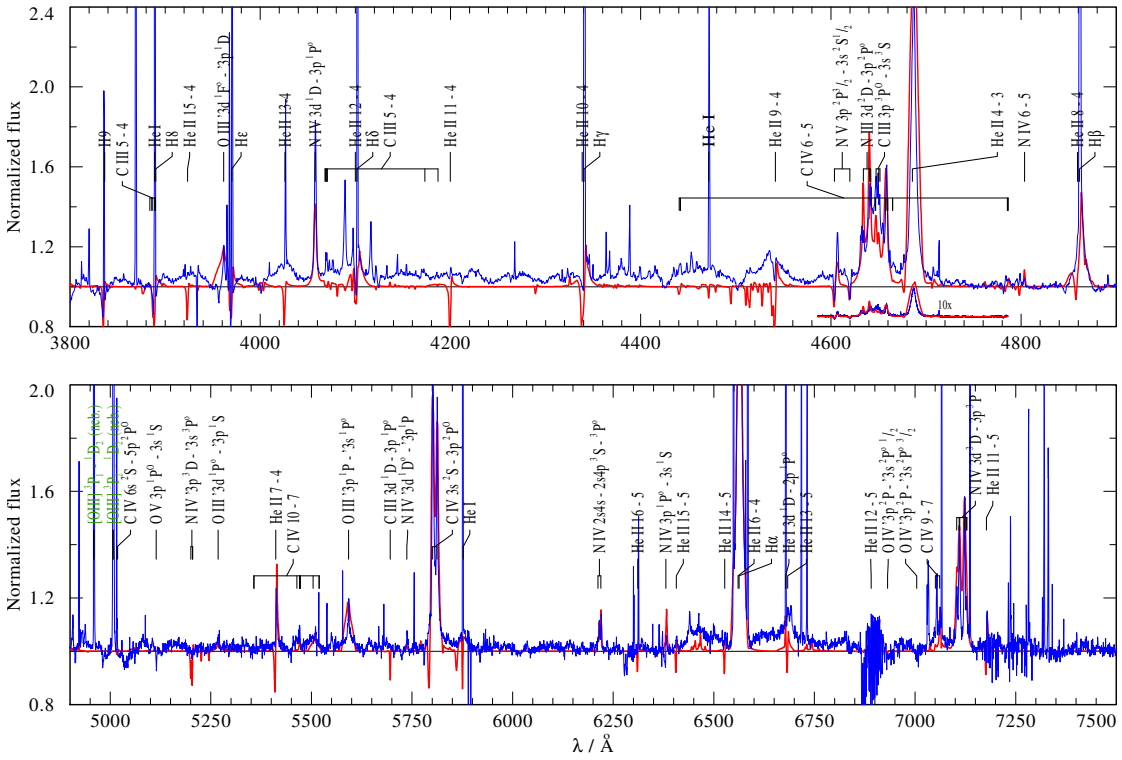

Figure 5.1: Optical spectrum: observation of PB 8 (blue, thin line) and PoWR model (red, thick line), both normalized to the model continuum. The observation is rebinned to 0.5 Å . The observed stellar spectrum is contaminated by the narrow nebular lines.

the "large" aperture. The spectral resolution is about 5 Å , and the estimated S/N ratio is roughly 10 for $1200 - 1700$ Å and 20 for $1700 - 2000$ Å .

A FUSE observation of PB 8 has been performed with the LWRS aperture of $30'' \times 30''$ in run Z9111301000. We use the coadded spectrum "all4ttagfcal" from the CalFUSE pipeline, which is already rebinned to 0.1 Å to improve the S/N ratio, but still sufficient to resolve interstellar H_2 absorption lines.

5.1.3 Analysis

Models with non-clumped wind ($D = 1$) predict e.s. wings to be stronger than observed. For the central star of PB 8 we find that $D = 10$ is consistent with observation (cf. Fig. 5.4).

For the terminal velocity v_∞, we obtain a value of $1000\,\mathrm{km\,s^{-1}}$ from the width of the P Cygni line profiles (cf. Fig. 5.6). Note, that the width of the absorption profile is fitted by our model B, but not the rather round shape of the profile. Therefore, a similar model with same $v_\infty = 1000\,\mathrm{km\,s^{-1}}$ but with a different velocity field, described by a

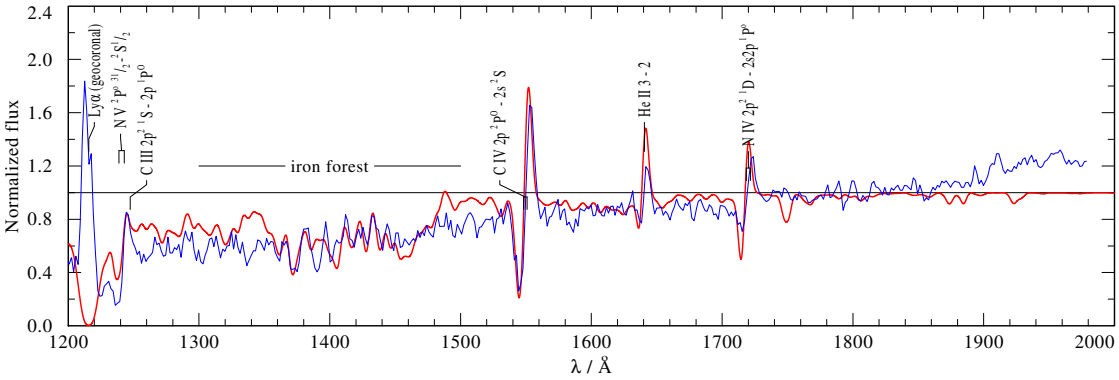

Figure 5.2: Observed IUE spectrum of PB 8 (blue, thin line) vs. PoWR model (red, thick). The observed spectrum was normalized by the model continuum. The synthetic spectrum was folded with a Gaussian with a FWHM of 5 Å, corresponding to the spectral resolution of the IUE observation. The iron forest is only partially reproduced.

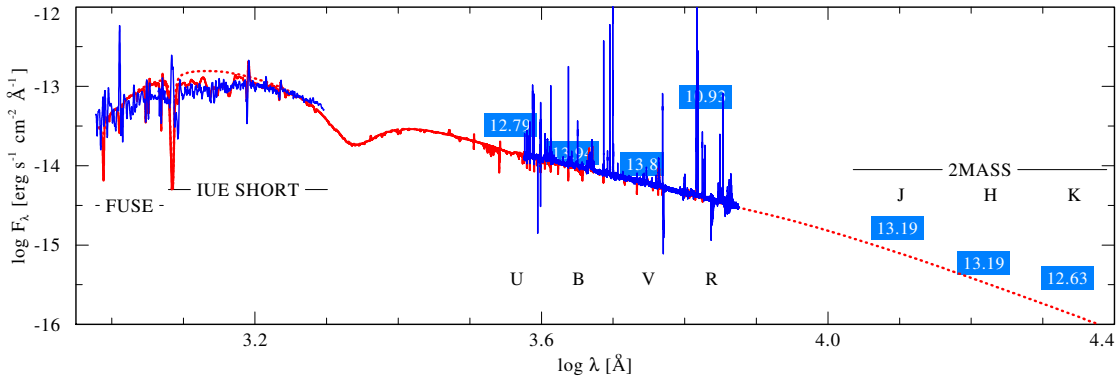

Figure 5.3: Spectral energy distribution for CS PB 8, model vs. observation. Observed spectra (blue thin lines) are from FUSE, IUE, and MIKE (see Sect. 5.1.2). Photometric values (blue blocks) taken from Acker et al. (1992) for UBV, Space Telescope Science Institute & Osservatorio Astronomico di Torino (2001) for R, and 2MASS (Skrutskie et al. 2006) for JHK are partly contaminated by nebular emission. The calculated spectrum (red line) is for the model parameters in Table 5.3. The model flux has been reddened with $E_{\mathrm{B\text{-}V}} = 0.4$ and $R_{\mathrm{V}} = 4$, and corrected for interstellar Lyman line absorption. The model continuum without lines is also shown for comparison (red dotted). Note that in the IUE SHORT range the iron spectral lines form a pseudo-continuum.

double-β law (Hillier & Miller 1999) is calculated (cf. Fig. 5.5). The double-β law mimics the hydrodynamically consistent solution for the velocity field (Gräfener & Hamann

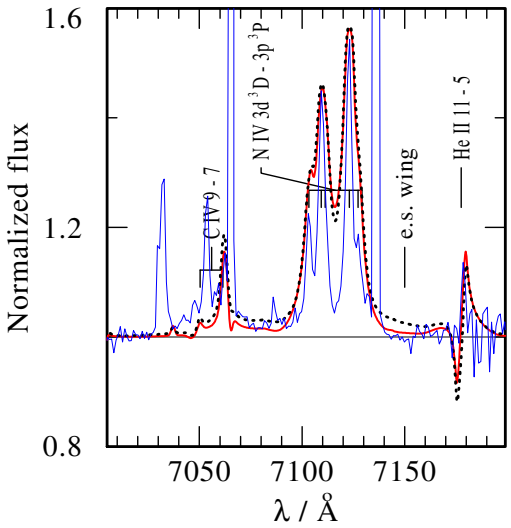

Figure 5.4: Electron scattering (e.s.) wings for two similar models with same R_t but different density contrast D. The homogeneous model (black dotted line) predicts stronger e.s. wings than observed (blue solid). Despite the uncertainty due to normalization to the continuum, the model with $D = 10$ (red solid) seems to be more consistent with the observation, although a higher clumping factor D cannot be excluded. The observation is rebinned to 1 Å for noise reduction.

2005). We choose $\beta_2 = 8$ and a contribution of 50 % to v_∞ to obtain our best fit to the observed P Cygni Profile. Using the double-β law, the velocity in the outer parts of the atmosphere increases more slowly than for the standard $\beta = 1$ law. Hence, as a result of the continuity equation, the wind density drops more slowly for the double-β law and spectral lines formed in the outer regions are stronger than in the case of the standard $\beta = 1$ law. A reduction of the mass loss rate would be necessary to recover the observed line strengths, but with the side effect of too weak helium lines. Thus, we cannot find a totally consistent fit applying the double-β law.

Regarding these difficulties, the additional line broadening of $50\,\mathrm{km\,s^{-1}}$ due to microturbulence, and the resolution of the given FUSE spectrum of $\Delta v = 27\,\mathrm{km\,s^{-1}}$, we give a conservative estimate of the uncertainty in v_∞ of $100\,\mathrm{km\,s^{-1}}$.

Additional line broadening by microturbulence is also included in our models. From the shape of the line profiles we deduce a microturbulence velocity of less than $50\,\mathrm{km\,s^{-1}}$.

Stellar luminosity and mass are set to typical values, $L = 6000\,L_\odot$ and $M = 0.6\,M_\odot$ (see e.g. Schönberner et al. 2005b; Miller Bertolami & Althaus 2007). The absolute flux of the model is diluted by its distance, which we consider to be a free parameter, as no certain distance is known. With help of Eq. (2.1), the results can be easily scaled to a different luminosity. The value of M has no noticeable influence on the synthetic spectra.

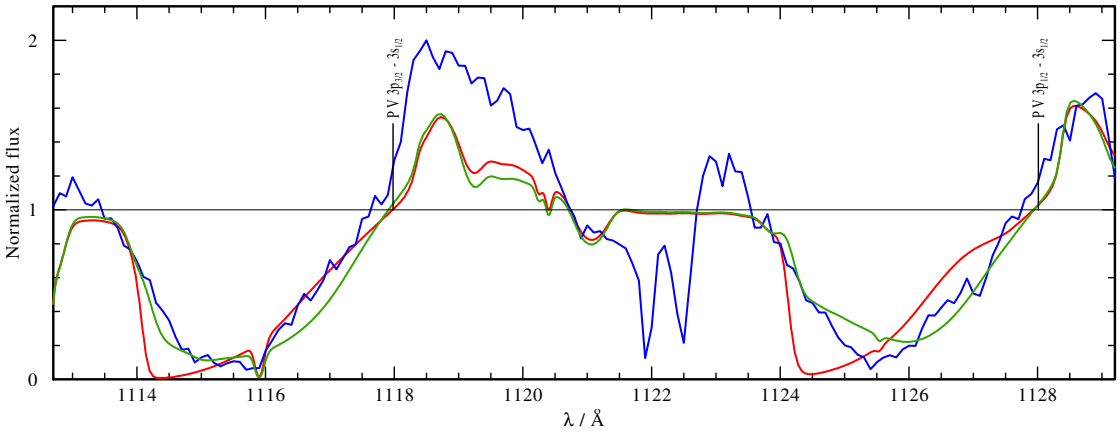

Figure 5.5: Detail of the FUSE spectrum showing the P V resonance doublet, observation (blue line) vs. two PoWR models (including ISM absorption) with different velocity fields. Although the width of the absorption trough can be fitted by our model B (red), the absorption profile shows clear deviations, indicating a velocity law, that is different from the standard β-law. Therefore, we have calculated a similar model with same $v_\infty = 1000\,\mathrm{km\,s^{-1}}$, but with a double-$\beta$ law (green), matching the round shape of the absorption features. Note that in the model, the emission feature of the doublet component for $J_\mathrm{up} = 3/2$ appears weaker than the other component, as the $J_\mathrm{up} = 3/2$ component is more affected by absorption lines from iron than the $J_\mathrm{up} = 1/2$ component. Without these absorption lines, the emission feature of the $J_\mathrm{up} = 3/2$ component would be a little bit stronger than the one of the $J_\mathrm{up} = 1/2$ component.

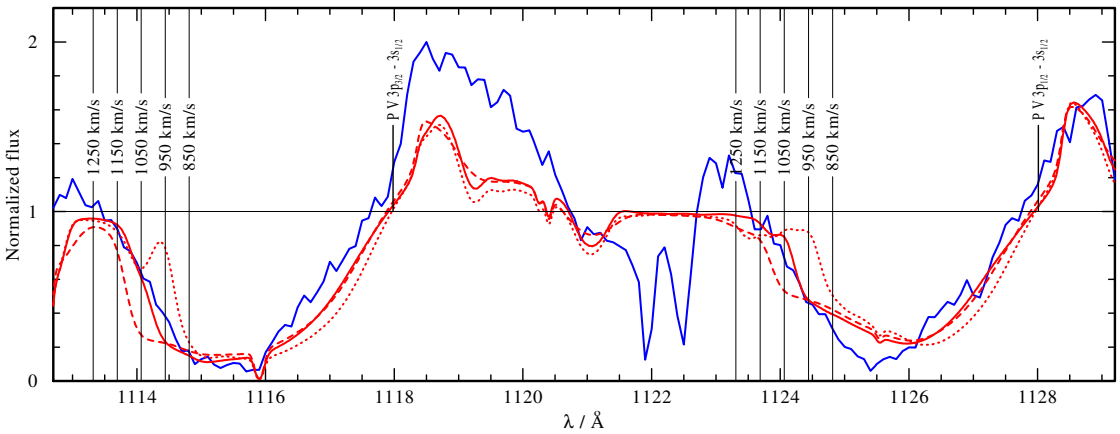

Figure 5.6: Same detail of the FUSE spectrum (blue line) as in Fig. 5.5, but plotted vs. PoWR models (including ISM absorption) using the double-β law with different terminal velocities: $v_\infty = 900\,\mathrm{km\,s^{-1}}$ (red dotted), $v_\infty = 1000\,\mathrm{km\,s^{-1}}$ (red solid), $v_\infty = 1100\,\mathrm{km\,s^{-1}}$ (red dashed). Best agreement is achieved for $v_\infty = 1000\,\mathrm{km\,s^{-1}}$, when additional line broadening with $50\,\mathrm{km\,s^{-1}}$ is taken into account.

Table 5.1: Ratios between the peak heights: measured ratios vs. ratios from the final model (model B). From our optical observation, we estimate the uncertainty in the normalized continuum to be on the order of 10 %. We consider this to be the uncertainty in the peak measurement, which we then use to infer a 20 % error in the measured ratio.

	C IV / C III	N IV / N III	He II / He I
Observed peak height ratios	1.4 ± 0.3	1.0 ± 0.2	2.3 ± 0.5
Corresponding temperature	50 ± 4 kK	54 ± 2 kK	52 ± 3 kK
Peak height ratios from the final model	1.6	0.9	2.7

As aforementioned, the strengths of the spectral lines is closely correlated to the transformed radius R_t, the stellar temperature T_*, and the chemical abundances. By definition, the transformed radius is related to the wind density, and thus, is a measure for the emissivity of the wind (the amount of emitting material). Generally, a change in the transformed radius influences all spectral lines almost similarly. The temperature determines the ionization stages: an increase in the temperature means an increase in the line strengths of higher ions of any element at the expense of the line strengths of the lower ions. Finally, the doubling of the abundance of one element should also double the strengths of its spectral lines. Naturally, the description of these correlations is highly simplified as all parameters are linked non-linearly, and they can serve as a rule of thump only. With this scheme, we start by determining R_t and T_* from a grid of models, and then measure the abundances while the other two parameters are fixed.

The grid of WNL model atmospheres[1] in the (T_*, R_t)-space is used for a first guess at the spectrum. Then a refined grid of models with adapted chemical abundances from our first guess model A (see Table 5.2) and adequate L and M is calculated. For this grid, the ratios of line strengths of N IV 7100 / N III 4634, C IV 5800 / C III 4650, and He II 4686 / He I 5876 are calculated and plotted as contour lines over the grid. Taking the ratios instead of the absolute line strengths diminishes the influence of chemical abundances, and therefore de-couples the abundance determination from finding the best-fitting (T_*, R_t). As the the C III 4650 line is blended with the N III 4634 line, its equivalent width cannot be measured accurately. Instead we use the height of peaks as a measure of the line strength, which is less affected by blending.

Although the line strengths of most of the spectral lines of carbon, oxygen, and nitrogen can be reproduced by model A, some of the unblended helium lines appear stronger than observed.

Therefore, we calculate a model with same T_*, but half of the mass-loss rate ($2^{2/3} \times R_t$) and half of the mass fraction of helium (model C in Table 5.2). To recover the line strengths of H, N, O, and C, the mass fraction for each of these elements is thus doubled.

[1] http://www.astro.physik.uni-potsdam.de/~wrh/PoWR/powrgrid1.html

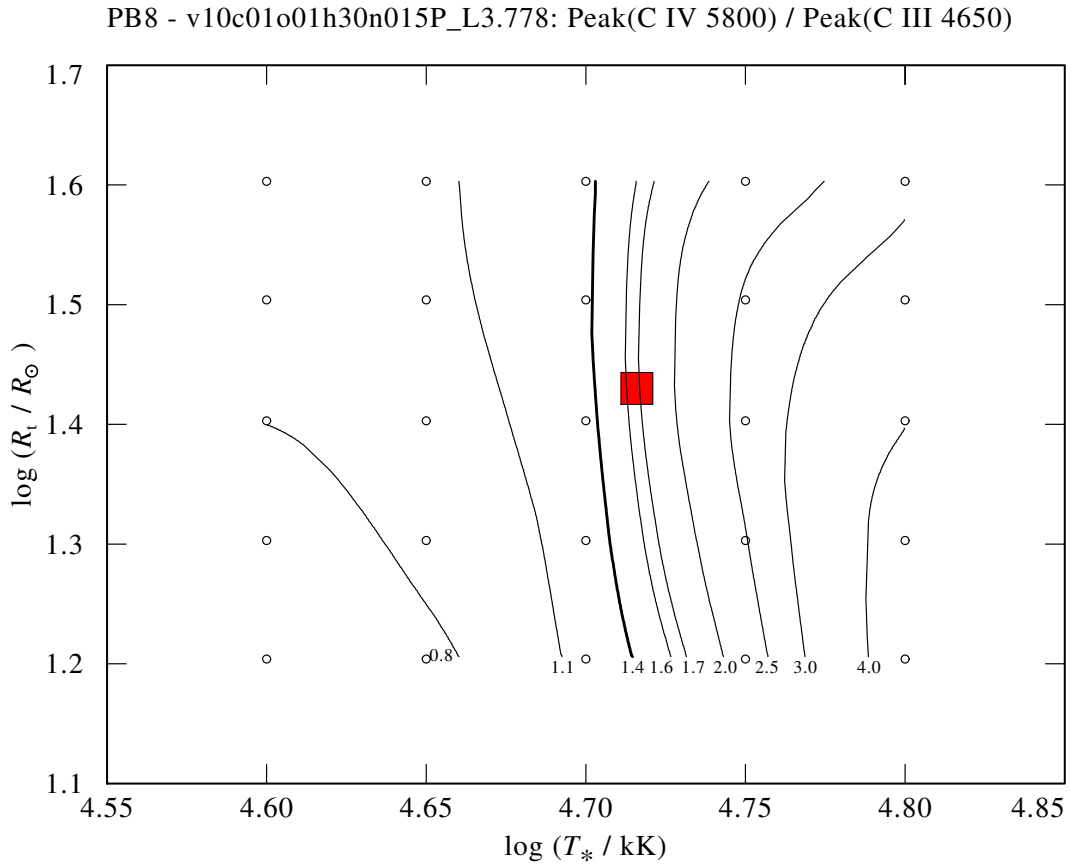

Figure 5.7: Contour plot of the ratios between the peak heights of C IV 5800 to C III 4650. The open circles correspond to the calculated models, between these data points the contour lines are interpolated. The best fitting model (model B) for PB 8 is labeled by the red square, while the thick line represents the measured value. There is no point of intersection of the contour lines of the measured ratios for all considered spectral line ratios, i.e. of the thick lines in this contour plot and the following ones. But within the inferred uncertainties our final model B is consistent with the observed line ratios.

It should be noted in fact that the mass fraction of the iron group elements must be increased as well. Although iron depletion is possible, e.g. by neutron capture in the s-process nucleosynthesis, it is hard to explain how a star probably older than the sun can have twice the solar iron abundance. Although the iron forest in the IUE spectrum can be reproduced only partially and the impact of a doubled iron abundance on line strength of the iron forest is only on the scale of 20 % at maximum, we do not alter the iron abundance of our PoWR models.

Then, as expected, all of the spectral lines of helium are weaker than in model A (Fig. 5.11). The He II 4686 in model C however seems to be more consistent with the

observation. In contrast, the line blend of He II 4859 and Hβ is deformed by deep absorption features and the He I 5876 is now overly weak.

Therefore, we choose a model with parameter values in between those of model A and C. As a compromise, the best fit of all of the spectral lines, which we could find, is achieved with our final model B, at a stellar temperature of $T_* = 52\,\mathrm{kK}$ and a transformed radius of $R_\mathrm{t} = 26.9\,\mathrm{R}_\odot$.

Parallel to the fitting of the normalized spectrum, we obtain the synthetic spectral energy distribution (SED) in absolute units. This model SED is fitted to the calibrated spectra and photometric measurements by adjusting the distance and the reddening parameter $E_{\mathrm{B-V}}$ (see Fig. 5.3).

The best fit is obtained with a color excess of $E_{\mathrm{B-V}} = 0.41$ and $R_\mathrm{V} = 4$ (Cardelli et al. 1989). This reddening is higher than the value of $E_{\mathrm{B-V}} = 0.24$ derived for the nebula from the Balmer line decrement by García-Rojas et al. (2009) for the same observations, assuming $R_\mathrm{V} = 3.1$. Following Cardelli et al. (1989), a higher value of R_V can be interpreted as a larger grain size of the dust, meaning there may be different dust composition for the planetary nebula and the central star along the line of sight. A possible explanation could be dust within the nebula in the close vicinity of the central star, as there is a strong mid-IR emission visible in MSX and IRAS observations (Fig. 5.12). The shown blackbody flux for $T = 150\,\mathrm{K}$ should demonstrate that this emission is indicative for "warm" dust. The 2MASS photometry values seem to be higher than predicted by the stellar atmosphere model due to contamination by nebular emission.

The SED fit requires a distance of 4.2 kpc. Note that this value relies on the adopted stellar luminosity of $6000\,L_\odot$, and has to be scaled when L would differ from this typical value. A distance of 5.15 kpc on PB 8 has been derived from the nebular luminosity and its brightness temperature in the radio range (5 GHz), while the nebular distances scatter between 2.2 and 5.8 kpc (Phillips 2004, and references therein).

The observed FUSE flux cannot be reproduced consistently with the IUE and optical flux by any set of parameters for the model, distance or extinction. In particular, the flux between 1120 Å and 1200 Å seems to be too low compared with the model. This might be caused by problems with the channel alignment, as reported for other observations, e.g. Miksa et al. (2002). Therefore, the FUSE spectrum shown in Fig. 5.13 has been

Table 5.2: Parameters for the PoWR models in Fig. 5.1, 5.10, and 5.11. Our final model is model B.

model	R_t	$\dot{M}$	T_*	He	H	C	N	O	d	$E_{\mathrm{B-V}}$
	$[R_\odot]$	$M_\odot\,\mathrm{a}^{-1}$	kK	% mass fraction					[kpc]	mag
A	22.4	1.3×10^{-7}	50	66	30	1	1.5	1	4.6	0.40
B	26.9	8.5×10^{-8}	52	55	40	1.3	2	1.3	4.2	0.41
C	35.5	6.3×10^{-8}	50	33	60	2	3	2	4.4	0.42

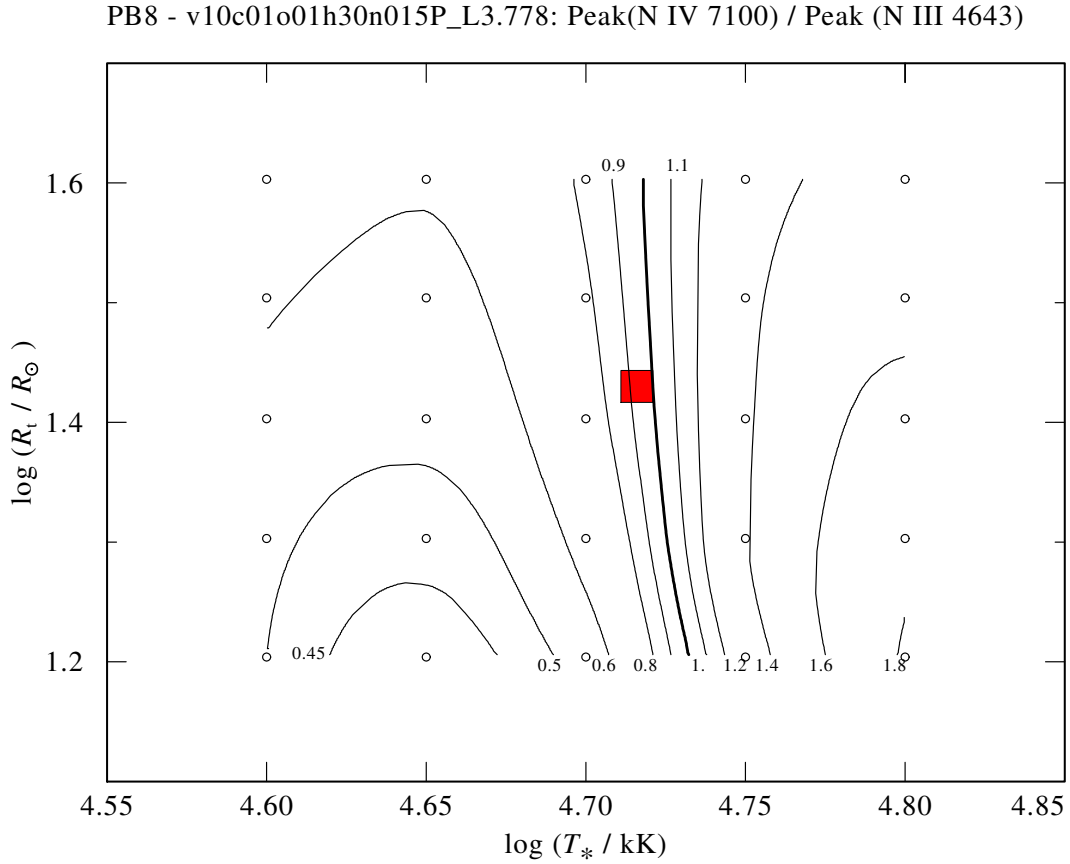

Figure 5.8: Contour plot of the ratios between the peak heights of N IV 7100 to N III 4643, using the same symbols as in Fig. 5.7. From the N IV 7100 to N III 4643 line ratio one would deduce a slightly higher temperature than our final model (model B) has.

normalized to the continuum by eye.

The FUSE spectra are as usual contaminated by H_2 absorption lines, nebular and airglow emission lines, which hampers the analysis of the underlying stellar spectrum. A simple fit of the H_2 absorption lines by eye is performed with help of adequate templates to tell interstellar from stellar absorption lines. For the fitting we use a column density of $n_{H_2}(J = 0) = 4 \times 10^{19}\,\mathrm{cm}^{-2}$ and excitation temperatures of $T_{J=0-J=1} = 60\,\mathrm{K}$ and $T_{J=2-J=4} = 270\,\mathrm{K}$. The synthetic stellar spectrum which has been corrected for this interstellar absorption from H_2 is shown in Fig. 5.13. We find the same radial velocity of $v_{\mathrm{rad}} = 12\,\mathrm{km\,s}^{-1}$ for the central star, its planetary nebula, and the absorbing ISM.

To obtain the observed P Cygni profiles of the O VI resonance doublet, superionization by X-ray emission is included in the model. Therefore, an optically thin hot gas component of $T = 1.5\,\mathrm{MK}$ is assumed to be distributed within the stellar wind. We only account for its contribution to the emissivity and opacity by free-free emission (thermal bremsstrahlung)

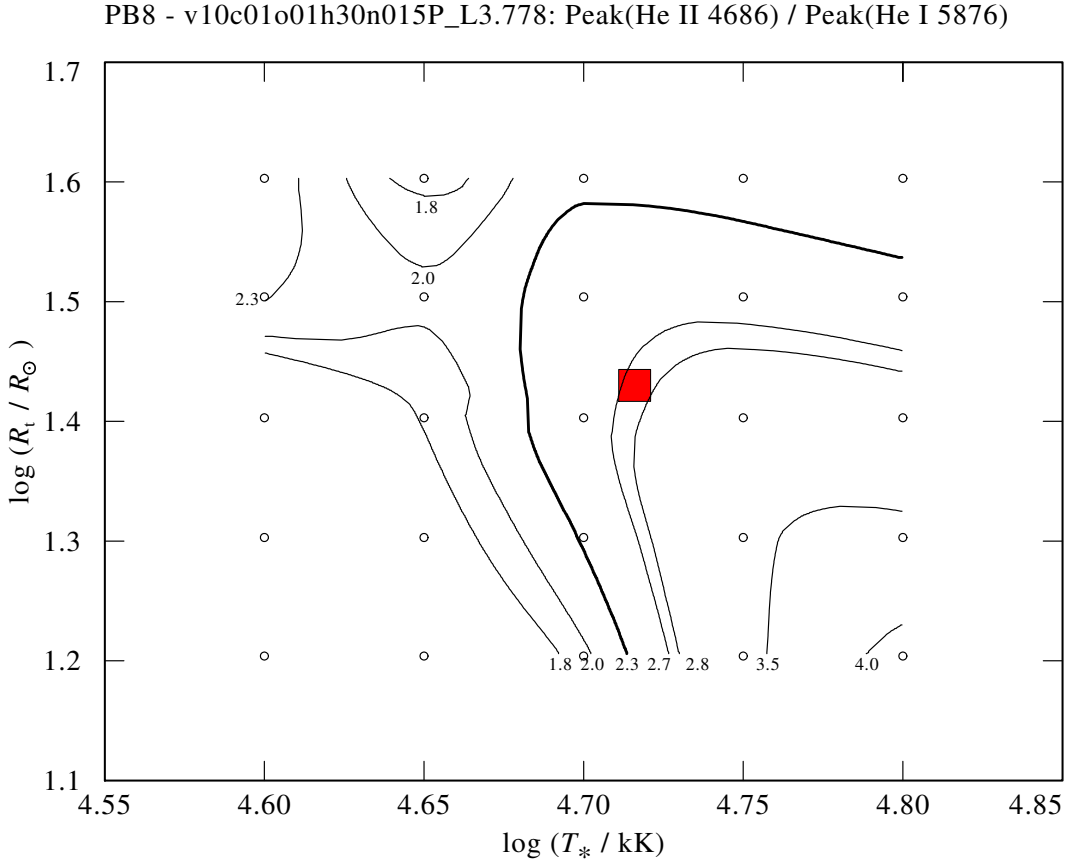

Figure 5.9: Contour plot of the ratios between the peak heights of He II 4686 to He I 5876, using the same symbols as in Fig. 5.7.

and absorption (Baum et al. 1992).

From our PoWR model (without additional X-ray emission) we predict an H I Zanstra temperature of $T(\mathrm{H\,I}) = 53 \pm 3\,\mathrm{kK}$. Shaw & Kaler (1989) measured a lower value, $T(\mathrm{H\,I}) = 32 \pm 3\,\mathrm{kK}$. This discrepancy could mean that the nebula is not optically thick in all directions of the ionizing radiation. For He II the model predicts a Zanstra temperature of only $T(\mathrm{He\,II}) = 21 \pm 1\,\mathrm{kK}$ due to strong absorption in the helium-rich wind, which means that there should not be enough photons to create a noticeable zone of fully ionized helium in the nebula. This agrees with García-Rojas et al. (2009) who could not detect any nebular He II lines in the spectrum of PB 8.

Element abundances

Hydrogen. He II lines from the Pickering series with even principle quantum numbers n appear much stronger in the observation than the odd members of the same series. As the former are blended with the Balmer lines of hydrogen, this is clear evidence for a significant

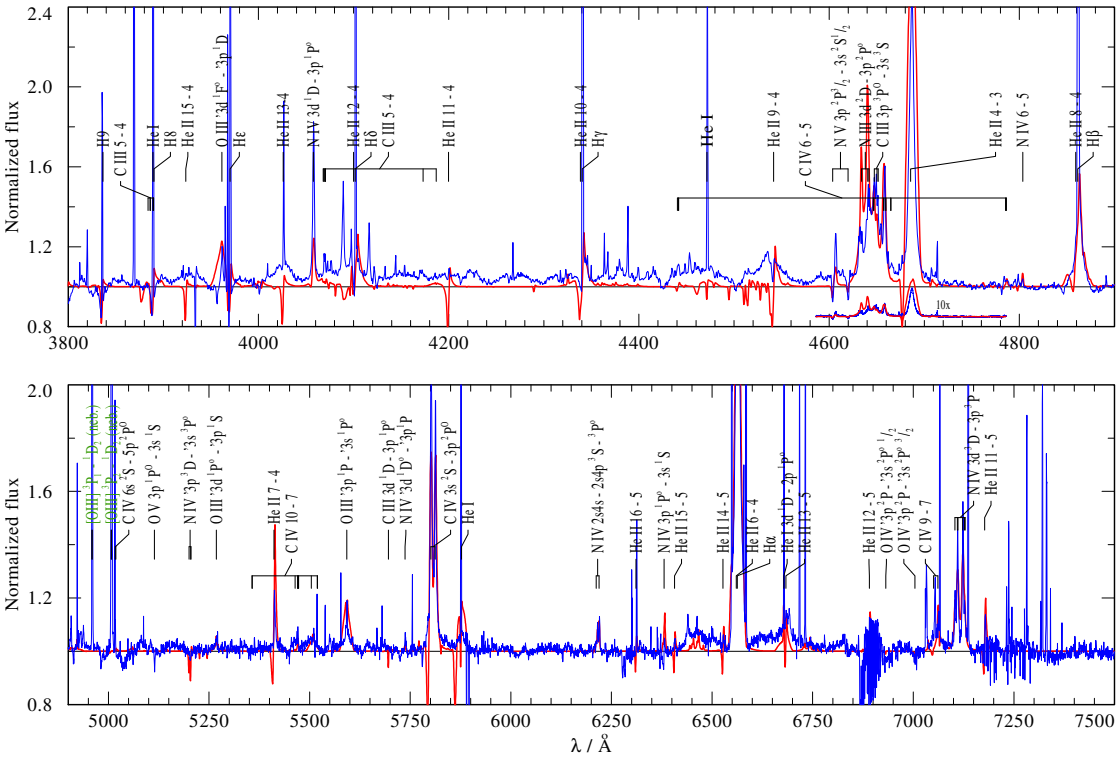

Figure 5.10: PoWR model A with only 30 % hydrogen. The emission lines from helium appear much too strong.

contribution from hydrogen. We obtain the best fit with a hydrogen mass fraction of 40 %.

Carbon. The carbon mass fraction derived from C III and C IV lines is only $X_C = 1.3\,\%$. Spectral lines from other ionization stages, especially C II, are not detected.

Oxygen. The oxygen abundance is based on the emission lines from O III and O IV. The O VI resonance line at 1031 Å in the FUSE spectrum depends on the superionization effect and is therefore not useful for the abundance determination.

Nitrogen. A nitrogen abundance of about 2 % by mass is derived from the spectral lines of N III and N IV. The N V lines appear too weak in the model. The stronger spectral lines in the observation might also be the result of superionization.

Iron. Iron-group elements, Sc, Ti, V, Cr, Mn, Fe, Co, and Ni, are included with solar metallicity ($X_{Fe} = 1.6 \times 10^{-3}$ by mass, cf. Gräfener et al. 2002). The iron forest, visible in the FUSE and IUE spectra from 1500 Å to shorter wavelengths, is roughly reproduced with these abundances.

Stellar parameters and chemical abundances derived for the central star of PB 8 are compiled in Table 5.3.

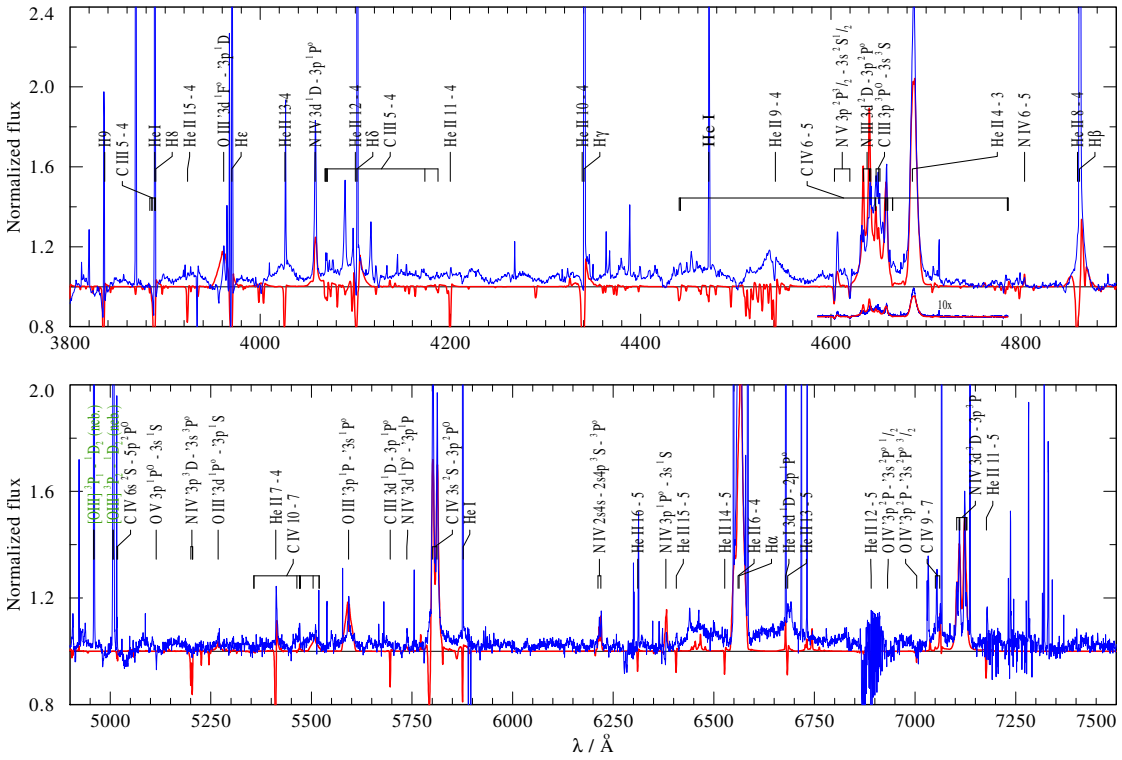

Figure 5.11: Observation vs. PoWR model C with reduced mass-loss rate relative to model A and reduced helium abundance. To recover the strength of the emission lines of carbon, nitrogen, and oxygen of model A, their abundances are increased. The helium emission lines are weaker than observed and absorption lines are stronger than in the observed spectrum. This model is considered as an upper limit for the hydrogen, carbon, oxygen, and nitrogen abundance, and as a lower limit for the mass-loss rate and the helium abundance.

Nebula age

García-Rojas et al. (2009) derived from the separation of the maxima of [O III] $\lambda\,5007$ an expansion velocity of $14 \pm 2\,\mathrm{km\,s^{-1}}$. With the same method we find from [N II] $\lambda\,6548$ and 6583 an expansion velocity of $19 \pm 6\,\mathrm{km\,s^{-1}}$. Following Schönberner et al. (2005a), this kind of discrepancy is characteristic for young planetary nebulæ, as the individual emission lines form in different regions with different velocities in the beginning of the PN expansion. Especially for the determination of the kinematic age of the nebula, only the [N II] shell is a reliable indicator (Schönberner et al. 2005a). Therefore we estimate the shell radius from the [N II] spectrogram, obtaining a value of 2.5″. No substructure of the [N II] doublet, which would indicate different velocities for rim and shell, can be resolved. Thus we adopt the peak separation as the indicator for the shell expansion velocity,

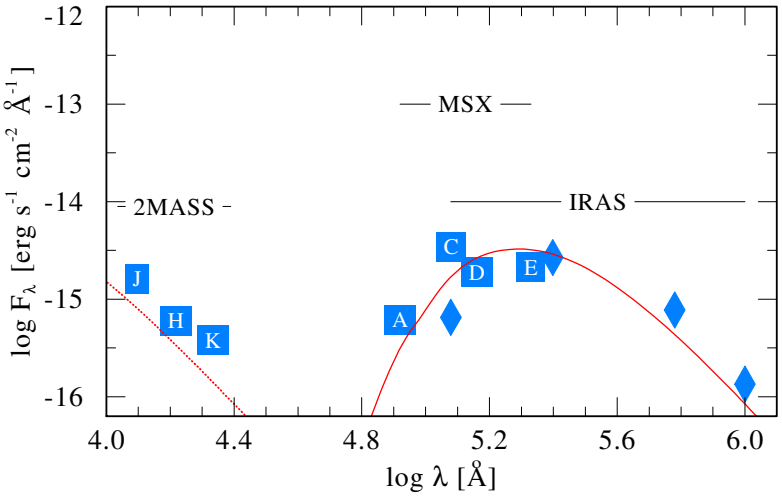

Figure 5.12: SED for PB 8 in the infrared range. Photometric observations (blue blocks) for JHK are from 2MASS, ACDE from MSX (MSXPSC V2.3), and 12, 25, 60, 100 μm (blue diamonds) from IRAS (IPAC V2.0 1986). Also shown is the synthetic stellar continuum (red dotted) and a blackbody spectrum (red line) for $T = 150$ K, indicating warm dust emission.

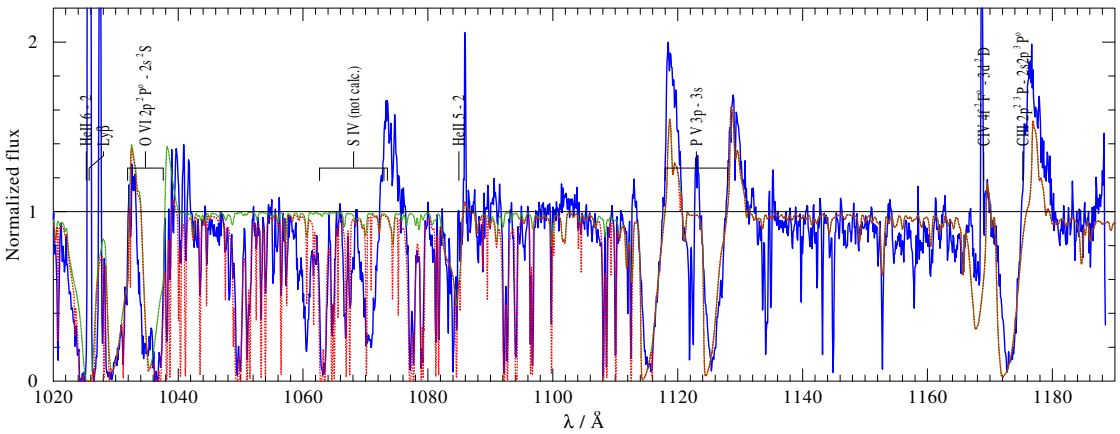

Figure 5.13: Detail of the normalized FUSE spectrum (blue line) compared to the synthetic spectrum after accounting for interstellar H_2 and Lyman absorption (red dotted). The stellar spectrum shows strong P Cygni profiles. Superimposed are narrow interstellar absorption lines of H_2, emission lines from the planetary nebula, and telluric air glow features. The synthetic spectrum without interstellar H_2 absorptions is shown for comparison (green).

Table 5.3: Parameters from PoWR model and comparison with observation for the central star of PB 8.

T_*	52 ± 2	kK
v_∞	1000 ± 100	$\mathrm{km\,s^{-1}}$
$\dot{M}$	$(8.5^{+4.0}_{-2.2}) \times 10^{-8}$	$M_\odot\, a^{-1}$
R_t	$26.9^{+8.6}_{-4.5}$	$R_\odot$
$E_\mathrm{B-V}$	0.41 ± 0.01	mag
$d(L_* = 6000\,\mathrm{L}_\odot)$	4.2 ± 0.2	kpc
v_rad	12	$\mathrm{km\,s^{-1}}$
H	40^{+20}_{-10}	% mass fraction
He	55^{+11}_{-22}	% mass fraction
C	$1.3^{+0.7}_{-0.3}$	% mass fraction
N	$2.0^{+1.0}_{-0.5}$	% mass fraction
O	$1.3^{+0.7}_{-0.3}$	% mass fraction

and regard this as a lower limit. Together, with the shell radius and the spectroscopic distance, this yields an upper limit for the dynamical age of the nebula of 2900 years, in agreement with Gesicki et al. (2006). Hence we conclude that PB 8 is a relatively young nebula.

5.1.4 Discussion

PN and Central star status

PB 8 appears as a roughly spherical nebula, nearly round in the composite image of Hα, [N II], and [O III] (Fig. 5.14, also available at `http://www.astro.washington.edu/balick/PNIC/`), although the shell shows some knotty structure. In particular, there is a bright structure extending from the center to the northern side of the shell. The long-slit spectrogram reveals also good symmetry in the radial velocities (Fig. 5.15).

Given the unique chemical abundances of the central star PB 8, one must reconsider the possibility that this object is in fact a massive star with a ring nebula. However, the low nebular expansion velocity discussed in Sect. 5.1.3 is rather characteristic for PNe. Medina et al. (2006) found expansion velocities for PNe with Wolf-Rayet nuclei in the range of $8 - 44\,\mathrm{km\,s^{-1}}$ from direct observations. Expansion velocities for ring nebulæ around massive stars are systematically higher, $16 - 110\,\mathrm{km\,s^{-1}}$ (Chu et al. 1999).

Moreover, the electron density in PB 8 measured by García-Rojas et al. (2009), $n_\mathrm{e} = 2550 \pm 550\,\mathrm{cm^{-3}}$ is typical for young planetary nebulæ, but several times higher than found in ring nebulæ (Mathis et al. 1992).

Furthermore, if the central star of PB 8 were a massive star, this would imply a

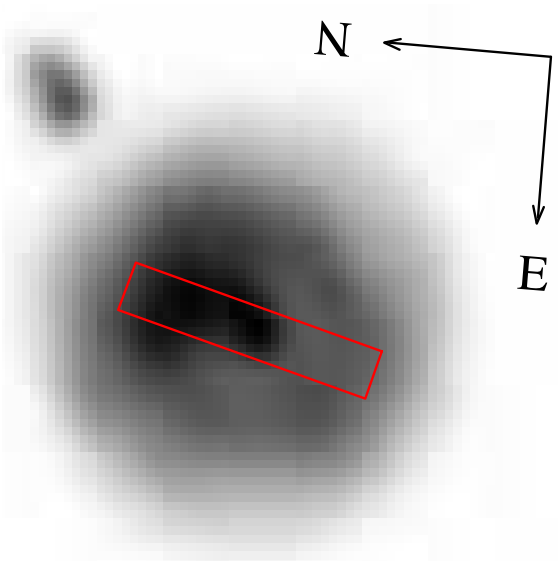

Figure 5.14: Composite picture of PB 8 from Hα, [N II], and [O III] emission lines with linear intensities (adapted from Schwarz et al. 1992). Also shown is the slit position (red rectangle) of our optical observation. The slit orientation was set to the parallactic angle, which actually varied between $-20°$ and $-10°$ during the exposure. The bright nebular knot in the northern part of the slit can also be recognized in the lower part of the spectrogram (Fig. 5.15).

luminosity of at least $\log(L/L_\odot) = 5.3$, which shifts the distance to ≈ 24.2 kpc. With a Galactic latitude of 4° this corresponds to a height of 1.7 kpc above the fundamental plane of the Galaxy. This is much more than the scale height of the thin disk and therefore, an unlikely location for a massive star.

Re-classification of the central star of PB 8

The central star of PB 8 has been classified as spectral type [WC5-6] by Acker & Neiner (2003). However, we have shown above that the central star of PB 8 is not a member of the [WC] sequence; its spectrum shows strong lines of nitrogen, reflecting that its chemical composition rather resembles that of a WN star. Nevertheless, carbon is slightly enhanced, in contrast to the typical WN composition where carbon is strongly depleted due to the CNO cycle equilibrium.

Among the massive WN stars there are a few objects with a similar composition as our program star, usually considered as caught in the transition phase to enter the WC stage, and classified as spectral type WN/WC or WNC. Therefore, in analogy to these massive stars, we suggest to classify the central star of PB 8 as [WN/WC].

The detailed subtype of PB 8 is WN6 when applying the classification scheme established

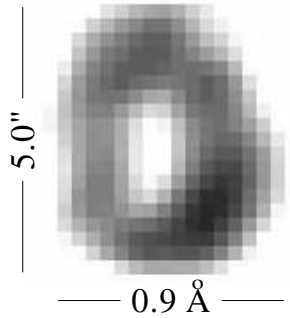

Figure 5.15: Spectrogram of the [O III] 5007Å line, indicating the roughly spherical symmetry of the nebula. This symmetry is seen along the slit, as well as in the dispersion direction which reflects the radial velocity along the line-of-sight. The southern end of the slit is to the top (cf. Fig. 5.14).

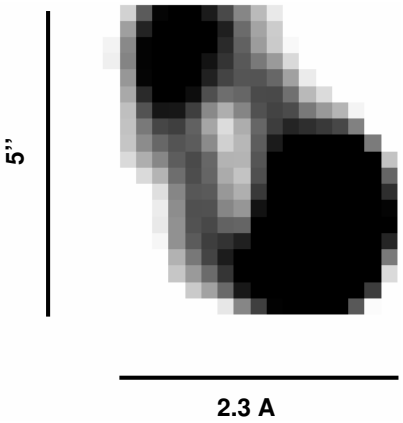

Figure 5.16: Spectrogram of the [N II] 6583Å line, similar to Fig. 5.15, but more extended emission in dispersion direction, indicating a higher velocity of the [N II] emitting region than for the [O III] emitting region.

by Smith (1968) for massive WN stars. With the scheme in van der Hucht et al. (1981) for massive WC stars, the WC7 subtype seems to be appropriate. In combination with these two schemes, we determine the detailed subtype classification is [WN6/WC7].

The subtype [WC5-6] classification of PB 8 by Acker & Neiner (2003) was partly based on the identification of spectral features with stellar C II, but we cannot confirm any stellar C II line from our high-resolution data.

Tylenda et al. (1993) defined alternatively the class of "weak emission line stars" (WELS) for those spectra that show much fainter and narrower emission lines than massive WC stars. Gesicki et al. (2006) assign this WELS classification to PB 8. However, the nature and homogeneity of the WELS class seems to be still unclear.

There are two other known WR-type central stars with non carbon-rich winds. One is LMC-N 66 in the LMC, which is only occasionally of the Wolf-Rayet type. It has an irregular nebula and seems to be a close binary (see discussion in Peña et al. 2004). The other example, the central star of PMR 5 discovered by Morgan et al. (2003), is probably a Galactic [WN] star. Its spectrum shows only helium and nitrogen lines, while any carbon lines are missing. In case of PB 8, carbon and oxygen lines are also visible. Morgan et al. (2003) discussed the PN status of PMR 5 on the basis of nebular expansion velocity and electron density and concluded that PMR 5 is a normal PN.

Evolutionary status

The surface composition of PB 8 appears unique among all central stars of planetary nebulæ that have been analyzed thus far. Only two other CSPNe (PMR 5 and the enigmatic variable LMC-N 66) are known to show a WN-type composition dominated by helium with a significant amount of nitrogen. Two more CSPNe are known to be helium-rich, but without strong winds (LoTr 4 and K 1-27 , Rauch et al. 1998). Our program star PB 8, however, is unique in showing a significant amount of carbon, while carbon is usually depleted in WN-type compositions. This poses the question of how to explain the evolutionary origin of PB 8.

The formation of hydrogen-deficient post-AGB stars is explained by a thermal pulse which leads to the ingestion of the hydrogen envelope (Herwig et al. 1999; Herwig 2001; Werner & Herwig 2006; Althaus et al. 2005). The last thermal pulse may occur either at the tip of the AGB (AGB final thermal pulse, AFTP) or later, when the AGB has been left (late thermal pulse, LTP, or very late thermal pulse, VLTP). These models lead to a carbon-rich surface composition (carbon abundance larger than 20 % by mass), right to explain the [WC]-type central stars. The nitrogen abundance is predicted to be very small, except for the VLTP case where $X_{\rm N} \geq 1\%$ has been predicted (Althaus et al. 2005; Werner & Herwig 2006).

As a tentative explanation for PB 8, we propose that the last thermal pulse has been only "weak", such that only a small amount of carbon has been dredged up to the surface. The bulk of matter now at the surface is helium-rich from the former intershell region, that also contained some nitrogen according to the equilibrium from the CNO cycle. In addition, some of the hydrogen-rich envelope must have survived the last pulse and became mixed into the present outer layers. While it is not clear whether such a "weak" last thermal pulse can happen on the AGB, it might occur in an extremely late VLTP when the star is already too cool to undergo a full He-shell flash (F. Herwig, priv. comm.).

Further constraints for the evolutionary origin of PB 8 may be derived from the planetary nebula. In Sect. 5.1.3 we have shown that the present nebula is younger than 3000 years. There is no visible remnant of an older PN. Moreover, the nebula abundance ratios He / H = 0.123 and N / O = 0.28 by number (García-Rojas et al. 2009) show that PB 8 is not a helium enriched Peimbert's Type I PN. For the latter ones He / H > 0.125 or N / O > 0.5 is expected (Peimbert & Torres-Peimbert 1987). A VLTP origin of the nebula is therefore implausible. The low N / O ratio also indicates the absence of hot bottom burning (HBB), which is predicted for the more massive AGB stars. From comparison with stellar evolutionary tracks, Kaler & Jacoby (1989) deduce N / O > 0.8 as a sharp limit for N-enriched PNe, indicating HBB in AGB-stars with $M_{\rm core} > 0.8\,{\rm M}_\odot$.

Thus, the following alternative scenarios might explain our results:

1. The CSPN of PB 8 has a low mass and evolves slowly. For instance, a $0.6\,{\rm M}_\odot$ post-AGB star on the way to an LTP has a crossing time from 10^4 K to its maximum effective temperature in 4000 years (Blöcker 2003). Then, either

   a) the present nebula has been ejected by a born-again AGB-star after occurrence

of a "weak" VLTP. A possible older PN from the first AGB phase has already dissolved. As mentioned above, this scenario does not fit well to PB 8, as the PN is not enriched in helium; or,

b) the CSPN suffered an "anomalous AFTP", resulting in the observed surface abundances. The nebula was formed only during this AGB phase of the star. In this scenario it is difficult to explain the enhanced nitrogen abundance of the star, as nitrogen enrichment is neither predicted for the AFTP nor can it originate from HBB.

2. Alternatively, the CS of PB 8 may have a relatively high mass and therefore evolved very fast. The crossing time for, as an example, a $0.94\,M_\odot$ post-AGB star is only 50 years (Blöcker 2003). A VLTP has already occurred, but most of the nebula presently observed still originates from the first AGB period, not from the born-again AGB star after the VLTP. Albeit possible, this scenario has a low probability because the empirical mass distribution of central stars has a sharp maximum at $0.6\,M_\odot$ and declines substantially towards higher values (Tylenda 2003); furthermore there are no hints of HBB, which would be indicative for a more massive CSPN.

However, one has to keep in mind that the appropriate stellar evolution models are still calculated only in 1D. Especially the convective mixing during H-ingestion flashes of the TPs were treated in diffusion approximation, whereas recent hydrodynamical studies, e.g. by Woodward et al. (2008), emphasize that convective mixing is rather an advection process, making 2D or 3D calculations necessary.

Alternatively to single star evolution, one may consider binarity with a common envelope phase as origin of hydrogen deficiency. However, PB 8 shows no evidence for binarity. The nebula does not look bipolar. Also, Méndez (1989) found no indication of radial velocity variations between three spectra taken within one year, but only changes of the P-Cygni line profiles which must be attributed to variability of the stellar wind.

Summarizing, the evolutionary origin of PB 8 cannot be explained by any existing model for a post-AGB star which lost its hydrogen envelope by a last thermal pulse. However, one can imagine scenarios of a weak or anomalous thermal pulse occurring either on the AGB or later, which may explain the unique chemical composition of this star and its young nebula.

The chemical composition found in the expanding atmosphere of the central star of PB 8 differs from any known central star abundance. However, it resembles the rare transition class of WN/WC subtypes of massive Wolf-Rayet stars. Therefore we suggest to open a new class of [WN/WC]-type central stars with PB 8 being its first member.

5.2 PMR 5 - A [WN] central star candidate

Hydrogen-deficient central stars that are not of type [WC] seem to be very rare. So far, only two examples are known in our Galaxy: one is the central star of PN PB 8, for which a spectral analysis is presented in Section 5.1, and the other one is PMR 5, discovered by Morgan et al. (2003). In the spectrum of PMR 5 (see Fig. 5.18), Morgan et al. (2003) identified broad stellar lines of helium and nitrogen, but no spectral line arising from carbon. Therefore they suggest PMR 5 to be a [WN]-type central star.

5.2.1 Observations

The photometric data for PMR 5 (cf. Fig. 5.17) indicates a relatively high reddening. Therefore, PMR 5 is relatively faint in the optical range. Morgan et al. (2003) give an estimate for E_{B-V} of 3.0 to 3.5.

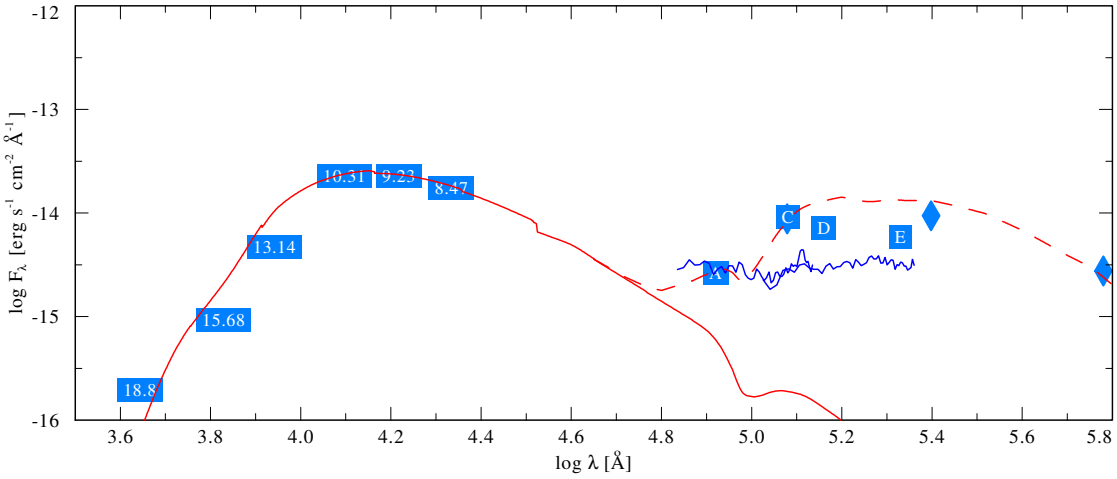

Figure 5.17: Spectral energy distribution of PMR 5, PoWR model (red line) vs. observation: photometric values (blue blocks) from USNO-A2.0 (Monet 1998) for B, I and R from USNO-B1.0 (Monet et al. 2003), JHK from 2MASS (Skrutskie et al. 2006), ACDE from MSX (MSXPSC V2.3), and blue diamonds from IRAS (IPAC V2.0 1986). Also shown is a low resolution IRAS spectrum (blue line) and a tentative blackbody fit (red dashed line) of temperature $T = 150$ K to the photometric values. The infrared excess above 80 000 Å may be attributed to circumstellar warm dust, as found in many PNe.

Although Morgan et al. (2003) used a spectrograph which covers the range of 3800 – 7300 Å at the SAAO 1.9-m telescope, there was no signal below $\lambda = 5500$ Å as PMR 5 is too red for this instrumental setup. Thus, only a small part of the optical spectrum is available (cf. Fig. 5.18). The spectrum has a very low S/N ratio and has only a

low resolution of 7.4 Å per pixel, corresponding to a resolution of 280 to 400 km s^{-1} in velocity.

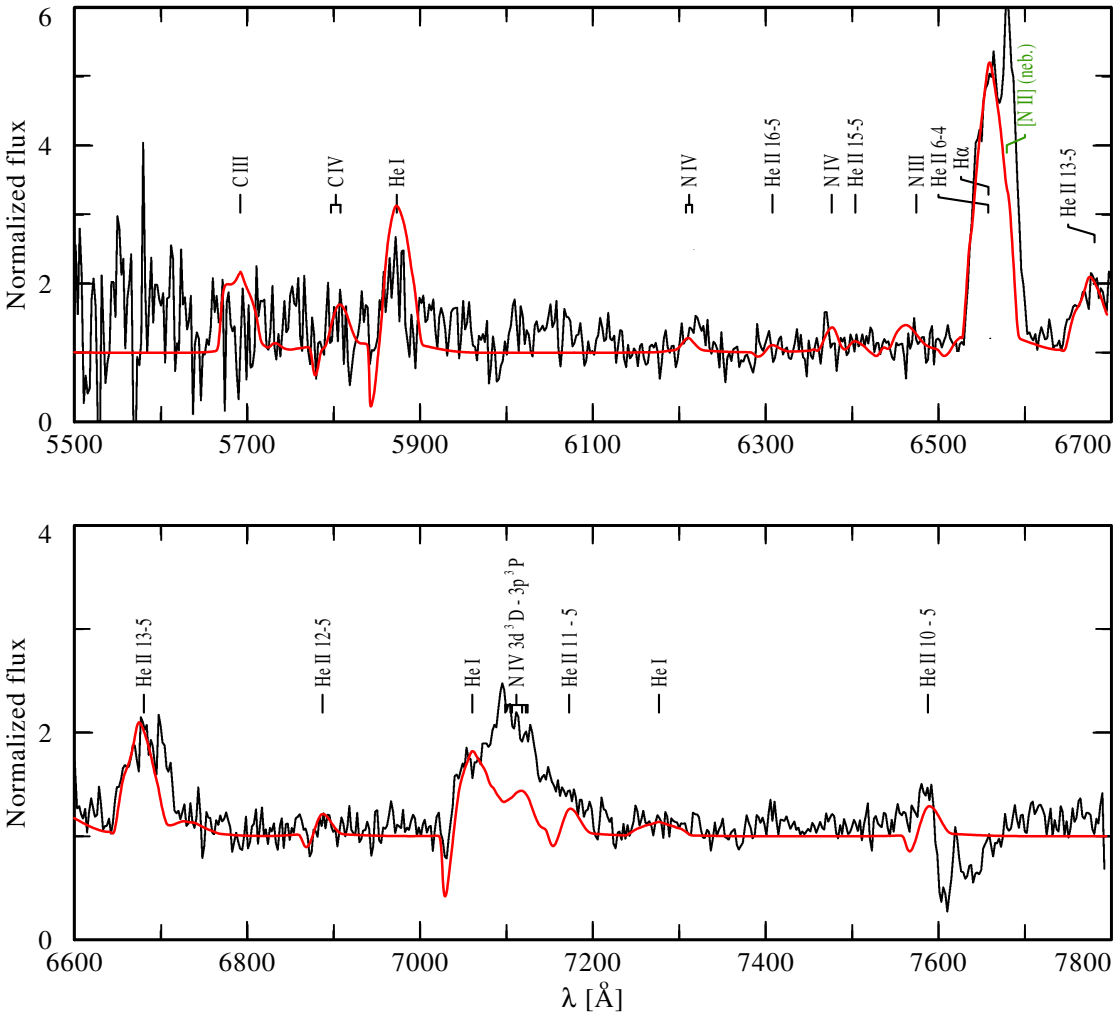

Figure 5.18: Optical spectrum of PMR 5: observation (black line) adopted from Morgan et al. (2003) vs. a PoWR-model with 10 % nitrogen. To match the observation, the model spectrum and the identifiers for the spectral lines are shifted to shorter wavelengths by $v_{\rm rad} = 200\,{\rm km\,s^{-1}}$.

5.2.2 Analysis

We adopt the optical spectrum from Morgan et al. (2003) and try to find a PoWR model fitting the observation. In Fig. 5.18, the spectrum from Morgan et al. (2003) is shown together with a PoWR-model for a WNL-like chemical composition. Having only a short

spectrum of low quality, the primary intention of the fit is to confirm the identifications of the spectral lines and to check for the presence of any carbon lines.

To match the observation, we have to shift our model and the identifiers for the spectral lines to shorter wavelengths by $v_{\rm rad} = 200\,{\rm km\,s^{-1}}$. This value is smaller than the spectral resolution, therefore it does not necessarily mean that PMR 5 has a $v_{\rm rad}$ of $-200\,{\rm km\,s^{-1}}$.

The model accounts for H, He, N, C, and iron group elements. We assume solar abundances for the iron group elements. The grid of WNL model atmospheres[2] in the $(T_*, R_{\rm t})$-space is used for a first guess at the spectrum. From the ratio of line strengths between the He I and He II lines, we derive a temperature of $T = 56\,{\rm K}$ and a transformed radius of $R_{\rm t} = 3.6\,R_\odot$. From the width of the spectral lines, we infer a terminal velocity of $v_\infty = 1500\,{\rm km\,s^{-1}}$. The density contrast of $D = 4$ is adopted from the WNL grid, as the quality of the spectrum is not sufficient to derive the density contrast from the strength of the electron scattering line wings.

Then, models with appropriate stellar luminosity and stellar mass, i.e. $L = 6000\,L_\odot$ and $M = 0.6\,M_\odot$, are calculated (cf. Table 5.4).

Because of the anomalous strength of the N IV 3d ^{3}D-3p ^{3}P line multiplet, we increase the nitrogen abundance in our PoWR model to 10 % by mass. Moreover, a mass fraction of 20% is necessary to reproduce the observed strength of the N IV 3d ^{3}D-3p ^{3}P line multiplet. As one can already see in Fig. 5.18, already at a nitrogen abundance of than 10 %, the modeled N III 6479 Å line is stronger than observed.

Regarding the low S/N ratio of the observation, the helium lines are sufficiently well fitted with an abundance of ca. 70 % by mass.

A hydrogen abundance of 20 % is directly adopted from the grid of WNL model atmospheres. The only hydrogen line is Hα, which is blended with the He II 6-4 line. Although the model fits well to the observed line blend, the fraction of nebular Hα in the observed line blend is unknown. Hence, it is possible that the hydrogen abundance is overestimated.

In the range of the optical spectrum from Morgan et al. (2003), the strongest carbon lines are the C III 5696 Å emission line and the C IV 5801/5812 Å multiplet. Both carbon lines belong to the noisiest part of the spectrum, hampering a reliable identification. Therefore, we cannot determine precise carbon abundances. However, from the absence of a clear signal, we infer an upper limit of 1 % by mass for the carbon abundance.

We also looked for oxygen lines, but within the given wavelength range no oxygen line can be found in the observation. From the comparison to the spectral analysis of PB 8 (cf. Sect. 5.1) and the oxygen lines found there, we find that oxygen with a mass fraction of less than 1 % would escape detection in the case of the noisy spectrum of PMR 5.

The derived parameters are summarized in Table 5.4.

[2] http://www.astro.physik.uni-potsdam.de/~wrh/PoWR/powrgrid1.html

Table 5.4: PMR 5: Parameters from the PoWR model fit of the observation for the central star PMR 5.

T_*	56	kK
L	6000	$L_\odot$
v_∞	1500 ± 400	$\mathrm{km\,s^{-1}}$
$\dot{M}$	3.3×10^{-6}	$M_\odot\, a^{-1}$
R_t	3.6	$R_\odot$
D	4	(density contrast)
H	20	% mass fraction
He	69	% mass fraction
N	10	% mass fraction
O	-	% mass fraction
C	< 1	% mass fraction
$E_\mathrm{B-V}$	3	mag
$d(L_* = 6000\, L_\odot)$	0.5	kpc
t_dyn	200	years

5.2.3 Discussion

Classification

Morgan et al. (2003) claim that PMR 5 is a Wolf-Rayet type central star, although the high expansion velocity of its nebula of $165\,\mathrm{km\,s^{-1}}$ is rather unusual for a PN (cf. Sect. 5.1.4). The arguments given for the central star status of PMR 5 are not necessarily mandatory. E.g., although the infrared excess, which is attributed to emission from warm dust, is often found in PNe, there exist examples of massive WN stars that show an IR excess due to emission from warm dust (e.g. Barniske et al. 2008). Ring nebula around massive stars may also appear circular, and recently new WN stars were found by the Hα emission of their nebula (e.g. Gvaramadze et al. 2009). Hence, it cannot be ruled out that PMR 5 is a massive WR star.

However, PMR 5 is obviously an emission-line star, showing spectral lines from helium and nitrogen. Morgan et al. (2003) have already mentioned the absence of carbon lines and thus supposed that PMR 5 is not a WC-type star, but rather a WN-like star. From our spectral analysis, we agree with this classification and try to determine the spectral subtype.

Unfortunately, the optical spectrum from Morgan et al. (2003) does not cover the wavelength range that contains the spectral lines for the classification of the WN subtype by Smith (1968).

Therefore, Morgan et al. (2003) compared their optical spectrum of PMR 5 with WR spectra by Vreux et al. (1983) and classified PMR 5 as WN6, or [WN6] respectively.

We choose another method by relying on our PoWR model fit and use the synthetic

spectrum from the PoWR model. Applying the classification scheme of Smith (1968) to the synthetic spectrum (see Fig. 5.19) we would classify PMR 5 as of subtype WN8, or, including brackets to distinguish PMR 5 from massive WN stars, as [WN8]. Alternatively, with the derived stellar temperature of $T_* = 56\,\mathrm{K}$ and the transformed radius of $\log R_\mathrm{t}/R_\odot = 0.6$, the same subtype, WN8, can be determined from Fig. 5 in Hamann & Gräfener (2004).

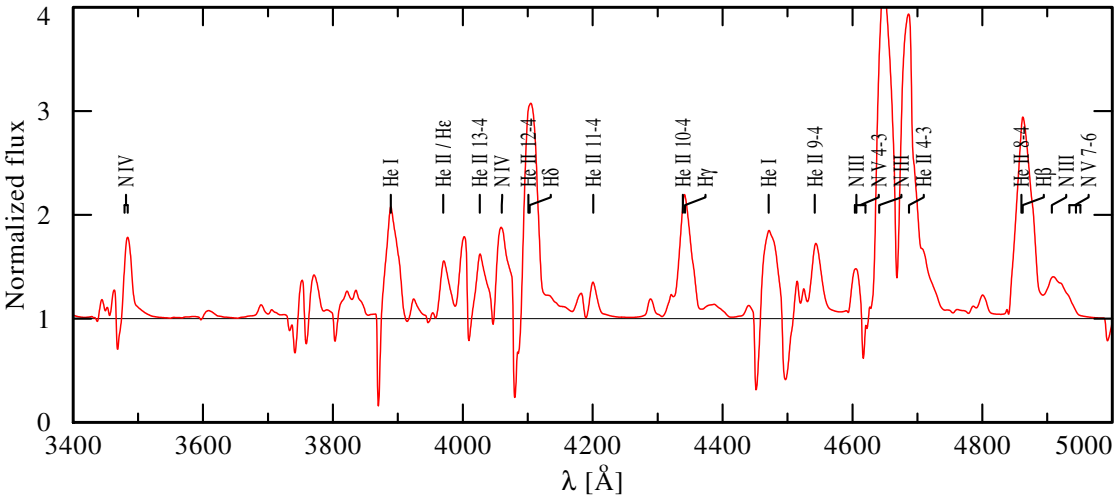

Figure 5.19: Optical spectrum of the PoWR model for PMR 5, showing the spectral lines used for classification.

Abundances and evolutionary status

Having only a small piece of the optical spectrum in low quality and with only a few spectral lines, the derived parameters must be considered to be relatively uncertain. In particular, the high nitrogen abundance of 10 % relies mainly on one line multiplet. Moreover, it is difficult to explain the anomalous overabundance of nitrogen and, at the same time, a mass fraction of less than 1 % of carbon. Therefore, we must prospect for unusual scenarios that can reproduce these abundances.

Binarity is maybe the first thing that comes to the mind. So far, no hints of binarity of PMR 5 have been found. The nebula looks perfectly circular. The optical spectrum shows no indication of a companion star, and the observed IR excess can be attributed to dust emission. Moreover, there is no time series of sufficiently highly resolved spectra that could reveal a periodic line shift due to a orbital motion. Although a binary evolution of PMR 5 cannot be ruled out for the moment, in the following, we consider only a single-star evolution of PMR 5.

Hence, for low-mass stars, during the occurrence of thermal pulses, the formation of a ^{14}N pocket is predicted, e.g. by Althaus et al. (2005). The ^{14}N pocket is formed at

the base of the helium buffer after the dredge-up phase and contains 46 % ^{14}N by mass. During the following thermal pulse, this nitrogen is burnt to ^{22}Ne. It can be speculated, whether it is possible that the ^{14}N pocket is not burnt during the following pulse, but instead mixed upwards , thus resulting in the observed surface composition of PMR 5.

Furthermore, in the VLTP scenario, nitrogen can be produced from carbon via $^{12}\mathrm{C}(\mathrm{p},\gamma)^{13}\mathrm{N}$, resulting in a nitrogen abundance of a few percent (Werner & Herwig 2006). Arguments against the VLTP scenario in case of PMR 5 are the predicted abundances of $X_\mathrm{C} \approx 40$, $X_\mathrm{O} \approx 20$, and $X_\mathrm{H} = 0$ by mass. While the hydrogen abundance may be in fact zero for PMR 5, carbon and oxygen abundances of 40 % and 20 % respectively can be excluded.

Nevertheless, if the nitrogen abundance of PMR 5 were only 1.5 %, the other abundances would be consistent with those of massive WNL stars. Then, the observed nebula around PMR 5 would be a ring nebula and its expansion velocity would not be consistent with values found for other ring nebula (Chu et al. 1999).

Bibliography

Abbott, D. C., Beiging, J. H., Churchwell, E., & Torres, A. V. 1986, ApJ, 303, 239

Acker, A., Marcout, J., Ochsenbein, F., Stenholm, B., & Tylenda, R. 1992, Strasbourg - ESO catalogue of galactic planetary nebulae. Part 1; Part 2 (Garching: European Southern Observatory, 1992)

Acker, A. & Neiner, C. 2003, A&A, 403, 659

Althaus, L. G., Serenelli, A. M., Panei, J. A., et al. 2005, A&A, 435, 631

Ambarzumjan, V. & Mustel, E. 1957, Theoretische Astrophysik

Barlow, M. J. & Hummer, D. G. 1982, in IAU Symposium, Vol. 99, Wolf-Rayet Stars: Observations, Physics, Evolution, ed. C. W. H. de Loore & A. J. Willis, 387–392

Barniske, A., Oskinova, L. M., & Hamann, W.-R. 2008, A&A, 486, 971

Baum, E., Hamann, W.-R., Koesterke, L., & Wessolowski, U. 1992, A&A, 266, 402

Blöcker, T. 2003, in IAU Symposium, Vol. 209, Planetary Nebulae: Their Evolution and Role in the Universe, ed. S. Kwok, M. Dopita, & R. Sutherland, 101

Bloecker, T. 1995, A&A, 299, 755

Bond, H. E., Kawaler, S. D., Ciardullo, R., et al. 1996, AJ, 112, 2699

Cardelli, J. A., Clayton, G. C., & Mathis, J. S. 1989, ApJ, 345, 245

Chu, Y.-H., Weis, K., & Garnett, D. R. 1999, AJ, 117, 1433

Crowther, P. A., Abbott, J. B., Hillier, D. J., & De Marco, O. 2003, in IAU Symposium, Vol. 209, Planetary Nebulae: Their Evolution and Role in the Universe, ed. S. Kwok, M. Dopita, & R. Sutherland, 243

De Marco, O. 2002, Ap&SS, 279, 157

De Marco, O., Barlow, M. J., & Storey, P. J. 1997, MNRAS, 292, 86

De Marco, O. & Crowther, P. A. 1998, MNRAS, 296, 419

De Marco, O. & Crowther, P. A. 1999, MNRAS, 306, 931

De Marco, O., Crowther, P. A., Barlow, M. J., Clayton, G. C., & de Koter, A. 2001, MNRAS, 328, 527

De Marco, O., Storey, P. J., & Barlow, M. J. 1998, MNRAS, 297, 999

Feibelman, W. A. 1999, PASP, 111, 221

García-Rojas, J., Peña, M., & Peimbert, A. 2009, A&A, 000, xxx

Gesicki, K., Zijlstra, A. A., Acker, A., et al. 2006, A&A, 451, 925

Gräfener, G. & Hamann, W.-R. 2005, A&A, 432, 633

Gräfener, G., Hamann, W.-R., & Todt, H. 2008, in Astronomical Society of the Pacific Conference Series, Vol. 391, Hydrogen-Deficient Stars, ed. A. Werner & T. Rauch, 99

Gräfener, G., Koesterke, L., & Hamann, W.-R. 2002, A&A, 387, 244

Groenewegen, M. A. T. & Lamers, H. J. G. L. M. 1989, A&AS, 79, 359

Grosdidier, Y., Acker, A., & Moffat, A. F. J. 2002, in Revista Mexicana de Astronomia y Astrofisica Conference Series, Vol. 12, Revista Mexicana de Astronomia y Astrofisica Conference Series, ed. W. J. Henney, J. Franco, & M. Martos, 90–91

Gvaramadze, V. V., Fabrika, S., Hamann, W.-R., et al. 2009, MNRAS, in press

Hamann, W.-R. & Graefener, G. 2005, in Astronomical Society of the Pacific Conference Series, Vol. 334, 14th European Workshop on White Dwarfs, ed. D. Koester & S. Moehler, 341

Hamann, W.-R. & Gräfener, G. 2004, A&A, 427, 697

Hamann, W.-R., Gräfener, G., & Koesterke, L. 2003, in IAU Symposium, Vol. 212, A Massive Star Odyssey: From Main Sequence to Supernova, ed. K. van der Hucht, A. Herrero, & C. Esteban, 198

Hamann, W.-R., Gräfener, G., & Liermann, A. 2006, A&A, 457, 1015

Hamann, W.-R. & Koesterke, L. 1998a, A&A, 335, 1003

Hamann, W.-R. & Koesterke, L. 1998b, A&A, 335, 1003

Hazard, C., Terlevich, R., Ferland, G., Morton, D. C., & Sargent, W. L. W. 1980, Nature, 285, 463

Herald, J. E. & Bianchi, L. 2004, ApJ, 609, 378

Herwig, F. 2001, Ap&SS, 275, 15

Herwig, F. 2005, ARA&A, 43, 435

Herwig, F., Blöcker, T., Langer, N., & Driebe, T. 1999, A&A, 349, L5

Herwig, F., Bloecker, T., Schoenberner, D., & El Eid, M. 1997, A&A, 324, L81

Herwig, F., Schoenberner, D., & Bloecker, T. 1998, A&A, 340, L43

Hillier, D. J. 1987, ApJS, 63, 965

Hillier, D. J. 1990, A&A, 231, 116

Hillier, D. J. 1991, A&A, 247, 455

Hillier, D. J. & Miller, D. L. 1999, ApJ, 519, 354

Iben, Jr., I., Kaler, J. B., Truran, J. W., & Renzini, A. 1983, ApJ, 264, 605

Iben, Jr., I. & Tutukov, A. V. 1985, ApJS, 58, 661

Jacoby, G. H. & Ford, H. C. 1983, ApJ, 266, 298

Kaler, J. B. & Jacoby, G. H. 1989, ApJ, 345, 871

Keeler, J. E. 1898, ApJ, 8, 113

Kippenhahn, R. & Weigert, A. 1990, Stellar Structure and Evolution, ed. R. Kippenhahn & A. Weigert

Koesterke, L. 2001, Ap&SS, 275, 41

Koesterke, L. & Hamann, W.-R. 1997a, in IAU Symposium, Vol. 180, Planetary Nebulae, ed. H. J. Habing & H. J. G. L. M. Lamers, 114

Koesterke, L. & Hamann, W.-R. 1997b, A&A, 320, 91

Koesterke, L. & Hamann, W.-R. 2002, in Astronomical Society of the Pacific Conference Series, Vol. 260, Interacting Winds from Massive Stars, ed. A. F. J. Moffat & N. St-Louis, 259

Kudritzki, R. P., Urbaneja, M. A., & Puls, J. 2006, in IAU Symposium, Vol. 234, Planetary Nebulae in our Galaxy and Beyond, ed. M. J. Barlow & R. H. Méndez, 119–126

Leuenhagen, U. 1997a, in IAU Symposium, Vol. 180, Planetary Nebulae, ed. H. J. Habing & H. J. G. L. M. Lamers, 119

Leuenhagen, U. 1997b, in IAU Symposium, Vol. 180, Planetary Nebulae, ed. H. J. Habing & H. J. G. L. M. Lamers, 118

Leuenhagen, U. & Hamann, W.-R. 1994, A&A, 283, 567

Leuenhagen, U. & Hamann, W.-R. 1998, A&A, 330, 265

Leuenhagen, U., Hamann, W.-R., & Jeffery, C. S. 1996, A&A, 312, 167

Li, J., Harrington, J. P., & Borkowski, K. J. 2002, AJ, 123, 2676

Marcolino, W. L. F., Hillier, D. J., de Araujo, F. X., & Pereira, C. B. 2007, ApJ, 654, 1068

Mathis, J. S., Cassinelli, J. P., van der Hucht, K. A., et al. 1992, ApJ, 384, 197

McCandliss, S. R. 2003, PASP, 115, 651

McGraw, J. T., Liebert, J., Starrfield, S. G., & Green, R. 1979a, in IAU Colloq. 53: White Dwarfs and Variable Degenerate Stars, ed. H. M. van Horn & V. Weidemann, 377–381

McGraw, J. T., Starrfield, S. G., Angel, J. R. P., & Carleton, N. P. 1979b, SAO Special Report, 385, 125

Medina, S., Peña, M., Morisset, C., & Stasińska, G. 2006, Revista Mexicana de Astronomia y Astrofisica, 42, 53

Méndez, R. H. 1989, in IAU Symposium, Vol. 131, Planetary Nebulae, ed. S. Torres-Peimbert, 261

Méndez, R. H. 1991, in IAU Symposium, Vol. 145, Evolution of Stars: the Photospheric Abundance Connection, ed. G. Michaud & A. V. Tutukov, 375

Miksa, S., Deetjen, J. L., Dreizler, S., et al. 2002, A&A, 389, 953

Miller Bertolami, M. M. & Althaus, L. G. 2007, MNRAS, 380, 763

Monet, D. 1998, USNO-A2.0, ed. D. Monet

Monet, D. G., Levine, S. E., Canzian, B., et al. 2003, AJ, 125, 984

Morgan, D. H., Parker, Q. A., & Cohen, M. 2003, MNRAS, 346, 719

Oskinova, L. M., Hamann, W.-R., & Feldmeier, A. 2007, A&A, 476, 1331

Paczyński, B. 1970, Acta Astronomica, 20, 47

Pakull, M. W. 2009, in IAU Symposium, Vol. 256, IAU Symposium, ed. J. T. van Loon & J. M. Oliveira, 437–442

Peña, M., Hamann, W.-R., Ruiz, M. T., Peimbert, A., & Peimbert, M. 2004, A&A, 419, 583

Peimbert, M. & Torres-Peimbert, S. 1987, Revista Mexicana de Astronomia y Astrofisica, vol. 14, 14, 540

Phillips, J. P. 2004, MNRAS, 353, 589

Pottasch, S. R., ed. 1984, Astrophysics and Space Science Library, Vol. 107, Planetary nebulae - A study of late stages of stellar evolution

Ralchenko, Yu., K. A. R. J. & NIST ASD Team. 2008

Rauch, T., Dreizler, S., & Wolff, B. 1998, A&A, 338, 651

Sahai, R., Wootten, A., & Clegg, R. E. S. 1993, in IAU Symposium, Vol. 155, Planetary Nebulae, ed. R. Weinberger & A. Acker, 229

Sanduleak, N. 1971, ApJ, 164, L71

Schmutz, W., Hamann, W.-R., & Wessolowski, U. 1989, A&A, 210, 236

Schönberner, D., Jacob, R., & Steffen, M. 2005a, A&A, 441, 573

Schönberner, D., Jacob, R., Steffen, M., et al. 2005b, A&A, 431, 963

Schwarz, H. E., Corradi, R. L. M., & Melnick, J. 1992, A&AS, 96, 23

Schwarzschild, M. & Härm, R. 1965, ApJ, 142, 855

Shaw, R. A. & Kaler, J. B. 1989, ApJS, 69, 495

Sion, E. M., Liebert, J., & Starrfield, S. G. 1985, ApJ, 292, 471

Skrutskie, M. F., Cutri, R. M., Stiening, R., et al. 2006, AJ, 131, 1163

Smith, L. F. 1968, MNRAS, 138, 109

Smith, L. F. & Aller, L. H. 1969, ApJ, 157, 1245

Space Telescope Science Institute & Osservatorio Astronomico di Torino. 2001, VizieR Online Data Catalog, 1271

Stasińska, G., Gräfener, G., Peña, M., et al. 2004, A&A, 413, 329

Tajitsu, A. & Tamura, S. 1998, AJ, 115, 1989

Tylenda, R. 2003, in IAU Symposium, Vol. 209, Planetary Nebulae: Their Evolution and Role in the Universe, ed. S. Kwok, M. Dopita, & R. Sutherland, 159

Tylenda, R., Acker, A., & Stenholm, B. 1993, A&AS, 102, 595

van der Hucht, K. A. 2001, New Astronomy Review, 45, 135

van der Hucht, K. A., Conti, P. S., Lundstrom, I., & Stenholm, B. 1981, Space Science Reviews, 28, 227

van der Hucht, K. A., Jurriens, T. A., Wesselius, P. R., et al. 1985, A&A, 145, L13

Vreux, J. M., Dennefeld, M., & Andrillat, Y. 1983, A&AS, 54, 437

Werner, K. 2001, Ap&SS, 275, 27

Werner, K., Heber, U., & Hunger, K. 1991, A&A, 244, 437

Werner, K. & Herwig, F. 2006, PASP, 118, 183

Werner, K. & Rauch, T. 1994, A&A, 284, L5

Werner, K., Rauch, T., & Kruk, J. W. 2007, A&A, 474, 591

Werner, K., Rauch, T., Reiff, E., Kruk, J. W., & Napiwotzki, R. 2004, A&A, 427, 685

Woodward, P., Herwig, F., Porter, D., et al. 2008, in American Institute of Physics Conference Series, Vol. 990, First Stars III, ed. B. W. O'Shea & A. Heger, 300

Wright, A. E. & Barlow, M. J. 1975, MNRAS, 170, 41

Zacharias, N., Monet, D. G., Levine, S. E., et al. 2004, in Bulletin of the American Astronomical Society, Vol. 36, Bulletin of the American Astronomical Society, 1418

Zanstra, H. 1927, ApJ, 65, 50

Danksagung

Abschließend möchte ich mich bei den Menschen bedanken, die diese Arbeit unterstützt haben.

Als erstes danke ich natürlich meinem Hauptsponsor, meiner Familie.

Dann möchte ich mich beim gesamten Bereich Astrophysik der Uni Potsdam bedanken, besonders für die tolle Arbeitsatmosphäre, in der es Spaß gemacht hat, die Doktorarbeit zu schreiben.

Spezieller Dank gilt meinem Doktorvater Wolf-Rainer Hamann für die Ermöglichung und intensive Betreung dieser Doktorarbeit.

Meinem Doktoronkel Götz Gräfener danke ich für Normalität und die Turboversion des PoWR-Codes (inklusive der vorlauten COMA-Testversion), bei der man die Gammas so schön anziehen kann, und mit deren Hilfe manche Modellrechnungen, insbesondere für Neon, erst möglich wurden.

Ein großer Dank an Andrea Brockhaus, ohne die wir alle kopflos wären.

Miriam Peña danke ich für durchwachte Nächte, um meine Beobachtungsdaten zu gewinnen, und für die ausführlichen fachlichen Diskussionen.

Weiterhin danke ich Martin Roth und Christer Sandin vom AIP für die Kollaboration im D3Dnet.

Ganz besonders bedanke ich mich bei meinen Kolleginnen Adriane Liermann und Ute Rühling für anregende Zwischenfragen und das Zusammenhalten im Doktorarbeits-Schlussspurt. Ebenso herzlichen Dank an Nadine Giese und Fabian Krause, auch für die gute Zusammenarbeit an unserem ersten PNN-Artikel.

Schließlich danke ich meiner Arbeitsgruppe, vor allem Cora Fechner, Thorsten Tepper García, Andreas Barniske, Lida Oskinova, Philipp Richter und Achim Feldmeier für erholsame Kekspausen und interessante Fragen. Und ein Dank auch an unseren Systemadministrator Peer Leben, der unsere Rechner am Laufen hält.